Doctoral Dissertation
Doctoral Program in Materials Science and Technology (31th Cycle)

Innovative Materials for Post Lithium-ion Batteries

Mojtaba Alidoost
******

Supervisors
Prof. Silvia. Bodoardo
Prof. Nerino. Penazzi, Co-Supervisor

Doctoral Examination Committee:
Prof. EzequielLeiva, Universidad Nacional de Córdoba
Prof.Giovanni Battista Appetecchi, ENEA

Politecnico di Torino
April 25, 2019

This thesis is licensed under a Creative Commons License, Attribution - Noncommercial - NoDerivative Works 4.0 International: see www.creativecommons.org. The text may be reproduced for non-commercial purposes, provided that credit is given to the original author.

I hereby declare that, the contents and organisation of this dissertation constitute my own original work and does not compromise in any way the rights of third parties, including those relating to the security of personal data.

…….....

Mojtaba Alidoost

Turin, April 25, 2019

Summary

The universal strategies towards low CO_2 emitting fuels, makes the use of clean renewable energy resources necessary. The intermittent nature of the renewable energies and energy consumption profile require efficient energy storage systems. In addition, the electrification of transport as one of the main solution to reach local zero emission, principally is based on the battery technologies.

Rechargeable lithium batteries, have already conquered the market of electronic devices such as cell phones, portable computers and middle size home appliance. The use of lithium-ion technology for hybrid or electric vehicles (EV), demands higher energy density. Lithium-sulfur batteries with theoretical energy density 2600 Wh/kg are subject of many current studies for EV applications. Sulfur is an abundant, sustainable, eco-friendly and low cost cathode material which can be a solution in the near future for energy storage. However, the commercialization of lithium-sulfur batteries is limited by insulating nature of elemental sulfur and shuttling of dissolved lithium sulfides across the separator and reach the anode. Several solutions are suggested by scientific communities to mitigate lithium-sulfur issues. These strategies are focused on various cell components such as anode, cathode and the electrolyte. In this dissertation three main components of lithium-sulfur cell (Anode-Cathode-Electrolyte) and two polymeric separators for lithium-air battery are studied.

A brief introduction about the importance of electrochemical energy storage, electric cars and market trend is discussed in chapter 1. Chapter 2 is dedicated to general description of materials for lithium-sulfur batteries. The synthesis of sustainable and low cost cyclodextrin-based nanosponges (CD-NS) is reported in chapter 3. NSs were applied in three fields: i) CITR-NS were used to prepare an oxygen selective membrane for lithium-air battery. The dispersion of NS in PVdF polymer, provided a membrane with significant reduction in water permeability while oxygen selectivity was increased by more than six times. Replacing the polymeric matrix with PEEK, resulted in oxygen-blocking membrane which was used as a lithium anode protection. ii) The carbonization of PMDA-NS provides a micro porous carbon which was used as conductive matrix for sulfur cathode synthesis. Moreover, a hierarchical carbon (HC-CNS) was prepared by silica template method to give a better accessibility of electrolyte to infiltrated sulfur. iii) Silicon nanoparticles were embedded in nanosponge during

synthesis and subsequently the carbonization was performed to give conductivity to this nanosponge matrix (Si@CNS). In chapter 4, the use of Si@CNS together with other silicon nanoparticles as an alternative anode is reported. The progressive improvements from simple Si-rGO to wrap Si3@CNS in graphene sheets (Si3@CNS-rGO) which has shown a high specific capacity and coulombic efficiency are discussed. At the end of chapter 4, an electrolyte with LiTFSI salt and fluoroethylene carbonate (FEC) additive is introduced which has increased the specific capacity more than 40%. In chapter 5, the preparation of high sulfur loading cathode (S@HC-CNS) with melt-infusion method is described. Because of good reproducibility in specific capacity, S@HC-CNS was used as standard cathode for electrolyte characterizations. In chapter 6, the water-based synthesis and application of pyrrolidinium-based ionic liquid as an additive for the electrolyte of lithium-sulfur battery is elucidated. Also the effect of electrolyte composition, separator type and electrolyte quantity are studied. In the chapter 7, a full cell with Si@CNS-rGO anode and S@HC-CNS cathode is introduced.

Acknowledgment

My first sincere thank is addressed to my tireless supervisor Prof. Silvia Bodoardo, who with her dedication to the work, motivates me to discover new opportunities. I would like to thank Prof. Nerino Penazzi, who during my PhD, with his patience, answers my countless doubts and guides me to understand electrochemistry. He was always available to discuss every detail of my work and helps me to interpret the results.

My third thank goes to my group members, Prof. Carlotta Francia, Dr. Julia Amici, Daniele Versaci and Usman Zubair which without their support, the experimental part of my thesis was not completed.

I would like to express my deepest appreciation and thanks to Prof. Francesco Trotta, Dr. Anastasia Anceschi and Dr. Fabrizio Caldera who dedicate their precious time and support in material synthesis and characterization in the Università di Torino.

And last but not least, I would like to thank my wife Farzaneh for her continues support during all this years because of many times she renounced social life when I was in the lab.

I would like to dedicate this thesis to my loving parents and Farzaneh

Contents

1. Chapter 1 Energy Storage 1
   1.1 Introduction 1
   1.2 Renewable Energy Sources (RES) 2
   1.3 Energy Storage Systems 3
   1.4 Electrochemical Power Source 4
   1.5 E-CAR 5
2. Chapter 2 Materials for lithium-sulfur batteries 8
   2.1 Sulfur Chemistry 8
      2.1.1 Sulfur reduction intermediate products 9
      2.1.2 Polysulfide Thermodynamics 9
   2.2 Materials for Anode 11
      2.2.1 Lithium metal anode 11
      2.2.2 Carbon-based anode 12
      2.2.3 Anode alloying materials 13
      2.2.4 Silicon as high capacity anode material 14
   2.3 Sulfur Cathode 16
      2.3.1 Carbon-based cathode 16
      2.3.2 Titanium-based cathode 17
   2.4 Liquide Electrolyte for Lithium-Sulfur Batteries 17
      2.4.1 Conduction phenomena in liquid electrolytes 18
      2.4.2 Liquid electrolytes categories for lithium-sulfur batteries 19
      2.4.3 Solvent mixture 20
      2.4.4 Salt dissolution & Dielectric Constant 21
      2.4.5 Ionic liquids based electrolytes 21
3. Chapter 3 Cyclodextrin Based Nanosponges Material as Battery Components 24
   3.1 Cyclodextrin as Building Block 24
   3.2 Cyclodextrin-Based Nanosponges (CD-NSs) 25
   3.3 Synthesis of Cyclodextrin-based Nanosponges 26
      3.3.1 Carbonyldiimidazole Nanosponge (CDI-NS) 26
      3.3.2 Hexamethylene diisocyanate Nanosponge (HMDI-NS) 28
      3.3.3 Pyromellitic Dianhydride Nanosponge (PMDA-NS) 29
      3.3.4 Citric acid Nanosponge (CITR-NS) 31
   3.4 Membrane for Lithium-Air batteries 33
      3.4.1 Oxygen selective membrane 33

3.4.2 Lithium protective membrane 34
3.5 Porous Carbon for Sulfur Cathode 35
3.5.1 Conventional Carbonization of NS synthesis to prepare CNS 35
3.5.2 Silica template NS synthesis to prepare HC-CNS 39
3.6 Silicon Anode- Embedded in CNS 43
3.6.1 Pure Silicon and Silicon with passivate layer 44
3.6.2 Silicon percentage in Nanosponge 46
4. Chapter 4 Innovative Anode Active Material Based on Si Nanoparticles 48
4.1 Experimental Set-up 48
4.1.1 Electrode preparation 49
4.1.2 Cell assembling 49
4.1.3 Electrochemical Tests 50
4.2 Graphene preparation 51
4.3 Silicon wrapped in Graphene 53
4.3.1 Bare Silicon-SiNPs 53
4.3.2 Silicon-rGO Composite 55
4.3.3 Silicon Nanoparticles in 3D-rGO (Si-rGO-PAM) 57
4.3.4 Si3-rGO-PAM-Passivate silicon nanoparticles 61
4.4 Embedded silicon nanoparticles in CD-NS 64
4.4.1 Carbonization of Si@ NS 64
4.4.2 Optimization of Silicon mass loading 67
4.4.3 Graphene wrapped Silicon anode-Si3@CNS-rGO 72
4.5 Electrode Fabrication 78
4.5.1 Binder effect 78
4.5.2 Mixing Method 79
4.6 Electrolyte with LiTFSI Salt and FEC Additive 81
5. Chapter 5 Sulfur Cathode Preparation 84
5.1 Sulfur Cathode Preparation Methods 84
5.2 Sulfur Cathode Active Material Based on HC-CNS 85
6. Chapter 6 Electrolyte for Lithium–Sulfur Cell 91
6.1 Experimental Methods 91
6.1.1 Electrolyte Conductivity – Conductivity of Cell 91
6.1.2 Electrolyte/Separator Conductivity – EL Cell 91
6.1.3Polysulfide Measurement 92
6.2 Ether-Based Solvent Mixture Electrolytes 93
6.2.1 Lithium Salts 93
6.2.2 The Effect of Salt Concentration on the Ionic Conductivity 94

6.2.3 Performance of Li-S Cell with Ether-based Electrolyte 95

6.3 Ionic Liquids-Based Electrolyte for Lithium-Sulfur Batteries 101

6.3.1 Ionic Liquid Synthesis 101
6.3.2 Empirical Characterizations of Ionic Liquid 104
6.3.3 Ionic Liquid; Effect of Celgard2500 and Whatman 105
6.3.4 Ionic Liquids as Additive for Electrolyte 109
6.3.5 Standard Electrolyte and Ionic Liquid Additive; Effect of Celgard2500 and Whatman 111
6.3.6 Standard Electrolyte and Ionic Liquid Additive; Effect of Celgard2500 and Whatman 116

7. Chapter 7 Silicon-Sulfur Full Cell 120
8. Chapter 8 Conclusion and Prospects 123

Figures

Figure 1-1: Energy consumption trend by sources in 50 years 2
Figure 1-2:Battery technology comparison.....5
Figure 1-3: Share of transport greenhouse gas emissions.....6
Figure 2-1:Lithium dendrite.....11
Figure 2-2: Effect of polysulfide on lithium metal 12
Figure 2-3: Lithium intercalation in graphite.....12
Figure 2-4: Voltage-Time profile of nano-sized silicon nanoparticles 15
Figure 3-1: Cyclodextrin categories comparison 25
Figure 3-2: Nanosponge-based material application in battery field 26
Figure 3-3: 1,1′- Carbonyldiimidazole nanosponge synthesis 27
Figure 3-4: a) TGA , b) FTIR analysis of CDI-NS 27
Figure 3-5: Hexamethylene diisocyanate nanosponge synthesis 28
Figure 3-6: a) TGA, b) FTIR analysis of HMDI-NS 29
Figure 3-7: Pyromellitic Dianhydride nanosponge synthesis 30
Figure 3-8: a) TGA, b) FTIR analysis of PDMA-NS 30
Figure 3-9: Citric acid nanosponges synthesis.....31
Figure 3-10: a)TGA, b) FTIR analysis of CITR-NS.....32
Figure 3-11: Dried nanosponges powder 32
Figure 3-12: Hydrophobic cavity of cyclodextrin.....33
Figure 3-13: Nitrogen adsorption isotherm of different carbonized nanosponges 37
Figure 3-14: Hollow carbonized nanospongesspheres.....38
Figure 3-15: XPS spectra of HC-CNS 40
Figure 3-16: FESEM images of HC-CNS.....42
Figure 3-17: Nitrogen adsorption isotherm of hierarchical carbonized nanosponges.....43
Figure 3-18: Embedding of silicon nanoparticles in nanosponge 44
Figure 3-19: Gel formation of a) Si@CNS and b) Si3@CNS 45
Figure 3-20: a) Sonication of reagents under Nitrogen flux, b) Gel formation of nanosponges under nitrogen flux with magnet stirring 46
Figure 4-1: a)Film applicator, b) Adjustable blade 49
Figure 4-2: a) EL-CELL, b) coin cell.....50
Figure 4-3: a) Mixing, b) Dialysis.....51
Figure 4-4: FESEM image of reduced graphene oxide-rGO 53
Figure 4-5: a)Galvanostatic cycling, b) Charge and discharge capacity of Bare silicon.....54
Figure 4-6:FESEM images of agglomerated silicon nanoparticles between graphene sheets 56
Figure 4-7: a) Galvanostatic cycling, b) Charge and discharge capacity of Si-rGO 57
Figure 4-8: TGA analysis of silicon nanoparticles in Si-3D-rGO 58
Figure 4-9: FESEM images of silicon nanoparticles in 3D-graphene (Si-3D-rGO).....59

Figure 4-10: EDX analysis of silicon nanoparticles in 3D-graphene (Si-3D-rGO) 60
Figure 4-11: a)Galvanostatic cycling and Coulombic efficiencies, b) Charge and discharge capacity of silicon nanoparticles in 3D-graphene (Si-3D-rGO) 61
Figure 4-12: TGA analysis of passivated silicon nanoparticles in 3D-graphene (Si3-3D-rGO) 62
Figure 4-13:FESEM images of passivated silicon nanoparticles in 3D-graphene Si3-3D-rGO 62
Figure 4-14: a)Galvanostatic cycling and Coulombic efficiencies,b)Charge and discharge capacity of passivated silicon nanoparticles in 3D-graphene (Si3-3D-rGO) 63
Figure 4-15: FESEM images of passivated silicon nanoparticles embedded in carbonized nanosponges (Si3@CNS) 65
Figure 4-16: FESEM images of Si3@CNS a) before, b) after ball milling ... 66
Figure 4-17: TGA analysis of silicon nanoparticles embedded in nanosponge with initial silicon a) 10%, b) 20% 68
Figure 4-18: Nitrogen adsorption isotherm of the Si3@CNS at 77K and PMDA-CNS 69
Figure 4-19: a) Galvanostatic cycling and Coulombic efficiencies, b) Charge and discharge capacity of (Si@CNS) 70
Figure 4-20:a) Galvanostatic cycling and Coulombic efficiencies,b) Charge and discharge capacity of Si3@CNS 71
Figure 4-21: Comparison between galvanostatic cycling of Si@CNS and Si3@CNS 72
Figure 4-22: Low density Si3@CNS-rGO after Freeze-drying 73
Figure 4-23: FESEM images of Si3@CNS-rGO 74
Figure 4-24: TEM images of Si3@CNS-rGO a) distribution of oxygen on the surface of SiNPs, b) presence of homogeneous carbon shell on the SiNPs,c) presence of inhomogeneous carbon shell on the SiNPs,d) the distribution of Si3@CNS on the rGO 75
Figure 4-25:XRD analysis of passivate silicon nanoparticles before treatment (Si3) and after final synthesis (Si3@CNS-rGO) 76
Figure 4-26:a) Galvanostatic cycling and Coulombic efficiencies,b) Charge and discharge capacity of Si3@CNS-rGO 77
Figure 4-27: FESEM images of micrometric channel inside the electrode structure. 78
Figure 4-28: Flexible anode prepared with innovative method 79
Figure 4-29: FESEM images of Si3@CNS-rGO a) before, b) after galvanostatic cycling 80
Figure 4-30: a) Agglomerated SiNPs after lithiation/delithiation, b) expanding inside carbonous matrix 81
Figure 4-31: Comparison between galvanostatic cycling of Si3@CNS and Si3@CNS-rGO in the modified (EC:DMC(v:v) + 1M LiTFSI + 1%FEC) 82
Figure 5-1: Preparation of cathode by sulfur infiltration in HC-CNS 85
Figure 5-2: TGA curve of S@HC-CNS 86

Figure 5-3: FESEM images of a) HC-CNS carbon,b) S@HC-CNS cathode .87
Figure 5-4: a) FESEM images of S@HC-CNS,b) Mapping distribution of sulfur on the surface and inside the pores of HC-CNS 88
Figure 5-5: Raman spectra of S@HC-CNS 89
Figure 6-1: Arrhenius plots of the ionic conductivity of the electrolyte with three (1M,2M,4M) concentrations-C2500.....94
Figure 6-2: a) Galvanostatic cycling and Coulombic efficiencies,b) Charge and discharge capacity of the cell with STD.W 96
Figure 6-3: a)FESEM image of lithium surface, b) sulfur mapping on the surface of lithium,c)extracted polysulfides from separator of the cell with STD.W 97
Figure 6-4: a)Galvanostatic cycling and Coulombic efficiencies, b) Charge and discharge capacity of the cell with STD.C 98
Figure 6-5:a)FESEM image of lithium surface,b)sulfur mapping on the surface of lithiumc) extracted polysulfides from separator of the cell with STD.C 99
Figure 6-6: UV-Vis spectra of standard electrolyte 100
Figure 6-7: The chemical structure of a) N-methylpyrrolidine, b) 1-bromoropane 102
Figure 6-8: The chemical structure of N-Methyl-N-propylpyrrolidinium bromide 102
Figure 6-9: N-methyl-N-propylpyrrolidinium bis(trifluoromethanesulfonyl)imide 103
Figure 6-10: Ionic liquid separator wetting a) Fiberglass-Whatman, b)Celgard-C2500.....104
Figure 6-11:Diffusion-Solubility test a)initial, b) after 6 hours, c)after one day 105
Figure 6-12: Extracted from separator of the cell with IL.C.....105
Figure 6-13: a) Galvanostatic cycling and Coulombic efficiencies, b) Charge and discharge capacityof the cell with IL.C 106
Figure 6-14: a) FESEM image of lithium surface, b)sulfur mapping on the surface of lithium,c)extracted polysulfides from separatorthe cell with IL.W....107
Figure 6-15:a) Galvanostatic cycling and Coulombic efficiencies, b)Charge and discharge capacity of the cell with IL.W 108
Figure 6-16:UV-Vis spectra of pure Ionic Liquid electrolyte.....109
Figure 6-17: Conductivity Arrhenius plot for electrolytes with Ionic Liquid Additive 110
Figure 6-18: Galvanostatic cycling of the cells with ionic liquid additive electrolyte 10, 20, 50% 111
Figure 6-19: a) FESEM image of lithium surface, b)sulfur mapping on the surface of lithium, c) extracted polysulfides from separator of the cell with STD.IL.C 112
Figure 6-20: a) Galvanostatic cycling and Coulombic efficiencies, b) Charge and discharge capacity of the cell with STD.IL.C 113

Figure 6-21: a) FESEM image of lithium surface, b)sulfur mapping on the surface of lithium, c) extracted polysulfides from separator of the cell with STD.IL.W 114
Figure 6-22: a) Galvanostatic cycling and Coulombic efficiencies, b) Charge and discharge capacityof the cell with STD.IL.W 115
Figure 6-23: UV-Vis spectra of the hybrid electrolyte 116
Figure 6-24: a) FESEM image of lithium surface, b)sulfur mapping on the surface of lithium, c) extracted polysulfides from separator of the cell with STD.IL.C.W 117
Figure 6-25: a) Galvanostatic cycling and Coulombic efficiencies, b) Charge and discharge capacity of the cell with STD.IL.C.W 118
Figure 7-1: a) Galvanostatic cycling b) Charge and discharge capacity of the full cell Si@CNS/ DME:DIOX (1:1) + 1M LiTFSI + 0.25 M LiNO3 /S@HC-CNS 121
Figure 8-1: Application of nanosponges for energy storage 123

Tables

Table 2-1: Comparison between anode materials 14
Table 2-2: Physical and electrochemical properties of Carbonate solvents....20
Table 2-3: Physical and electrochemical properties of ether solvents 20
Table 3-1: Dimensional characteristics of different cyclodextrins 24
Table 3-2: Contact angle, Oxygen and Water permeability of membrane prepared by dispersion of four nanosponges in PVdF 34
Table 3-3: Contact angle, Oxygen and Water permeability of membrane prepared by dispersion of CITR-NS nanosponges in PWC.....34
Table 3-4: Specific surface area, cumulative pore volume and pore of carbons prepared by nanosponges.....36
Table 3-5: XPS elemental analysis.....39
Table 3-6: Specific surface area, cumulative pore volume and pore of HC-CNS 43
Table 4-1: Result of different strategies for reduction of Graphene Oxide. The specific capacity was considered after at least 50 cycles.....52
Table 4-2: Specific surface area, cumulative pore volume and pore of Si3@CNS.....69
Table 6-1: Effect of salt and solvents mixture ratio on the ionic conductivity 93
Table 6-2: Composition of electrolytes with Ionic Liquid Additive.....109

LIST OF SYMBOLS AND ABBREVIATIONS

CNS: Carbonized nanosponge
CD-NS:Cyclodextrin-based nanosponge
CDI-NS: 1,1′- Carbonyldiimidazole nanosponge
HMDI: Hexamethylene diisocyanate
PMDA-NS: Pyromellitic Dianhydride Nanosponge
CITR: Citric acid Nanosponge
PVdF: Poly(vinylidene fluoride)
PEEK: Polyetheretherketone
Si@CNS: Silicon embedded in carbonized nanosponge
Si3@CNS: Silicon with silica passivate layer embedded in carbonized nanosponge
HC-CNS: Hierarchical Carbon
S@HC-CNS: Sulfur infiltrated in hierarchical Carbon
EIS: Electrochemical Impedance Spectroscopy
PYR13TFSI- N-methyl-N-propylpyrrolidinium bis(trifluoromethanesulfonyl)imide
TEGDME: Tris Ethylene Glycol Dimethyl Ether
P1,2O1TFSI: N-methoxyethyl-N-methylpyrrolidinium bis (trifluoromethanesulfonyl)-imide,
PP13-TFSI: N-methyl-N-propylpiperidinium bis(trifluoromethanesulfonyl)imide
DME:1,2-dimethoxyethane
SiNPs: Si Nano Particles
PVDF: poly vinylidene fluoride
NMP: N-methyl-2-pyrrolidone
CTAB: Hexadecyltrimethylammonium bromide
PAM: Polyacrylamide
CMC: Carboxymethyl Cellulose
SA: Sodium alginate
FEC: Fluoroethylene Carbonate

Chapter 1 Energy Storage

1.1 Introduction

Energy is one of the most challenging fields in the development because of its relation with numerous fields such as economy, industry, environment, transportation and even well-being of the people of a society. Because of its vicinity with a lot of sectors, energy sector has bigger challenges to face and overcome. The challenges which seems to exist in actual energy filed, can be seen as follows: the depletion of oil resources, meet energy security, climate change and environmental issues and obtaining sustainability in world level.

As the technology develops, the need of primary energy sources - and especially oil- increases but this increment is not coupled with the renewal rate of the conventional energy resources. At the other hand, supply and transport of energy requires security and it is achievable through a diversified energy system and an adequate energy infrastructure. Furthermore, the effects of climate change due to the increase of the CO_2concentration in the atmosphere and increase of the average temperature of the earth and consequently the increasing sea level, are so evident that it is necessary to interfere quickly to reduce and mitigate its effects as much as possible. In between, the pronounced role of energy production and transition sector on climate change is not deniable.

The continuous growth in the world population and subsequently the increment of energy consumption in residential level and increase in the usage of transport vehicles are the other challenges that decision makers must face in the coming years. Due to IEA, the total primary energy consumption of the world is estimated to increase by 47% between 2008 and 2035. In the same period, the electricity demand of the world is estimated to grow by a factor of 90%. The main electricity consumers will be developing countries (with 80% of increase in consumption) and not anymore the developed countries. To fulfill all above mentioned necessities of energy market, energy sources utilization and energy production need to undergo changes although the fossil fuels seems to remain principal actors of the energy market. Figure 1-1 reveals the trend by sources in 50 years.[1]

The transition towards renewable energy sources is one possible way to reach in an efficient way the requirements of the actual situation of the energy market in the world. Obviously, this task needs both governmental initiatives and technological innovations. As the efficiency of the renewable energy production technologies has increased meaningfully in the recent years, as a consequence, their application in the energy sector is become more meaningful and convenient than before. Unlike the conventional energy resources, they could be implement in different locations even independently from present infrastructures. One example are the Micro and Mini grids feed by photovoltaic cells or wind turbines used off grid and in difficult accessible zones especially in Africa.

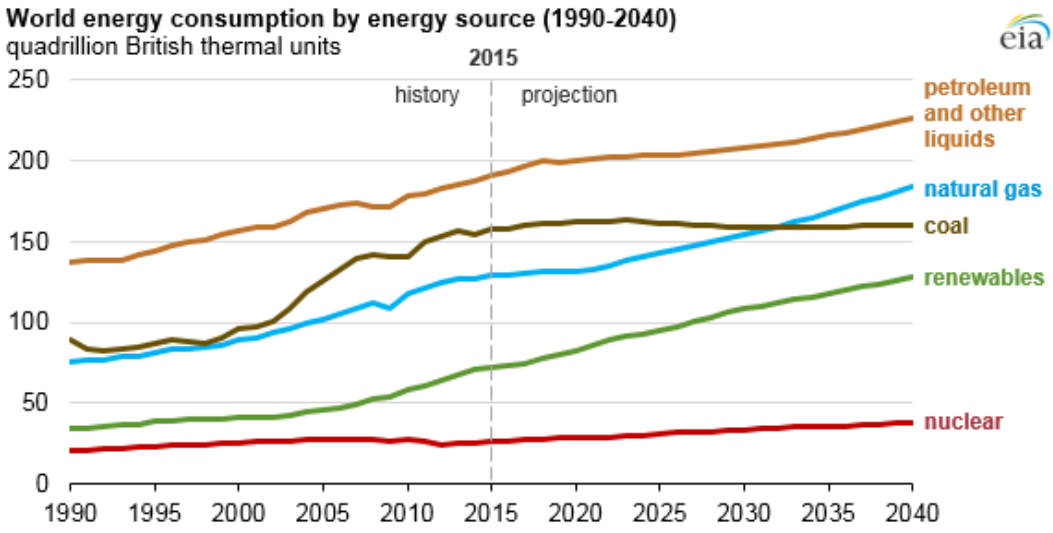

Figure 1-1: Energy consumption trend by sources in 50 years

The highly dependence of global warming on energy production and consumption and obligations of Paris agreement, make it necessary to choose a long term strategy by each country to reduce environmental impact of energy sector. For this purpose, a total revision in all consumption sectors such as Industrial, Agricultural, Residential and Transport is required. Apply a LCA (Life Cycle Analysis) model in every industrial processes are needed to avoid counterproductive plan and actions.

Paris agreement, result of the 21th Conference of Parties (COP21) was a turning point to achieve an international accordance towards the reduction of the speed and mitigation of the effects of climate change. In the frame of this agreement, the developed countries will assist developing countries to implement green technologies and help the more vulnerable countries to adapt theirselves with and mitigate the effects of the climate change as much as possible.[2] Some main elements of the agreement are listed below:

- Limiting the global temperature increase level below 2°C
- Peak the global greenhouse emission by making a balance between anthropogenic emission and Green House Gas removal
- Make possible the transformation of climate safe technologies via international cooperation and capacity building supports.
- Public training and education to increase the public awareness and participations

1.2 Renewable Energy Sources (RES)

Until 90s, the most focus regarding renewable energies was just in research and development (R&D) sector. After implementing obligations to force delivering

RES technologies in some European countries, the focus was changed towards market deployment policies. After introducing also some directives to increase the share of Renewable Energy Sources (RES) in different electricity (RES-E), heat (RES-H) and transport(RES-T) sectors, the global approach towards renewable energies has changed completely.[3] By applying governmental support instruments in above mentioned sectors, the implementation of RES in recent years is increased evidently. By the way, there are economic and non-economic barriers toward RES deployment. Through which one can point out to unfavorable administrative and legal frameworks, infrastructural, grid connected barriers, financial cost of this technologies, RES project risks etc. Between the barriers of implementation of renewable sources, also the intermittent nature of these technologies should be taken into consideration. The mismatch between demand and production and also the dependence of RES technologies on natural features such as wind and sun, decreases the reliability of them. By the way, a proper solution towards the later problem seems to use the energy storage technologies. This aspect, is the source of a lot of researches and debates between researchers and policy makers. The question, if and how much a country could rely on a 100% RES energy system, is a question that needs still to be answered.

1.3 Energy Storage Systems

Because of the reasons mentioned in the previous section, the energy production policies of the countries are changing and undergo fundamental variations and move towards implementation of circular economy and use of renewable energy sources in the energy park of the countries. Although this transition helps to reduce the effect of carbon emission and global warming, increases the possibility of temporary loss of production or have an uncover energy demand. The necessity of storage the energy independently from its production way is an important issue. On the other hand, one of the most important implications of energy sustainability criteria is to increase energy accessibility for the people in all countries around the world. To reach such a requirement, in difficult accessible zones or in developing countries, local grids feed by renewable energy sources such as off grid photovoltaic cells or wind turbine are installed. Such structure has a high dependency on storage techniques.

Among the benefits of Energy storage, the following options could be mentioned [4]:

- Improvement of quality and reliability of energy systems
- Increase the stability of transition and distribution
- Improve the RESs resilience
- possibility of utilization of existing technologies and decrease the upgrade cost of systems
- Improve the availability of distributed generation systems

Generally, the methods for Electrical Energy Storage can be classified in six categories:[5]

1-Mechanical (pumped hydroelectric storage, compressed air and flywheels)

2-Thermal energy storage (sensible heat storage and latent heat storage)

3- Thermochemical (solar fuels)

4- Chemical (hydrogen storage with fuel cells)

5- Electrical (capacitors, super capacitors and superconducting magnetic energy storage)

6-Electrochemical (conventional rechargeable batteries and flow batteries)

1.4 Electrochemical Power Source

Electrochemical storage systems are able to transform electric energy in chemical form and vice versa. Electrochemistry as can be deduced from its name, is a field that correlates electricity and chemistry. The oxidation-reduction (redox) reactions are considered as a connection of these two fields. During redox reaction an element oxidates and loses electrons and the other specie receives that electron and reduces. Since two reduced and oxidated species are in physical contact, the electrons are transferred directly between them.

Different combinations of anode and cathode can provide a range of voltage and energy density. Lead–acid, Nickel–cadmium, Nickel–metal hydride, Sodium nickel chloride, Lithium-ion are the principal battery chemistry in market.

Lead-Acid batteries are mostly used rechargeable batteries. The anode is elemental Lead (Pb) and the cathode is made of PbO_2, sulfuric acid functins as electrolyte.Their application for transportation is limited because of their low energy density (50–90 W h/L) and specific energy (25–50 Wh/kg). [6]

Lithium-ion batteries after first application by Sony Inc in 1991, have dominated the market of laptops, cell phones and other electric devices.[7] However, their energy density cannot respond to the application such as electric vehicles which need battery autonomy. Different chemistries are proposed to increase the energy density of lithium batteries. The energy density is a crucial factor to increase the autonomy of electric vehicle. It means that new chemistries are needed to provide high energy density. Figure 1-2 shows a comparison between rechargeable battery technologies. The post lithium-ion batteries such as Lithium-Sulfur and Lithium-Air batteries are emerging technologies which are expected to resolve the problems of energy density in next years.

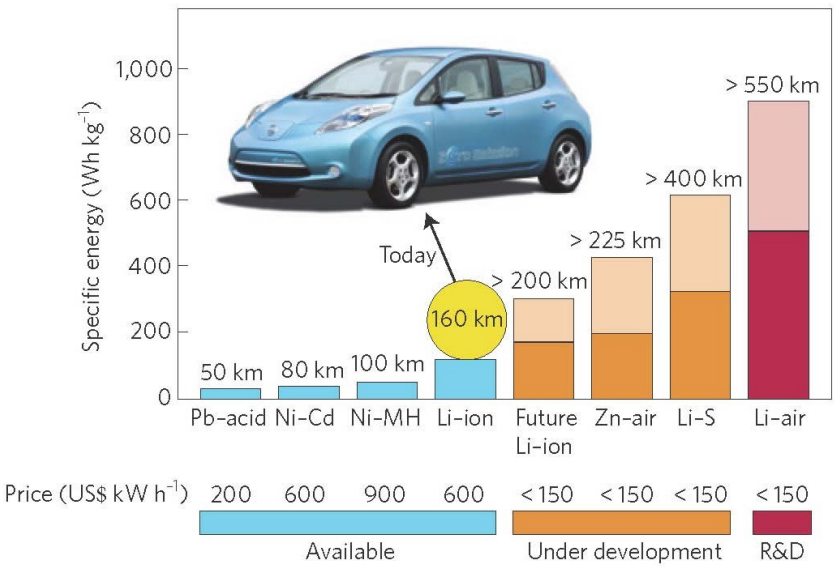

Figure 1-2:Battery technology comparison

The lithium-sulfur batteries with theoretical capacity of 1675 mAh/g and theoretical energy density of 2500 Wh/kg is a near to market technology whichcanprovidesufficientenergyformorethan400km.[10]

The abundance and fair cost of sulfur together with its eco-friendly characteristics make the application of Li-S batteries in near future possible. However, its commercialization requires improvements in cell components. Chapter 2 elucidates the general features of the materials which are used for lithium-sulfur batteries.

1.5 E-CAR

The strategies looking towards low CO_2 emission policies, involves specifically energy and transportation sector because of their marked role in total anthropogenic emissions. The low and zero emission mobility by electrification of transport as one of the main solution to reduce CO_2 emission is the goal of many automakers and governments. Norway, Germany and France announced their decisions to ban internal combustion engines by 2025, 2030 and 2040 respectively.[8] In 2016, 27% of total emission in the EU countries was due to the transport sector which is the main cause of the air pollution in the cities.[9] Moreover, the increasing background noise and congestion level in the urban areas could be mitigated through E-car usage.[10]

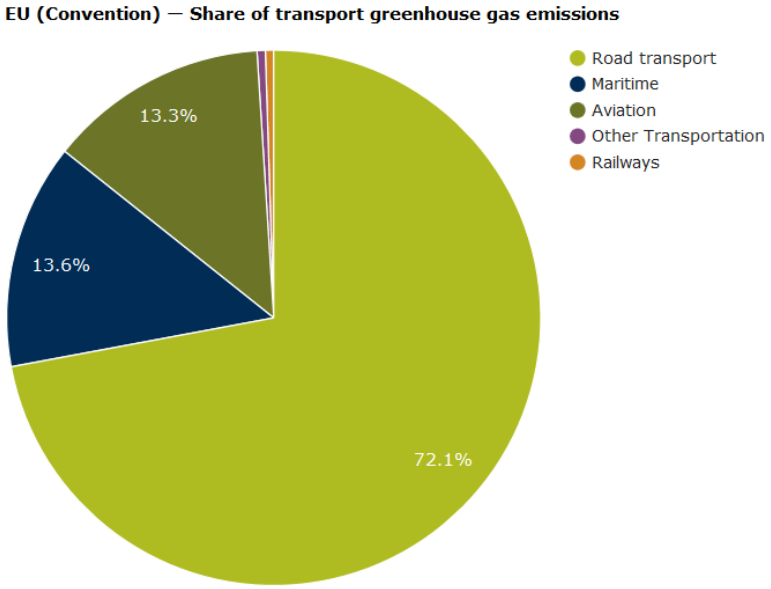

Figure 1-3: Share of transport greenhouse gas emissions

An adequate energy storage system is the main obstacle for E-car industry. The higher cost of the production of E-cars with respect to the cars running by fossil fuels is due to the battery cost and consequently, the higher cost is an obstacle for the penetration of them in the market. Also the energy density and power density together are other principal issues.

Chapter 2 Materials for lithium-sulfur batteries

The complexity of the electrochemical requires a deep knowledge of material properties, theoretical limits and industrial aspects. The functional materials which are present in electrochemical cells, must resist in the harsh chemical and electrochemical conditions. This chapter reports general features of anode, cathode and electrolyte for Lithium-Sulfur batteries.

2.1 Sulfur Chemistry

The elemental sulfur can be found in nature in many different forms as allotropes. The high tendency of sulfur atoms to form S-S bonds, can creates cyclic or linear molecules with 2 to 105 sulfur atoms. A wide range of molecular structures formation is possible by change in the S-S bond length and angle.[11]At room temperature and pressure the orthorhombic structure is the most thermodynamically stable form of sulfur. Orthorhombic sulfur is also called rhombic sulfur (α-sulfur) having S_8crown structure. The rhombic sulfur α-S_8 at 98ºC transforms to β-monoclinic sulfur structure. This allotrope remains stable up to its melting point around 120º C.[12]There is no big difference between the geometry of these allotropes. In the liquid phase an equilibrium forms between the S_8 and other cyclic structures, such as S_6, S_7, S_9, S_{12}. The viscosity of liquid sulfur depends on the equilibrium between the different rings and the lower viscosity is reachable in the temperature range 154º C- 159º C. [13] In chapter 5 the application of this property for preparation of sulfur-carbon cathode by melt infusion is explained.

The ability of accepting two lithium cations for each sulfur molecule, makes it a possible high capacity cathode material. Moreover, due to the abundance, low cost and eco-friendly properties, sulfur has become a promising cathode material for post lithium-ion batteries. The insulating nature of elemental Sulfur (conductivity of 10^{-10} S/cm) is the first challenge to tackle. Normally a carbonous matrices can provide a conductive network to increase the electronic conductivity. The sulfur/carbon ratio and its distribution in the carbonous matrices are the factors which determine the sulfur utilization. The dissolution of sulfur reduction products (polysulfides) in electrolyte is a crucial parameter for sulfur utilization. During sulfur reduction, when lithium ions reach to the cathode, they can react with sulfur atoms in the surface. If these products are soluble in the electrolyte, the sulfur atoms in the inner layer or bulk can participate in the reaction, otherwise the reduction of sulfur will stop. [14]

The dissolved PS in organic electrolyte can migrate to anode side and can react with lithium anode. This phenomenon is called shuttle effect which means a chemical reaction on the metallic lithium occurs instead of electrochemical in the cell. These problems are main drawbacks that limit the commercialization of lithium-sulfur batteries.

An ideal sulfur cathode must satisfy three main requirements as below;

1. Create electronic and ionic pathway with intimate contact between sulfur particles and conductive matrices.
2. Increase the utilization of sulfur active materials.
3. Block the polysulfides from shuttling by hosting the electrochemical reaction products in the proximity of the surface.[15]

2.1.1 Sulfur reduction intermediate products

The reduction of elemental sulfur occurs in different steps and intermediate products in each step, which are developed due to their specific potential. The initial studies performed by H. Yamin, reveals the presence of a series of intermediate sulfide species. They used cycling voltammetry to investigate the redox equilibrium mechanism and determination of chain lengths and concentration of polysulfides.[16]Dominko et al, applied an in-situ cycling voltammetry to determine quantitatively soluble polysulfides. Their study shows the highest concentration of polysulfides at the beginning step of cell operation.[17]

2.1.2 Polysulfide Thermodynamics

The theoretical capacity of Li-S battery is achievable by the reduction of sulfur in one step in which the transferred lithium cations through the electrolyte meet the electrons reached on the conductive matrix and react with elemental sulfur atom based on the:

$$\mathbf{16}\boldsymbol{Li^{+}} + \boldsymbol{S_8} + \mathbf{16}\boldsymbol{e^{-}} \rightarrow \mathbf{8}\ \boldsymbol{Li_2S_2}$$

The hypothetic one step reduction reaction is not possible because of the factors which kinetically and thermodynamically affect the formation of reduction products. The solubility of elemental sulfur in organic solvents ($S_8(s) \rightarrow S_8(l)$), causes a loose of active material. The cyclic crown shape of sulfur(S_8) forms a non-polar molecule, which facilitates its dissolution in many organic solvents having C=C bond.[18] Sulfur in the liquid phase cannot participate in electrochemical reaction because of lack of electronic contact. The rest of elemental sulfur which is in a direct contact with the surface of carbon matrix, can be reduced in different cell voltage. The cyclic crown shape of S_8 can be transformed in a long linear chain composed of two lithium atoms and eight sulfur in an opened ring. The solubility of the intermediate polysulfide products and their voltage characteristics are the main factors which determine the thermodynamic and kinetics of reaction. Zhang applied Cyclic Voltammetry (CV) t*o*better understand the mechanism of sulfur reduction. [14] The reduction was supposed to have four phases as below;

First phase: Reduction from elemental sulfur to $Li_2 S_8$

At high voltage around 2.2-2.3V, the elemental S_8 reacts with lithium ion cause to break S_8 ring. The formed Li_2S_8 dissolves into liquid electrolyte to become a

liquid cathode. This reduction plateau was observed at first reduction peak in 2,25V of Cyclic Voltammetry. This stage can go on until depletion of elemental sulfur which causes numerous voids in the cathode.

Second phase: Reduction from the dissolved Li_2S_8 to low-order polysulfides

With increase in the population of Li^+ in the cathode side, the voltage decrease constantly and the chemical reactions start to produce intermediate PS with shorter length. This increase in the number of Lithium Polysulfide cause increase in viscosity then reaches a maximum value in the end of the discharge region.

$$\mathbf{Li_2S_8 + 2\ Li \rightarrow\ Li_2\ S_{8-n} +\ Li_2S_n}$$

$$\mathbf{Li_2S_8 + 2Li \rightarrow Li_2S_{8-n} + Li_2S_n}$$

Third phase: Reduction from the dissolved low-order polysulfides to insoluble ones

The relatively high concentration of PS intermediate, increase the probability of efficient collision between Li^+ and PS. In the voltage around 1.9-2.1V, two main reactions are possible which can produce insoluble Li_2S or Li_2S_2. This phase provides a higher share of the overall capacity.

$$\mathbf{2Li_2S_8 + (2n\text{-}4)\ Li \rightarrow nLi_2S_2}$$

$$\mathbf{Li_2S_n + (2n\text{-}2)\ Li \rightarrow nLi_2S}$$

Fourth phase: Reduction from insoluble Li_2S to Li_2S_2

Non-conductive and insoluble nature of the components involved in this reaction, make it a very kinetically slow reaction. This phase has negligible effect on the cell capacity. In all phases the soluble intermediate reduction products (lithium polysulfides) can migrate to the anode side and react chemically with lithium metal instead of electrochemical reaction on the cathode.

In literature there are many studies reported which try to suppress the polysulfide dissolution and shuttle effect. In this chapter three principal strategies are discussed;

1-Anode strategies:

These strategies provide a system to protect metallic lithium against the polysulfide species by covering it with a polymeric or ceramic layer or substituting metallic lithium with alternative anode materials.

2-Cathode strategies:

This approach consists in designing cathode materials with sulfur embedded in a conductive matrix to confine all reduction reactions in porous cathode.

3-Electrolyte strategies:

Electrolyte being the main component involved in the dissolution of PS, it is the main subject of researches. The type of solvent, additives, the salt concentration are the parameters which affect directly the PS dissolution.

In this work three innovative methods are introduced to mitigate the principal issues of lithium-sulfur cells. Silicon alternative anode, hierarchical cathode and ionic liquid-based electrolyte are discussed in chapters 4,5 and 6 respectively.

2.2 Materials for Anode

2.2.1 Lithium metal anode

Lithium metal with high theoretical specific capacity (3860 mAh/g) and low negative redox potential (−3.040V) is the first candidate as anode material. However, there is a drawback involved in such choice. In the rechargeable Lithium Metal Batteries (LMBs), lithium continuously is plated on or stripped from substrates during charge/discharge cycling. The crystal defects and grain boundaries on the metal surface induce a continuous random deposition which causes an asymmetric lithium accumulation on specific points.[19] This asymmetric accumulation draws to lithium dendrite formation. Such growth of the lithium dendrite decreases the safety and performance of battery. [20] Dendrites can penetrate in the separator and, reaching the cathode, bring the cell to short circuit and subsequently thermal runaway and in extreme case electrolyte combustion and cell explosion. [21]Dendrite formation is common also during electrodeposition or solidification of a metals in molten state. Multi-branched structure with different morphologies such as tree-, bush-, moss- and needle-like of dendrites can be observed. Figure 4.1 give an idea how lithium dendrite can pierce the separator and cause short cycle.[22]

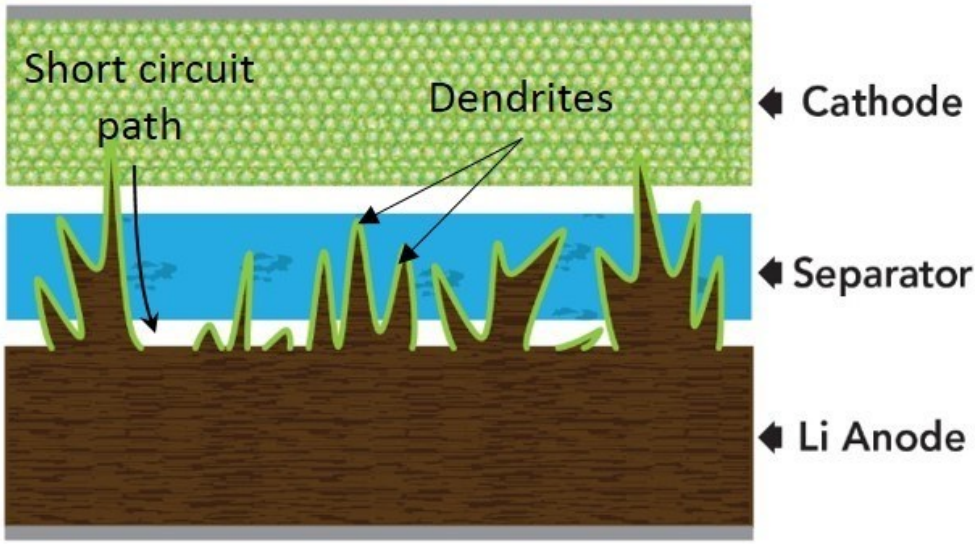

Figure 2-1:Lithium dendrite

Despite different methods applied to prevent such phenomenon including the use of ceramics and polymers as lithium protection or employing electrolyte such as polymer electrolyte and ionic liquid, actually, graphite is the standard active material for commercial rechargeable lithium batteries. Moreover, in lithium-sulfur batteries the presence of metal lithium electrode favors the effect of polysulfides which diffuse toward anode. Polysulfide with different chain length can react

chemically with lithium.[23]Figure 2-2 shows the effect of polysulfide shuttle on lithium metal after few cycles with polymeric separator.

Figure 2-2: Effect of polysulfide on lithium metal

2.2.2 Carbon-based anode

Low cost, availability and its low intercalation potential made the carbonaceous materials the most attractive choice for anodes in practical Li-ion cells. The lithation of graphite is based on intercalation of Li^+ between graphene layers of graphite. In this process the electrons are exchanged between the host layers by involving *s* and *p* electrons ($2s^2$ and $2p^4$). In crystallographic structure of graphite, the distance between planes are 0.335 nm, which facilitates the insertion of Li^+ ions. Figure 2-3.a shows distance between layered structure of hexagonal graphene sheets.[24]

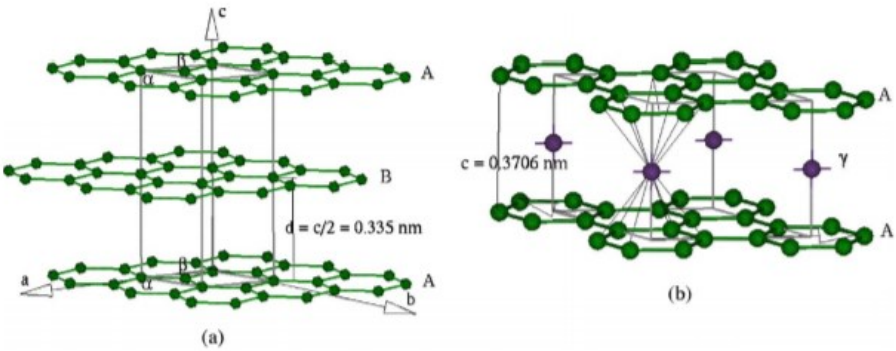

Figure 2-3: Lithium intercalation in graphite

The mechanism of lithium intercalation in graphite is well-identified. It occurs in reversible stages, corresponding to progressive intercalation which can reach the formation of LiC6 with a maximum theoretical capacity of 372 mAh/g. Figure 2-3.b depicts intercalated lithium between graphene layer of graphite.

$$\mathbf{Li + 6C \leftrightarrow LiC_6}$$

There are continuous researches in progress to improve the specific capacity of carbon materials. Generally, carbon-based anode can be divided in two main categories; soft carbons (graphite and graphitizing carbons) and hard carbons (non-graphitizing, glass-like carbons) which are expected to deliver higher capacities (500-700 mAh/g) .[16] To respond to the market requirement for batteries with higher energy density, anodes with higher specific capacity are needed. In the next section, alternative anodes with alloying mechanism are presented.

2.2.3 Anode alloying materials

Anode was intensively studied by a number of research groups with the strategies such as compound technology which synthesizes lithium composite with different number of components as anode material. The commonly used compounded materials include C-Li, Si-Li, Si-C-Li, Sn-C-Li structure.[25]

Between these compounds, the alloy anodes are promising materials for Lithium batteries due to their high specific capacity (almost 2-10 times higher than Graphite). In addition, they provide a higher safety respect to the metallic lithium. Despite these benefits their commercialization is limited by high initial irreversible capacities and rapid capacity fade during cycling. Large volume changes (up to 300%) during lithiation/delithiation is the main challenge of using alloy anodes. Such changes in volume of the structure causes pulverization of the active material and poor cycle stability. [26]

The reasons of large irreversible capacity for alloy anodes are known as the following:

I. *Loss of active material*

The cracking and pulverization of active materials caused by large volume change during cycling lead to the disconnection from the conductive carbon or current collector.[27]

II. *Formation of solid–electrolyte interface (SEI) films*

During the continues volume changes the passivate layer in the outer shell which forms in the first contact between electrolyte and anode material, breaks and more surfaces are exposed to the electrolyte. This process consumes more electrolyte and forms further layers that makes SEI layer thicker. This process causes salt-degradation and electrolyte depletion.[28]

III. *Trapping in the host alloy*

Li^+ insertion/extraction in the alloy generally leaves some Li ions trapped in the anode due to slow Li^+ release kinetics, leading to formation of highly stable lithiated compounds reducing its reversibility.[29]

IV. *Reaction with surface oxide layers*

The native oxide layer formed on the surface of metal or alloy particles during synthesis can react with Li^+ to form irreversibly Li_2O.[30]

V. *Aggregation of alloy particles*

The energy released during lithiation/delithiation induces a high mechanical stress to the structure, generating a welding effect leading to the aggregation of fine particles.[30]

2.2.4 Silicon as high capacity anode material

Silicon is an abundant element which is very rarely found as the elemental form in the Earth's crust. Commonly it is present in the form of silicon dioxide(silica) or silicates. Silicon is considered as an alternative to lithium in lithium/sulfur batteries as negative electrodes due to its high theoretical specific capacity (3580 mAh/g). The low intrinsic electrical conductivity of silicon is the first issue that must be faced. Silicon is an indirect band gap material which its electronic and optical properties depend on its dimension especially when near to the bulk Bohr radius.[31] Moreover, silicon anode suffers from fast capacity fading after the first cycles. This problem is associated to a large volume change during lithiation (up to 300%) which causes electrode active material delamination from the current collector. [32]

The lithiation of silicon forms an alloy which at fully state ($Li_{15}Si_4$) can deliver a theoretical capacity of 3580 mA h/g at room temperature.[33] This capacity can reach to 4200 mAh/g at high temperature corresponding to the formation of $Li_{22}Si_5$ alloy. [34]

Table 2-1shows the comparison between different anode materials. Silicon has both high specific capacity and volumetric capacity among all the common anode materials investigated except pure Li metal. [35]

Table 2-1: Comparison between anode materials

	Lithium	Carbon	Silicon	Tin
Lithiated phase	Li	LiC_6	$Li_{4.4}Si$	$Li_{4.4}Sn$
Theoretical specific capacity (mAh g_{-1})	3,862	372	3,580	994
Theoretical volumetric capacity (mAh cm^{-3})	2,047	837	9,786	7,246

2.2.4.1Silicon lithiation/delithation Mechanism

The mechanism of lithiation of silicon was studied by different method on the wide range of silicon nanostructures. The electrochemical lithiation of crystalline Si occurs with transformation of crystalline silicon to amorphous Si (Li_xSi) phase. The high activation energy required to weaken the Si-Si bond, is provided by high concentration of Li atoms near the reaction site. The formation of amorphous lithiated silicon can proceed to high Li/Si ratio (x = 3.75) at room temperature.[36] "The formation of highly lithiated Si at the reaction front causes most of the volume expansion to occur right at the front, which leads to enormous gradients in transformation strain. "[37]

Figure 2-4 shows discharge/charge profile of crystalline silicon. At first lithiation a crystalline-amorphous transition is recognizable which forms Li_xSi alloy. After first cycle all products of lithiation and delithiation occur in amorphous state. The reaction of silicon lithiation is;

$$xLi^+ + Si + xe^- \rightarrow Li_x Si$$

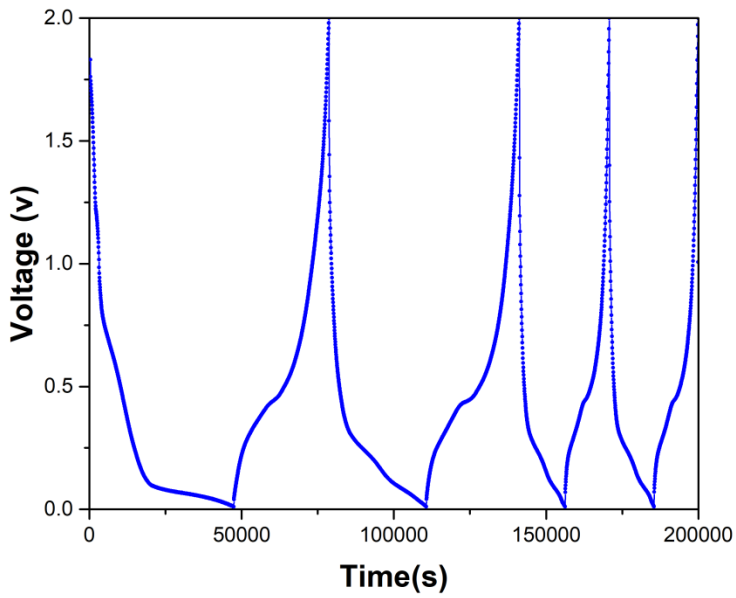

Figure 2-4: Voltage-Time profile of nano-sized silicon nanoparticles

2.2.4.2 Silicon Shape and Morphology

Different silicon morphology and shape were applied as anode active material. The structure of these materials can be classified in particle-based structures, silicon nanowires, nanotubes, nanofibers and porous silicon. Here a comparison between these strategies is reported.

In the case of particle-based structures, the size of particles is the first factor to be considered. The nanoparticles have higher specific capacity and capacity retention respect to micro-size particles because of their lower tendency and smaller volume change.[38] The nanoparticles with a conductive layer (core-shell structure) can suppress or minimize the volume expansion of silicon because of mechanical properties of amorphous conductive shell. A coating of poly vinyl alcohol(PVA) after calcination provides a capacity around 1500mAh/g.[39] Zhang et al. suggest that nanoparticles coated by polyacrylonitrile (PAN) can improve the capacity retention and avoids capacity fade of silicon.[40]

Hollow porous silicon nanoparticles coated silver shell synthetized in two steps, demonstrate high specific capacity with coulombic efficiency of 84% in first cycle which remains around 3000 mAh/g after 100 cycles. The difficulty of synthesis was the main drawback of this method .[41]

Yolk-shell structure Si@void@C was synthetized in two different coatings of silicon nanoparticles in two steps; first coating by silica layer via sol–gel method and subsequently the Si@SiO_2 particles were coated by sucrose. Calcination of sucrose and etching with Hydrofluoric acid (HF) were applied to create conductive layer and removing the SiO_2 layer. The presence of void between silicon nanoparticles and conductive layer provides a sufficient space for accommodate of silicon's volume change. This yolk-shell structure is able to provide a capacity around 800 mAh/g.[42] The low capacity can arise from lack in contact between conductive carbon and silicon nanoparticles.

"One-dimensional (1D) nanowires, nanotubes and nanofibers have the advantage of allowing the expansion of silicon radially to minimize the cracking propensity."[43] Chemical vapor deposition (CVD) was used to prepare nanowires on the stainless steel. This silicon nanowire demonstrates electronic conductivity along the longitudinal axis which made it independent of presence of conductive carbon. This anode provides a capacity around 3000 mAh/g for ten cycles.[44]

Liu et al. synthesized mesoporous silicon nanoparticles with acid wash of rice husks followed by calcination at 700 °C. Magnesiothermic reduction was used to transform as prepared nano-silica to silicon nanoparticles. A further acid etching was performed to obtain porous nanoparticles. This porous silicon provides a specific capacity around 2200 mAh/g at C/5 and 1700mAh/g at C/2. [45]

Chapter 4 introduces the use of silicon nanoparticles for preparing an innovative alternative anode for Lithium-ion and Lithium-Sulfur batteries.

2.3 Sulfur Cathode

Countless strategies were studied to improve cathode materials based on physical and/or chemical techniques. An appropriate electrical conductor can be a solution in order to create intimate contact with sulfur particles. Finding an optimum ratio between carbon and sulfur is needed to increase the electric conductivity. Moreover, designing an appropriate pores structure can enhance electrolyte wetting and sulfur utilization.

2.3.1 Carbon-based cathode

Carbon based materials are rational candidates in term of functionality, diversity and cost. Various nanostructured carbons such as one-dimensional (1D) carbon nanotube, two-dimensional (2D) Graphene, three-dimensional porous carbon were synthesized.[46] It is required to design an optimized material which provides enough space to accommodate high loading sulfur, having conductive network for electron transfer with relatively large channels for electrolyte accessibility. Moreover, this material should have the ability to trap polysulfides. In the microscopic level the structure of porous carbon materials can be considered as a defective hexagonal carbon layer planes cross-linked by aliphatic bridging groups which create amorphous structure. This morphology provides channel for electrolyte penetration and the connection creates conductive network.

Microporous carbons with pore dimensions less than 2nm, can immobilize the sulfur particles and intermediate polysulfides. Melt fusion treatment in a very low heating speed can guarantee the insertion of sulfur in micropores. However the small pore size limits the loading of sulfur to 50% in carbon matrices which dramatically reduce the capacity to 300 mAh/g. [47]

Mesoporous carbons with pore dimension in the range 2-20 nm, facilitate high sulfur loading and entrapment of polysulfide. Ji et al., suggest use of high ordered mesoporous carbon with simple melt-diffusion method which can reach 70% sulfur loading. The cell prepared with this cathode showed an initial reversible capacity around 1000 mAh/g.[48]

2.3.2 Titanium-based cathode

The application of Titanium-based nanostructures is another strategy which can reduce the dissolution of intermediate polysulfides. A yolk–shell nanostructure of Titanium dioxide with internal void space which can accommodate the volume expansion of elemental sulfur, provides a stable capacity over 1000 cycles by minimizing polysulfide dissolution.[49] Ding et al, suggest that in-situ formation of Li_xTiO_2 creates a ionic/electric conductor which mutually facilitates the lithium ion and electronstransportation.[50] Zhang et al, prepared a Titanium oxide-based free-standing cathode with excellent mechanical properties that is able to immobilize polysulfides. [51] In the present work cathode was not in the center of attention. A simple C/S cathode was prepared by the use of hierarchical porous carbon as reference material for electrolyte characterization (chapter5).

2.4 Liquide Electrolyte for Lithium-Sulfur Batteries

The conduction phenomenon is a cardinal point of electrochemistry systems because of its direct interaction with two sub phenomena:

1. The Electron Conduction: The motion of electrons allows the electrochemical reactions to take place
2. The Ion Conduction: Ions mass transport closes the electrochemical circuit.

This complexity and bilateral nature of conduction make it most challenging item in energy storage systems, specially optimizing these two processes. Indeed, an electrochemical reaction starts with oxidation of a specie “called reduced state” on the surface of anode to release Cation and electron. The reaction will be completed when these two species reach together on the surface of cathode to reduce the oxidant. The electrons are conducted through electrode, while, ions are conducted through electrolyte. The kinetics of these conduction process, directly affect the charge and discharge rate and cycling stability of the battery.

Electrolyte is the most critical part of lithium batteries because of its complex function and multilateral phenomena that occur during cycling. The main function of electrolyte is to conduct ions between electrodes. High ionic conductivity, chemical stability, wide Electrochemical Stability Window (ESW),

thermal stability, low volatility and not flammability are the main requirements that each electrolyte must satisfy. The ionic conductors can be classified in four categories; Liquid Electrolyte, Polymer Electrolyte, Solid Electrolyte and Ionic Liquids.

Solid electrolyte, by hindering the diffusion of polysulfide and controlling the shuttle of intermediates products, seems to be a promising solution for lithium –sulfur batteries.[52]Generally solid electrolytes are classified in two categories: ISE (Inorganic Solid Electrolyte) and OSE (Organic Solid Electrolyte). Solid electrolytes such as polymeric components, ceramic electrolytes and composite electrolytes have been used in lithium-sulfur batteries. The inherent low conductivities at room temperature is the main drawback of solid electrolyte systems. Moreover, the complexity of the manufacturing process can be another factor limiting the application of solid electrolytes. [53]The solid electrolytes show other issues like such low ion conductivity, poor cyclability and poor solid-solid interface interaction. In addition, the sulfur reduction mechanism in solid electrolytes must still be thoroughly understood.[54]

2.4.1 Conduction phenomena in liquid electrolytes

Generally, in Lithium batteries liquid electrolyte is composed of organic solvent and a lithium salt (organic or inorganic). Low viscosity and surface tension of organic solvents guarantee a perfect contact between electrode materials and electrolyte. This electrode wetting enables the electrolyte to penetrate the porous electrode structure. Moreover, facile mixture preparation by different organic solvents makes it possible to have a series of binary or ternary electrolytes. On the other hand, a suitable electrolyte requires to satisfy a compromise between all factors such as high ionic conductivity, chemical stability, thermal stability, low volatility, not flammability and wide electrochemical stability window (ESW). Designing an efficient liquid electrolyte consists of a proper selection of solvents, salts and additives to meet the above-mentioned essential factors. To better understand the macroscopic characteristics of the electrolytes, a deeper level of microscopic study over phenomenon affecting the electrolyte behavior is required.

Ionic solvation of a salt in an organic solvent as the first step of electrolyte formation depends on both salt lattice energy and solvent dielectric constant. In the electrolyte the ions are surrounded by solvent molecular shell. The salt is solved in the solvent when the bonds between ions of salt and solvent molecules is stronger than the ionic force in the solid structure. The dielectric constant of a solvent is measured by its polarity which is a principal factor affecting the dissolution of salts. In the electrolyte of lithium batteries with aprotic (non-aqueous) solvents, solvation occurs in two steps; the dissociation of lithium ion (cation) from the anion in the salt and subsequently its coordination by the solvent molecules. The coordination number and the structure of solvated ions influence the kinetic of conduction process. In the carbonate-based electrolytes the coordination number, are supposed to be between 2 and 6 but there is still no definitive answer to explain the nature of the Li^+ coordination. It is confirmed that the Li^+ is coordinated via the carbonyl

oxygen atom of the solvent. [55] The ion-dipole force between carbonate molecules and small lithium ions was calculated around -50 kcal/mol by Density Functional Theory (DFT) method.[56] This means that lithium ion has enough freedom to movement. The large anions with better distribution of their negative charge, can prevent ionic pairing and makes the cations more free and improve the conductivity.[57]

In liquid electrolyte the diffusion of ions is governed by Fick's law that is driven by decrease in molar Gibbs free energy or chemical potential difference. Indeed, diffusion is always along chemical potential gradient. [57]Diffusion phenomena is a random process which transports mass due to a gradient in chemical potential of the components in the system. In fact, the concentration gradient functions as a driving force. The structural properties and density of matter are determinate in diffusivity. Moreover, parameters such as temperature and pressure affect the diffusion drastically. The diffusivity coefficient of spherical ion in a liquid solvent is explained by Einstein-Stokes relation. The Einstein- Stokes equation explains the diffusion coefficient of a spherical particle undergoing Brownian Motion in a fluid at uniform temperature. The high conductivity maximum is a result of competing effects of number of charge carriers (ions), and viscosity of the electrolyte. The Nernst-Einstein equation correlate the conductivity to the diffusion coefficient. [58]

In liquids and solids, random jump is the mechanism of diffusion of atoms or ions which leads to position exchange with their neighbors. The kinetic of this stochastic process is Arrhenius type temperature dependent. In liquids, the dependency of diffusion on temperature is quite less than in solids. [59]

2.4.2 Liquid electrolytes categories for lithium-sulfur batteries

Favorite ion conductivity is the most evident electrochemical character of liquid electrolytes. These ion transportation properties become a disadvantage when in lithium-sulfur batteries intermediate polysulfide products can easily migrate to anode side and cause shuttle phenomenon. Different solvent categories such as carbonates, sulfones and ethers were applied for lithium-sulfur batteries.

Sulfone-based electrolytes with high-voltage stability were used in lithium-sulfur batteries. Ethyl methane sulfonate (EMS) with 1M LiTFSI, shows an oxidation stability until 5,5 v and low viscosity which results in higher ionic conductivity.[60] Both Tetra methylene sulfone (TMS) and EMS were used as co-solvent in binary electrolytes. Methyl isopropyl sulfone (MiPS) with 1M $LiPF_6$ provides an initial discharge capacity around 1080 mAh/g but the cell suffers from low cycling stability.

In many commercial batteries a mixture of cyclic and linear carbonate is used as solvent for electrolyte. The combination of high dielectric constant cyclic carbonates with low viscosity linear carbonates has synergic effect on the conductivity and performances of electrolyte. [61] Despite many experimental and theoretical studies, the solvation structure, coordination number and dynamics of lithium cations in pure and mixture of carbonate solvents is not yet well known. [62]

The common carbonate solvents which are used in lithium batteries electrolyte are reported in Table 2-2.

Table 2-2: Physical and electrochemical properties of Carbonate solvents

Solvent	ε	η (mPa.s)	bp (°C)	ʌ (mS/cm)	E (Vvs.Li/Li$^+$)
Ethylene Carbonate-EC	90	1.9	238	17	+6.2
Diethyl Carbonate-DEC	2.8	0.75	127	0.6	+6.7
Propylene Carbonate-PC	6.5	2.5	242	13	+6.6
Dimethyl Carbonate-DMC	3.1	0.59	90	2	+6.5

A mixture of carbonate solvents with the composition PC/EC/DEC (1:4:5), shows a very poor performance in lithium-sulfur cell. In the galvanostatic cycling of the cell with this electrolyte only one plateau was observed around 2.4 V and the capacity fades after first cycle. This behavior is related to the reactivity of carbonate solvent towards polysulfide species.[63]In carbonate-based electrolyte, the size of sulfur species in the cathode affects the cycling performance of Li-S cell. Zhang et al, demonstrated a stable cycling in a cell with small sulfur species with carbonate electrolyte EC/DMC.[47]

Ether-based electrolytes are common in Lithium-sulfur batteries. Linear and cyclic ether such as tetrahydrofuran (THF), 1,3-dioxolane(DIOX), 1,2-dimethoxyethane (DME), and tetra(-ethylene glycol) dimethyl ether (TEGDME), are promising due to their polysulfide solubility. TEGDME provides high specific capacity around 1200 mAh/g.[64]Table 2-3, reports some physical properties of ether solvents.

Table 2-3: Physical and electrochemical properties of ether solvents

	ε	η (mPa.s)	bp (°C)
1,3-Dioxolane-DIOX	7.0	0.57	103ºC
1,2-Dimethoxyethane-DME	7.2	0.46	85ºC
Diethylene glycol dimethyl ether-G2	7.4	0.97	162ºC
Triethylene glycol dimethyl ether-G3	7.5	1.89	216ºC
Tetraethylene glycol dimethyl ether-G4	7.7	3.26	275ºC

2.4.3 Solvent mixture

The effect of solvent combinations with different ratios on electrolytes performance were studied by in situ X-ray absorption spectroscopy (XAS). Five solvent mixture studied included; TEGDME; DOL:DME(1:1); PC:EC:DEC(1:4:5); EMS:DEC(8:1); EMS:DOL:DME(4:1:1). For the TEGDME and DOL:DME which provide highest discharge capacity, two voltage plateaus at around 2.4 V and 2.1V

were observed. Instead PC:EC:DEC and EMS:DEC electrolyte delivered very low capacity. XAS analysis revealed the similar discharge stable products in ether-based electrolytes, while in the carbonate-based solvents the reduction products are radical anions which react chemically with the solvent.[65]

2.4.4 Salt dissolution & Dielectric Constant

High dielectric constant of organic solvents facilitate the dissolution of salts and ionic transfer. The concentration of salt is a crucial factor to determine the mobility and diffusivity of ions. On the other hand, the salt concentration can drastically change the viscosity of electrolyte. As it was mentioned before the ion conductivity depends on both mobility and viscosity. The optimum salt concentration with high ion mobility and moderate viscosity can guarantee the ideal ion conductivity. Kikuko et al, suggest a mixtures of a solvent with large dielectric constant and high viscosity and a co-solvent with low viscosity and low dielectric constant to obtain synergic effect.[66]

2.4.5 Ionic liquids based electrolytes

Organic solvents have an essential role in chemical reactions and processing such as purification, extractions and cleaning. This fact is confirmed by their high industrial production which has been estimated at almost 20 million MT (metric tons) annually.[67] Volatility, toxicity and flammability are some of the issues that chemical industry must face. Moreover, solvent losses are one of the main sources of ground water and atmosphere contamination.

In recent years, Room Temperature Ionic Liquids (RTIL), organic salts which are liquids at room temperature are studied intensively as alternative solvents. Non-volatility, no-flammability and recyclability, make them eco-friendly and green solvents.[68] Walden describe ILs as "water-free salts which melt at relatively low temperatures, about up to 100 °C."[69]

Since ILs are molten salts, they contain only anions and cations. The presence of charged species, gives unique electrochemical properties which make them appropriate for energy storage applications. In addition, non-volatility and flammability can resolve the problems related to battery safety.

In ionic liquids, the attractive interactions between ions has diverse natures. It covers a range from strong forces such as hydrogen bonding, halogen bonding, dipole−dipole, magnetic dipole, electron pair donor/acceptor interactions to weak forces like van der Waals, solvophobic and dispersion forces. [70] The diversity of intermolecular forces and choice of different anion and cation make it tunable the properties of ILs. The understanding of solvent structure and the correlation with its chemical properties can give some insights on its electrochemical performance.

Generally ILs can be classified based on their proton donating ability to Protic and Aprotic molecular solvents.[71] In the Protic ILs or proton transfer, the anion is a conjugate base of Brønsted acid and the cation is conjugate acid of Brønsted base.[72]

The synthesis of (Protic Ionic Liquids) PILs are simpler than other classes of IL and the process is more economic due to absence of byproducts.

In the Aprotic ILs (AILs), the anion and cation are formed by the covalent bond formation between two functional groups. AILs generally are thermally and electrochemically more stable than the corresponding PIL. The synthesis usually is complicated, multistep and costly.

Menne et al, showed that at the same lithium ion concentration, the lithium coordination number in aprotic ionic liquids is higher than that in protic ones. The less coordinated cations move more freely which can be caused by different ion–ion interactions that influence the ion mobility. In AILs, the low level interactions between the Li^+ and $TFSI^-$ is due to sterically shielding of the IL cations.[73]

The ionic liquids should be highly purified in order to be applicable for lithium batteries. Moreover, the mixture of IL and lithium salt must provide high ionic conductivity ($\geq 10^{-3}$ S cm^{-1}) and wide electrochemical stability window to guarantee Li^+ reversible intercalation. High thermal stability is necessary for battery safety also at high-temperature. [74]

The melting point is the most characteristics property of IL. The bulkiness and asymmetry of anion and cation, avoid the crystal packing of ions and subsequently the melting point decreases. [75] Indeed the dimension and branching of anion and cation must hinder ions approaching. Among Perfluoroalkyl anions which were proposed as anion for lithium battery electrolytes, $TFSI^-$ was the best because of its wide anodic potential stability, high conductivity, thermal stability and hydrophobicity.[76]The quaternary aliphatic or alicyclic cations are the most stable ionic cations. The quaternary amines are stable even at the potential of metallic lithium.[77]Henderson et al, studied the phase diagrams of mixtures between ($TFSI^-$) salts containing Li^+ and N-alkyl-N-methylpyrrolidinium (PYR) cations. The performance of mixed salt used as electrolyte for electrochemical devices are influenced by crystalline phases.[78]The Pyrrolidinium based ILs ($PYR_{13}TFSI$) as electrolyte components, can improve the cyclability and long-term stability of electrochemical storage devices.[79]Pure Ionic Liquids as mixture of anion and cation are electrical insulators because of the electroneutrality of binary systems. Thus presence of adequate salt is necessary to release lithium cation in electrolyte.

In ternary/binary ionic liquid based electrolyte, the anion of IL must be the same anion delivered by the salt. The interaction between this common anion and the cations (released by the salt and ionic liquid) affect directly the mobility of lithium ion and the conductivity of electrolyte.[80]In the case of$PYR_{13}TFSI$ (N-Propyl-N-methyl pyrrolidinium bis (tri fluoro methane sulfonyl) imide) the choice of $TFSI^-$ anion was because of its high charge delocalization which leads to a relatively weak LiTFSIbinding.[81] However the tendency of $TFSI^-$ to form a cluster around lithium ions, restricts the mobility of lithium ions in ionic liquid electrolyte. [82]

Considering thermal and electrochemical stability, ionic conductivity and ease of synthesis, the $PYR_{13}TFSI$ was chosen as electrolyte additive. Moreover, its low polysulfide dissolution makes it suitable for Li-S battery applications.

Chapter 3 Cyclodextrin Based Nanosponges Material as Battery Components

The idea of finding a compound that satisfies the electrode requirements, indicates us to study an economic, easy to synthesize and ecofriendly material called cyclodextrin-based nanosponge. Their solubility in water, the ability of formation of inclusion complex and biocompatibility make them applicable in pharmaceutical industry as drug carrier. In this chapter cyclodextrin-based nanosponges with innovative applications in anode, cathode and membrane material for post-lithium batteries are introduced.

3.1 Cyclodextrin as Building Block

Cyclodextrins (CD) are cyclic oligosaccharides composed of glucopyranose units linked through α-1,4 glycosidic bonds which are produced from starch by enzymatic conversion. The structure can be considered as truncated cone with a hydrophilic outer surface and a slightly hydrophobic internal cavity that can host a wide range of guest molecules to create inclusion complexes (Figure 3-1). The encapsulation of bioactive compounds in cyclodextrin can protect them from cell environmental conditions and improve their aqueous solubility. Based on the number of glucose molecules, CDs are classified in three categories: α, β and γ. Table 3-1 reports dimensional characteristics of different cyclodextrins.[83]

Table 3-1: Dimensional characteristics of different cyclodextrins

	α-CD	**β-CD**	**γ-CD**
Number of sugar ring molecule	6-membered	7-membered	8-membered
Molar mass -g/mole	972.84	1134.98	1297.16
Inner diameter -nm	0.45-0.57	0.62-0.78	0.79-0.95
Outer diameter - nm	1.37	1.53	1.69
Height-nm	0.79	0.79	0.79

The peculiar structure and various forces of CDs such as electrostatic interactions, hydrogen bonds and Van der Waals interactions make possible the formation of inclusion complexes.[84] The size compatibility between host and guest molecules and the electrical charge distribution in the guest molecule are main factors that affect their complex stability.

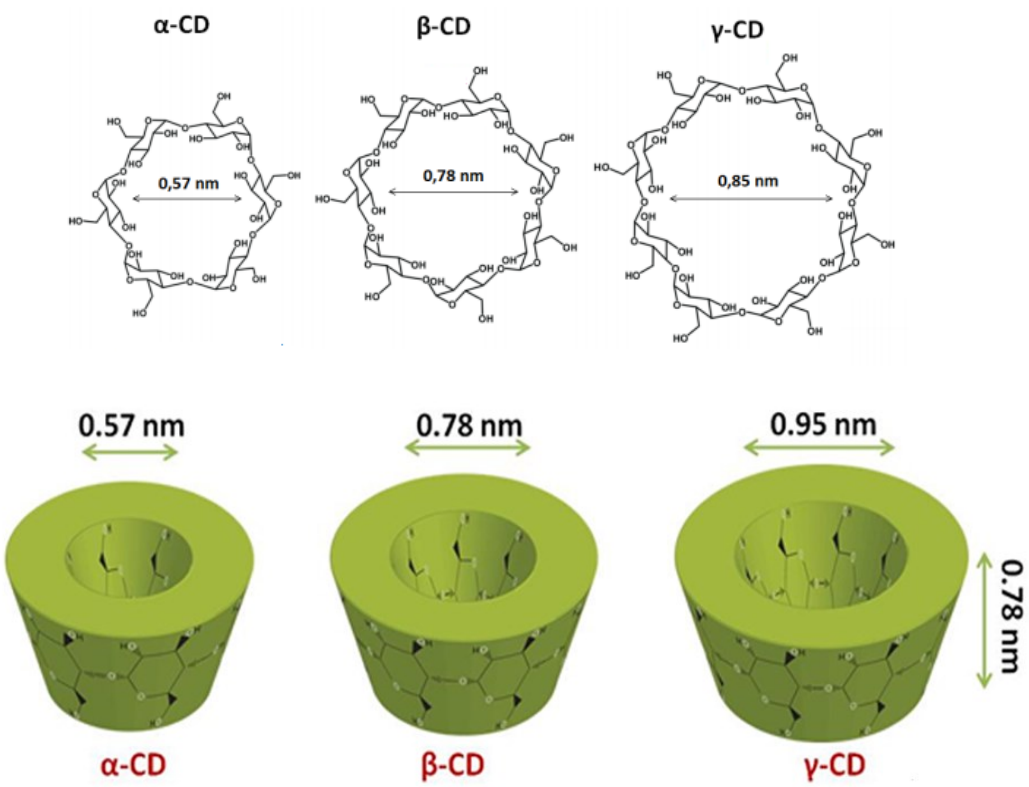

Figure 3-1: Cyclodextrin categories comparison

3.2 Cyclodextrin-Based Nanosponges (CD-NSs)

The polymerization of CDs is a method which forms nanosponges and improves their complexation ability. Owing their three-dimensional structure, NSs have the possibility to host guest molecules both inside the internal cavities of each CDs and in the enclosed volumes between CDs.[85] Cyclodextrins, can be cross-linked by using a wide variety of chemicals to obtain insoluble, three dimensional polymers. The final properties of a NS are strongly influenced by the nature of the cross-linker, the degree of cross-linking and the reaction conditions. To synthesize NSs, generally a sol-gel process is applied to form an organogel. The method consists in dissolving the β-CD in a solvent (usually dimethylformamide or dimethylsulfoxide), then a catalyst is introduced and finally the cross-linker is added. Once the product forms, the sample is washed to remove all impurities and unreacted CDs and finally a solid powder remains as NS.[85]

In this work different cross-linkers (CDI, HMDI, CITR, PMDA) were used to prepare NSs for application in energy storage. Figure 3-2 depicts the use of NSs in Lithium-Air, Lithium-ion and Lithium-Sulfur batteries. Since the application of nanosponges in Li-Air membrane and cathode in Li-S batteries are explained in details in previous works, in this chapter we summarize some of the results while chapter 4 is dedicated to their applications as Silicon-based anode for Li-ion and Li-S batteries.

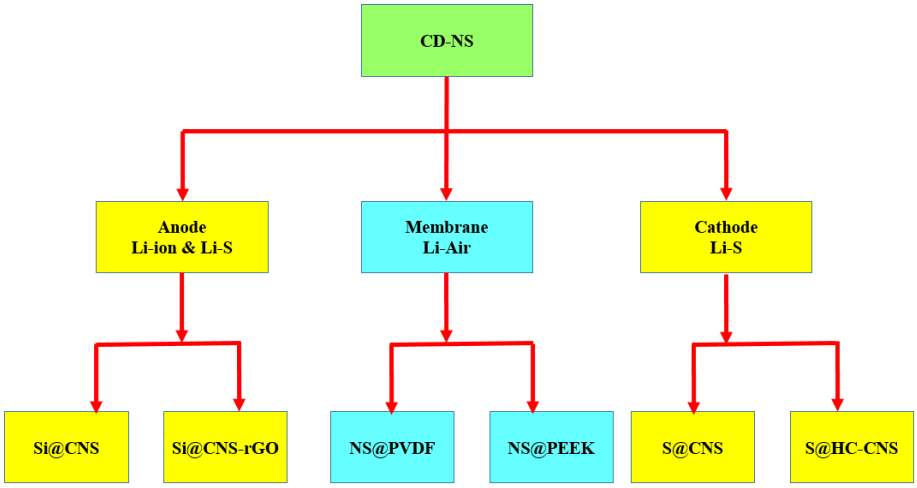

Figure 3-2: Nanosponge-based material application in battery field

3.3 Synthesis of Cyclodextrin-based Nanosponges

The presence of reactive hydroxyl groups in cyclodextrins allows them to act as polyfunctional monomers in polymerization reactions. All the nanosponges were prepared by the methods reported in a previous study by Caldera et al.[85] In this study four cross-linking agents, i.e. Carbonyldiimidazole, Pyromellitic dianhydride, Hexamethylene diisocyanate and Citric acid, were investigated.

3.3.1 Carbonyldiimidazole Nanosponge (CDI-NS)

1,1′- Carbonyldiimidazole (CDI) is a white powder (162.152 g/mol) belonging to the carbonyl active compounds family, having two imidazole groups connected to the carbonyl group. To synthetize CDI-NS, the 1:4 molar ratios of (βCD:CDI) was chosen. 0.006 mol of anhydrous βCD (6.5 g) were dissolved in 40 ml of anhydrous DMF under stirring, until complete dissolution of the βCD. After 5 minutes, 3.71 g (0.024 mol) of CDI were mixed, then the solution was heated at 90ºC under stirring, until a gel formed. Once the reaction was concluded, the monolithic gel was crashed and washed 3 times in a Buchner funnel with ethanol and water. The further purification was carried out in a Soxhlet extractor with ethanol for 24 h (Figure 3-3: 1,1′- Carbonyldiimidazole nanosponge synthesis).

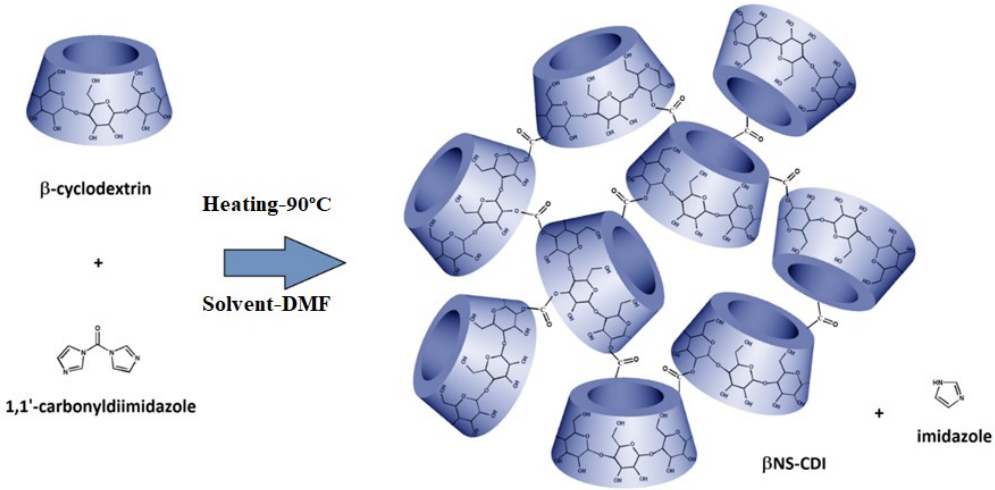

Figure 3-3: 1,1′- Carbonyldiimidazole nanosponge synthesis

TGA measurement was carried out on the CDI-NS. After an initial weight loss due to moisture evaporation, a single step thermal degradation starting at 270 °C was observed. The final carbon residue is around 20% (Figure 3-4.a). The FTIR was performed on CDI-NS to confirm cross-linking reaction. The CDI-NS shows a signal at 1739 cm^{-1} which is due to carbonyl group stretching vibration (Figure 3-4.b) .

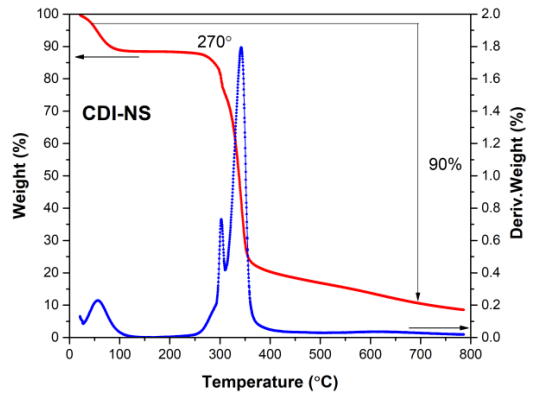

a)

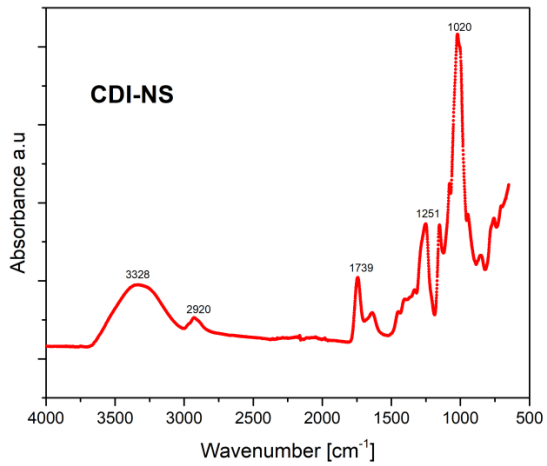

b)

Figure 3-4: a) TGA , b) FTIR analysis of CDI-NS

3.3.2 Hexamethylene diisocyanate Nanosponge (HMDI-NS)

Hexamethylene diisocyanate (HMDI) is a colorless liquid (168.2 g/mol, 1.047 g/cm^3) widely used for preparation of polyurethanes. To synthetize HMDI-NS the molar ratio (1:4) of (βCD:HMDI) was chosen. 3.91 g of anhydrous β-CD (3.44 mmol) was introduced to 16 mL DMSO under stirring to complete dissolution. Then, 0.4 g of 1,4-diazabicyclo [2.2.2] octane (DABCO) was added to the solution as catalyst. Subsequently 2.32 g of HMDI (13.75 mmol) was poured as a cross-linking agent in the solution and stirred until gel formation. In the following day, the solid block of cross-linked cyclodextrin was washed 3 times in a Buchner funnel with acetone and water. The further purification was carried out in a Soxhlet extractor with acetone for 24 h (Figure 3-5).

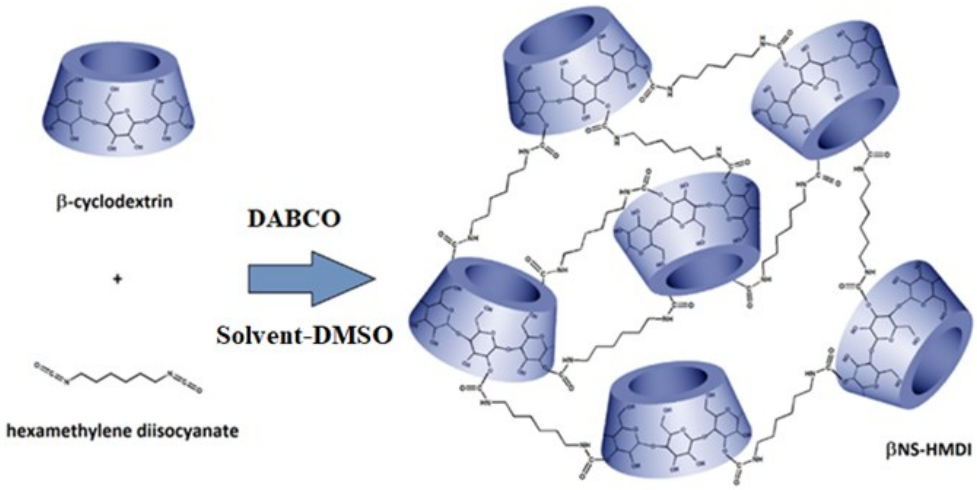

Figure 3-5: Hexamethylene diisocyanate nanosponge synthesis

TGA measurement was carried out on the HMDI-NS. After an initial weight loss due to moisture evaporation, a two steps thermal degradation at 280 and 365 ºC was observed. The final carbon residue was around 20% (Figure 3-6.a). The FTIR was performed on HMDI-NS to confirm cross-linking reaction. The HMDI-NS shows signals at 1692 cm^{-1}, 1536 cm^{-1} and 1252 cm^{-1} which are associated with carbamate groups (Figure 3-6.b).

a)

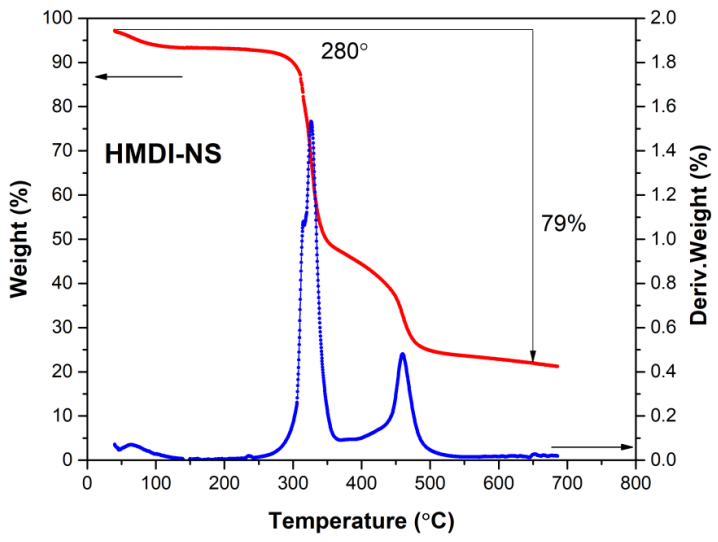

b)

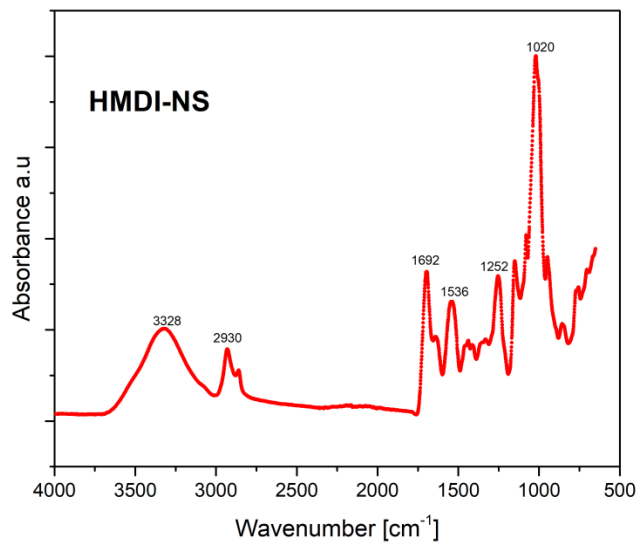

Figure 3-6: a) TGA, b) FTIR analysis of HMDI-NS

3.3.3 Pyromellitic Dianhydride Nanosponge (PMDA-NS)

Pyromellitic Dianhydride (PMDA) is a white crystalline powder (218.12 g/mol) belonging to cyclic anhydrides family. To synthetize PMDA-NS the molar ratio (1:4) of (βCD:PMDA) was chosen. 0.005 mol of anhydrous βCD (5.68 g) were added to 50 ml of DMSO, stirred until complete dissolution of the βCD. Subsequently 1.35 ml of TEA (triethylamine) catalyst was added. So after 5 minutes, 4.36 g of PMDA were mixed and for the gelation the sample left overnight at room temperature. Once the reaction was concluded, the polymer gel was crashed and washed three times in a Buchner funnel with acetone and water. The further purification was carried out in a Soxhlet extractor with acetone for 24 h (Figure 3-7).

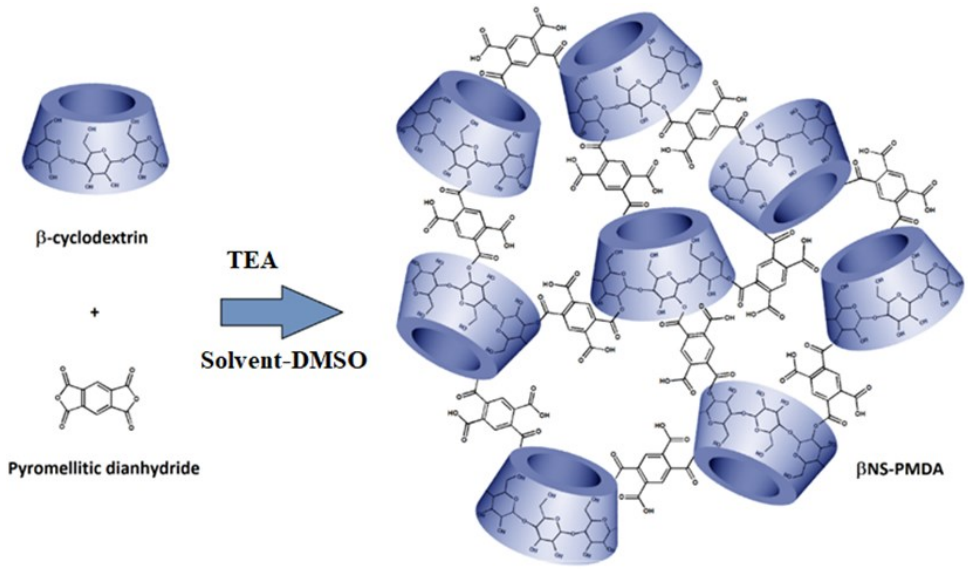

Figure 3-7: Pyromellitic Dianhydride nanosponge synthesis

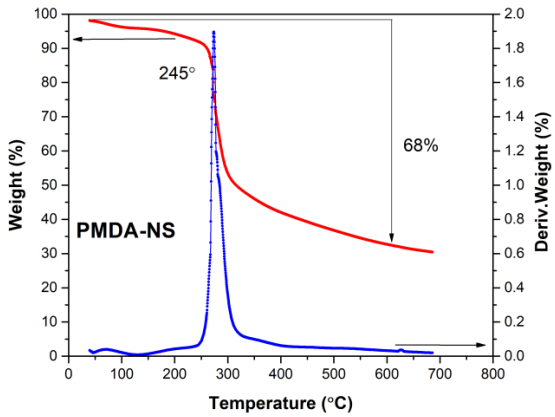

a)

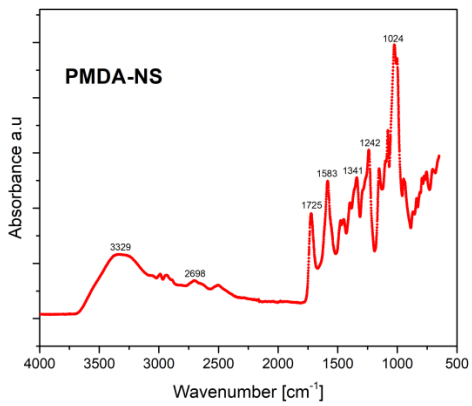

b)

Figure 3-8: a) TGA, b) FTIR analysis of PDMA-NS

TGA measurement was carried out on the PMDA-NS. After an initial weight loss due to moisture, a single step thermal degradation starting at 245º C

was observed. The final carbon residue is around 28% (Figure 3-8.a). The FTIR was performed on PMDA-NS to confirm cross-linking reaction. The PMDA-NS shows signals at 1725 cm^{-1} and 1583 cm^{-1} which are related to carboxyl and carboxylate groups respectively (Figure 3-8.b).

3.3.4 Citric acid Nanosponge (CITR-NS)

Citric acid (CITR) is a white crystalline weak organic acid with molecular weight 192.123 g/mol. To synthetize CITR-NS, the molar ratio (1:4) of (βCD: CITR) was chosen. 0.0035 mol of anhydrous βCD (4 g) were added in 20 ml of deionized water, stirred until complete dissolution of the βCD. Subsequently, 0.5 g of ($NaPO_2H_2 \cdot H_2O$) sodium hypophosphite monohydrate catalyst and 2.7 g of CITR were added. The solution was then heated in oven at 140°C for 1 h and 100°C for further 4 h under low pressure (20 mbar). Finally, the polymer was ground, washed with deionized water and further purification was performed in Soxhlet with acetone for 24 h (Figure 3-9).

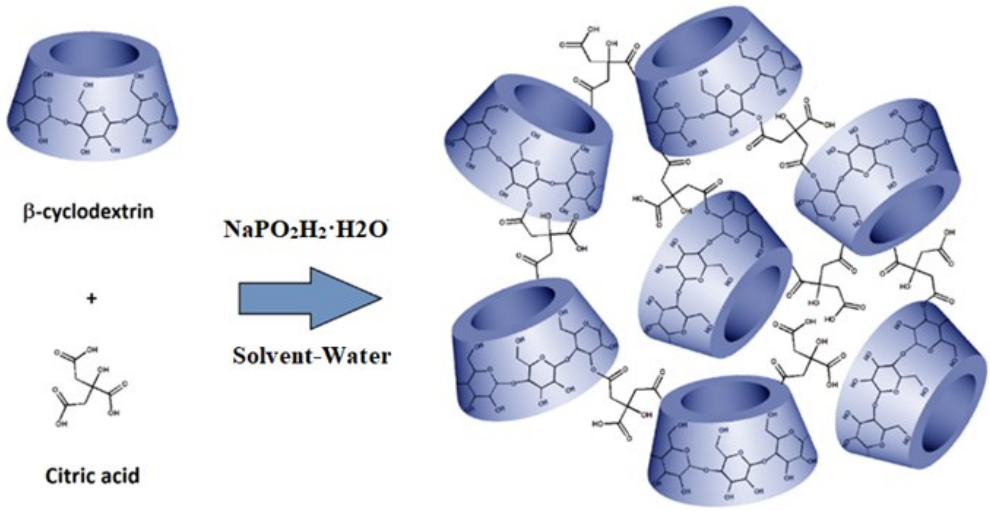

Figure 3-9: Citric acid nanosponges synthesis

TGA measurement was carried out on the CITR-NS. After an initial weight loss due to moisture, it was observed a single step thermal degradation starting at 159 ºC. The final carbon residue is around 20% (Figure 3-10.a) . The FTIR was performed on CITR-NS to confirm cross-linking reaction. The CITR-NS shows a signal at 1721 cm^{-1} which is related to carboxyl groups (Figure 3-10.b).

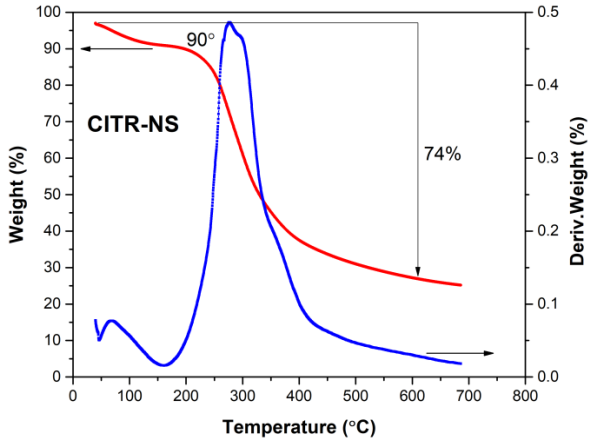

a)

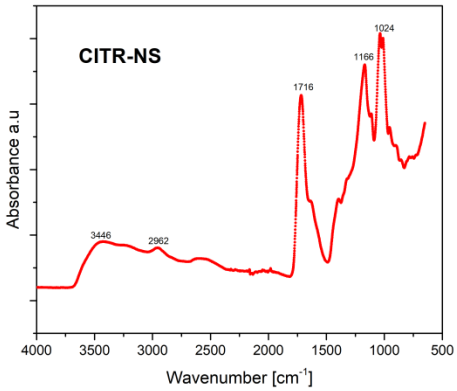

b)

Figure 3-10: a)TGA, b) FTIR analysis of CITR-NS

After drying in air, to remove the remaining low moisture quantity of nanosponges, CDI-NS, HMDI-NS, PMDA-NS at 100ºC and CITR-NS at 70ºC were dried under vacuum in Bucchi. The extra dried powders were used for as battery grade compounds for further applications (Figure 3-11).

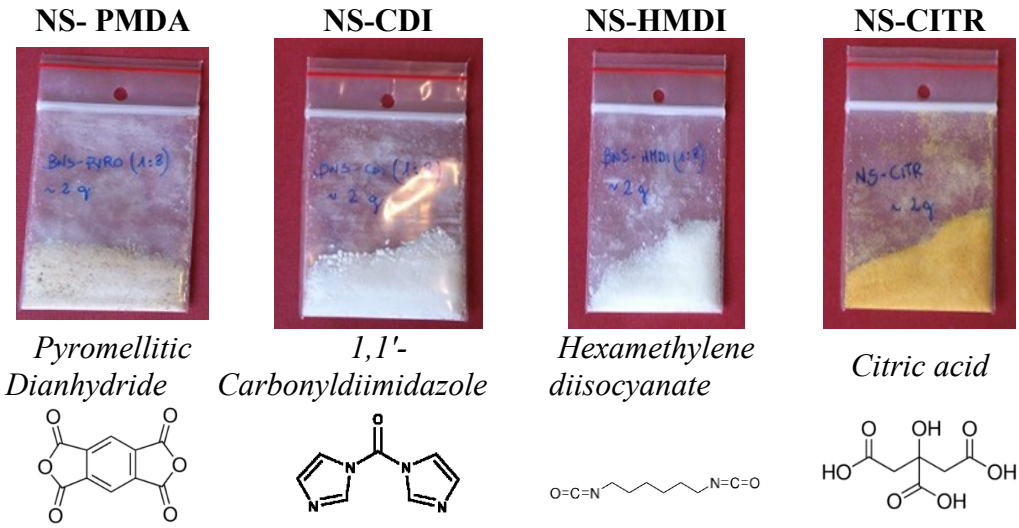

Figure 3-11: Dried nanosponges powder

3.4 Membrane for Lithium-Air batteries

The benefits of lithium-air batteries and their potential application for electric vehicles were discussed in chapter one. In the practical situation, the use of oxygen tank for lithium-oxygen batteries is not possible because of difficulties such as cost, safety, volume and weight. It means that a safe and economic source must be found for oxygen. Atmospheric air as the infinite source of oxygen is the best choice especially for its everywhere presence which can supply free oxygen in secure condition. Despite the advantages, the moisture content of the air is harmful for lithium anode and the electrochemical reactions on the cathode. The use of atmospheric air as the source of oxygen could have sense if its moisture could be blocked. To overcome this issue, an innovative oxygen-selective membrane was prepared by dispersion of nanosponges in polymeric matrix.

3.4.1 Oxygen selective membrane

The presence of hydrophobic groups inside the cyclodextrin's cavity, gives the ability to absorb and retain water molecules in the NSs. The interstitial channels which facilitate the diffusion of oxygen molecules was a clue to apply NSs as potential active components in oxygen-selective membrane (Figure 3-12). In this work, CDI-NS, HMDI-NS, PMDA-NS, CITR-NS were used for preparing four different types of polymeric membranes.

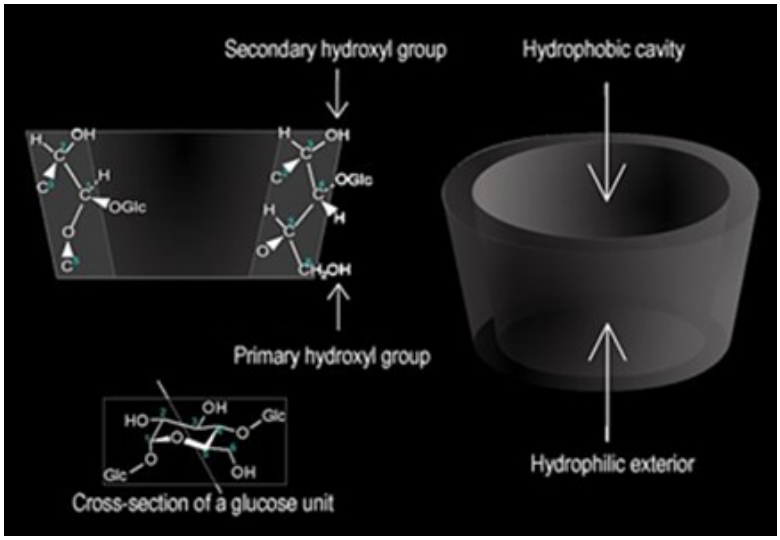

Figure 3-12: Hydrophobic cavity of cyclodextrin

All the nanosponges were prepared by the method developed in previous studies by Caldera et al.[85] Specifically, 5% of each carbonate, carbamate, pyromellitic and citrate nanosponges was dispersed in PVdF-HFP as polymeric matrix. Table 3-2: Contact angle, Oxygen and Water permeability of membrane prepared by dispersion of four nanosponges in PVdF polymer.

Table 3-2: Contact angle, Oxygen and Water permeability of membrane prepared by dispersion of four nanosponges in PVdF

Membrane	Contact angle/ °	O_2permeability (Barrer)	H_2O permeability (g m^{-2} day)
PVdF	148.72°±16	0.426	733.246
CITR @PVdF	125.4°± 5.7	3.1473	11.16
CDI@PVdF	89.1°±2.54	1.4065	7.420
PMDA@PVdF	117.5°±1.81	3.0497	9.733
HDMI@ PVdF	152.7°±8.24	0.1676	11.565

The best results were observed in the case of CITR @PVdF. The water permeability from 733.246 g/m^2.day falls drastically to 11.16 g/m^2.day. It can be seen that the addition of NS-CITR to PVdF decreased the water permeability by 98%. The result of oxygen permeability was even more interesting: The oxygen quantity in the PVDF was 0.426 Barrer while this value for the CITR @PVdF was 3.1473 Barrer. The observing increase in oxygen permeability was almost 7 times. Indeed, this membrane can satisfy two principal requirements for Li-air batteries. It decreased rigorously the penetration of water and facilitated the insertion of oxygen. The cell assembled with this membrane demonstrated stable capacity for more than 150 cycles while the same cell with another membrane stopped after 35 cycles.[86]

3.4.2 Lithium protective membrane

To evaluate the effect of the polymeric matrix, different polymers were used to prepare the membranes. The NS-CITR nanosponge in polyetheretherketone (PWC) demonstrate very interesting behavior. In this case the oxygen permeability was 0.0123 Barrer that was two order of magnitude less than the oxygen permeability in PVdF. This very low oxygen penetration, indicated us to use CITR@ PWC for protection of lithium anode in Li-air batteries. Moreover, the electrolyte uptake and ionic conductivity improved in CITR@PWC with respect to PCW. The contact angle was relatively low which means the membranes are wetted simply by the electrolyte. Since Li-air batteries are supposed to work in the absence of moisture, the low contact angle in this case is not a problem. Table 3-3: Contact angle, Oxygen and Water permeability of membrane prepared by dispersion of CITR-NS nanosponges in PWC characteristics of the membrane with and without nanosponge.[87]

Table 3-3: Contact angle, Oxygen and Water permeability of membrane prepared by dispersion of CITR-NS nanosponges in PWC

Membrane	Contact angle	O_2 Permeability (Barrer)	Ionic Conductivity	Electrolyte Uptake(wt%)
PWC	26.92°±2.74	0.4056	0.257 (mS/cm)	75

CITR@PWC	22.12°± 3.03	0.0123	0.406 (mS/cm)	305

3.5 Porous Carbon for Sulfur Cathode

The insulating nature of elemental sulfur limits its application as electrode active material in the rechargeable batteries. It means that a conductive matrix is required to host elemental sulfur to increase its electrical conductivity. Furthermore, immobilizing the polysulfide intermediate products which form during sulfur reduction in electrolyte is another issue that a cathode material must satisfy. In addition, the characterization of the electrolyte for lithium-sulfur batteries requires the use of a reference sulfur cathode. Initially, several commercially available sulfur cathodes were used, but the results were not reproducible due to different cathode compositions.

In a porous carbon material, the carbon network functions as electron conduction pathway and the pores are able to host sulfur and electrolyte. The size of pores is a factor which drastically affects the electrochemical properties of the material. Porous carbon spheres prepared by carbonization of starch were used as anode for lithium-ion battery with interesting electrochemical performance. This carbon provides a specific capacity higher than 500 mAh/g for 50 cycles.[88]

As defined by IUPAC, the pore with diameter less than 2 nm, between 2-50 nm and higher than 50 nm are respectively classified as micropores, mesopores and macropores.[89] Anceschi et al. prepared a porous carbon by pyrolysis of cyclodextrin-based nanosponges with the pore size in the range 5-15 Å.[90] Their interesting results, suggests a potential application of carbonized nanosponges (CNS) as a conductive matrix for hosting sulfur particles. Two main methods were applied for porous carbon synthesis.

i. Conventional carbonization of NS to prepare CNS
ii. Silica templated NS to prepare HC-CNS

3.5.1 Conventional Carbonization of NS synthesis to prepare CNS

The effect of catalyst, type of cross-linking agents and (cyclodextrin: cross-linking agent) molar ratio on the porosity and final pyrolysis residue was studied by Anceschi et al.[91] Among four types of nanosponges i.e. CDI-NS, HMDI-NS, CITR-NS, PMDA-NS, the last one with molar ratio 1:4 was selected as precursor for porous carbon production. The synthesis was conducted with the same method reported for typical nanosponges. A stoichiometric quantity of 0.005 mol of anhydrous βCD (5.68 g) was dissolved in 50 ml of DMSO under vigorous stirring. Subsequently, 1.35 ml of TEA was added as catalyst. As mentioned before, a 1:4 molar ratios between (βCD and PMDA) was chosen. After 5 minutes, 4.36 g of PMDA were introduced to the solution. In a few second a rigid gel was formed. In the following days, the monolithic gel was ground and washed three times in a Buchner funnel with acetone and water. Further purification was carried out in a

Soxhlet extractor with acetone for 24 h.

Carbolite Gero tubular furnace was used for the calcination of nanosponges to CNS (Carbonized Nano Sponge). 5 g of NS were loaded in alumina boats and heated at 800°C for 2 h under 100 ml min^{-1} flux of nitrogen with heating ramp of 10°C min^{-1}. Different conditions for maximum temperature and heating rate were applied and the optimal process settings were chosen based on the work of Anceschi et al.[90]

The as-prepared carbon was characterized to understand the effect of synthesis condition on the specific surface area, porosity and its morphology. For investigating the effect of pyrolysis on the physical properties of sample, ASAP2010 volumetric sorption analyzer, was used to measure N_2 adsorption–desorption isotherms at 77 K. To remove the adsorbents and moisture, first the samples were outgassed at 300°C under vacuum (10 µm Hg) for 12 h. The Langmuir equation (appropriate to describe the specific surface area of exclusively microporous systems) was applied to estimate specific surface area. The total pore volume and size were determined by means of DFT method applied to the adsorption branch of the isotherms (considering slit geometry and low regularization).

Table 3-4: Specific surface area, cumulative pore volume and pore of carbons prepared by nanosponges

Sample	Surface Area (m^2/g)	Cumulative pore Volume (cm^3/g)	Pore width (Å)
PMDA- CNS	560	0.11	5-16
HMDI-CNS	64	-----	-----
CDI-CNS	5	-----	-----
CITR-CNS	2.75	-----	-----

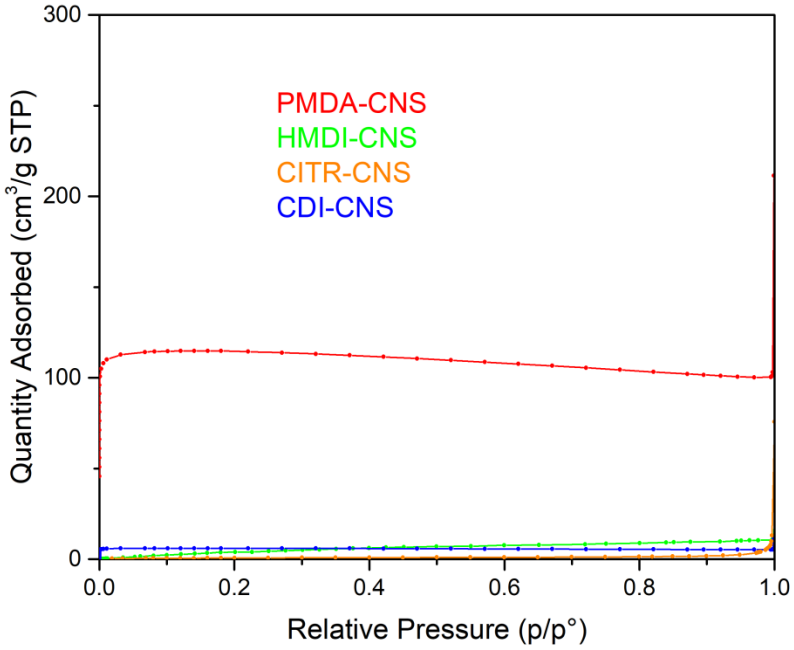

Figure 3-13: Nitrogen adsorption isotherm of different carbonized nanosponges

The nitrogen adsorption isotherm curves of different carbonized nanosponges at 77 K are shown in Figure 3-13. Among the nanosponges the PMDA- CNS is the only one that demonstrates interesting results (560 m^2 /g). The N_2 isotherm of PMDA- CNS shows the typical shape of Type I. Indeed, at low relative pressures (less than 0.02 p/p_0) a steep increase was observed which is the evidence for adsorption or condensation in micropores. The adsorption amount shows a plateau until the nitrogen saturation pressure. The presence of micropores is fundamental, as they provide space for hosting sulfur with high mass loading. In chapter 5 the preparation of S@CNS active material is explained.

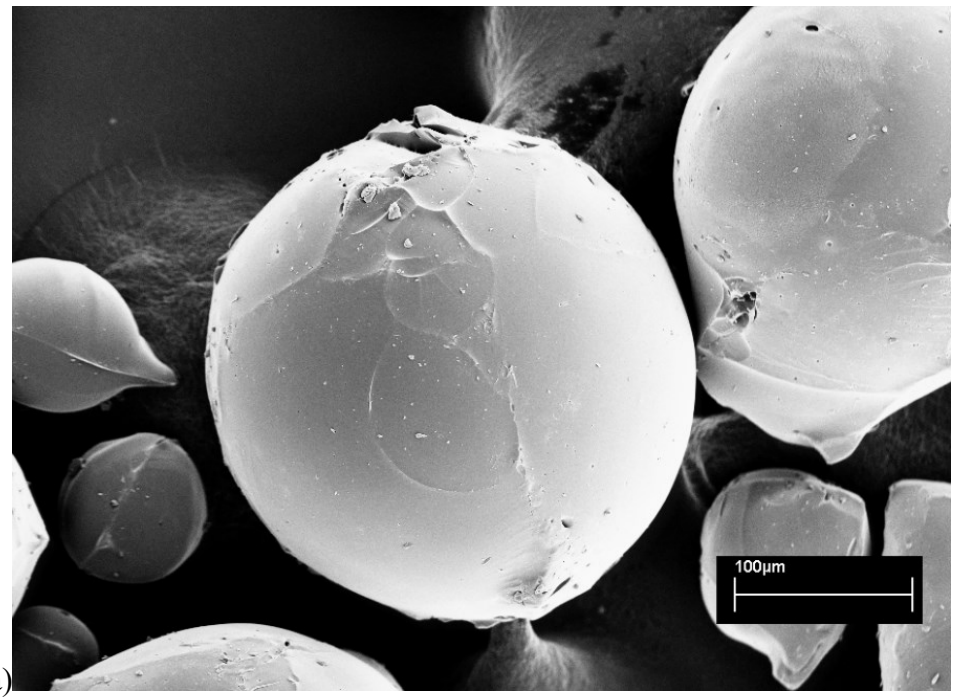

a)

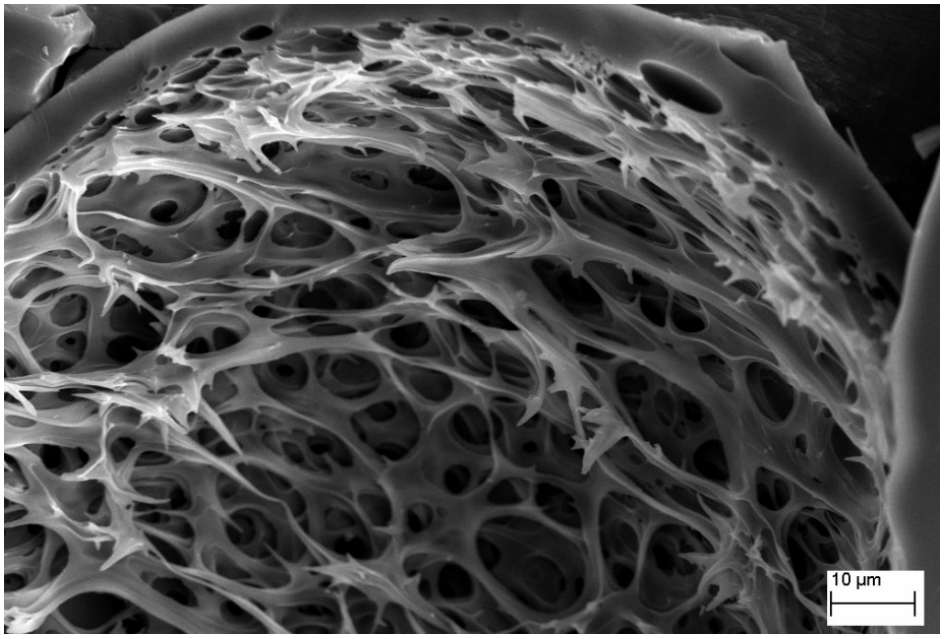

b)

Figure 3-14: Hollow carbonized nanospongesspheres

The morphology of PMDA-CNS was studied by Scanning Electron Microscopy (SEM). Figure 3-14.a shows the homogeneous spherical particles with a smooth surface which may form in the fluid phase formation, occurring before the carbonization. Figure 3-14.b demonstrates the presence of a hollow cavity inside the grinded sample. The formation of such cavities is attributed to the evaporation of volatile species generated during the thermal degradation. This low-density carbon material with twisted textural structural provides conductive matrices for electrode fabrication. Tortuous channels structures, like the ones observed in CNS, are known to provide a pathway for electrolyte accessibility. The

application of CNS as conductive matrix for lithium-sulfur batteries and its electrochemical characterization are reported in our previous work.[92]

3.5.2 Silica template NS synthesis to prepare HC-CNS

An ideal cathode must contain an acceptable quantity of active material to provide the required capacity. In addition, the electrolyte accessibility in the electrode must be facilitated. To increase the porosity and to obtain bimodal pore structure, a silica template method was applied. Hierarchically porous Carbon(HC) with both micro and meso pores could improve both sulfur loading and electrolyte accessibility. Tuning the structure and internal geometry of composite improves sulfur utilization. The distribution of sulfur on the surface and inside the pores of conductive carbon affects the specific capacity and kinetics of sulfur reduction.

To obtain hierarchically porous carbon, silica fumed powder with particles size 7nm was used as template to prepare precursor for HC. Different weight percentages of silica were used for the preparation of SiO_2@NS. The highest amount of template that can be introduced in the NS structure, without negatively impacting the gelation step, and therefore the NS formation, was found to be 20 wt%. To this purpose 2.2 g of silica were dispersed in 50ml of DMSO and kept under continuous sonication. To this dispersion, 5.68 g of anhydrous βCD were added under stirring until complete dissolution of the βCD. Subsequently, 1.35 ml of TEA (catalyst) were added. After 5 minutes, 4.36 g of PMDA were added and within 15 minutes at room temperature the gelation was completed. The procedure of purification and calcination of SiO_2 @NS was performed as explained in previous section for the non-templated PMDA-NS. Once prepared, SiO_2 @CNS was ground and washed with hydrofluoric acid (HF) to remove silica nano-particles. The etching procedure was optimized by varying the concentration of HF and time of etching process. After silica removal, the sample was washed three times with deionized water. X-ray photon spectroscopy (XPS) analysis was performed to investigate the atomic composition of the sample surface after treatment with HF (Figure 3-15).

In Table 3-5 the elemental composition of HC-CNS is reported. The very low quantity of silicon which represents silica confirms the efficiency of silica removing. In the sample the percentage of Fluorine was around 1.4%. To remove this residue, the final sample was rinsed again three times with Milli-Q water.

Table 3-5: XPS elemental analysis

Element	C	O	F	Si
Percentage	87.5	10.8	1.4	0.3

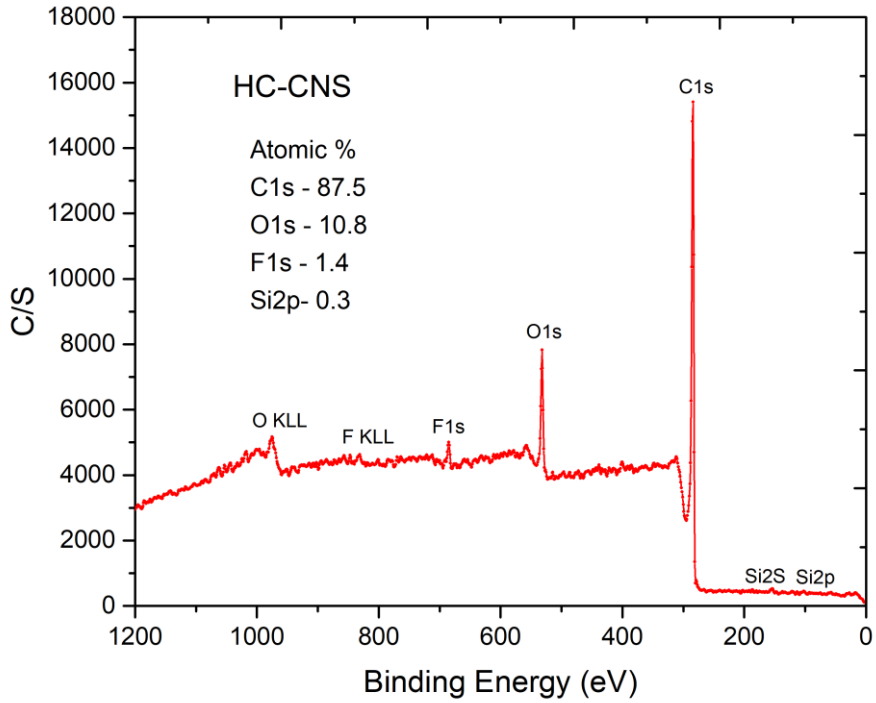

Figure 3-15: XPS spectra of HC-CNS

To investigate the morphology of the HC-CNS, Field-Emission Scanning Electron Microscopy (FESEM, JEOL-JSM-6700F) was used.

c) 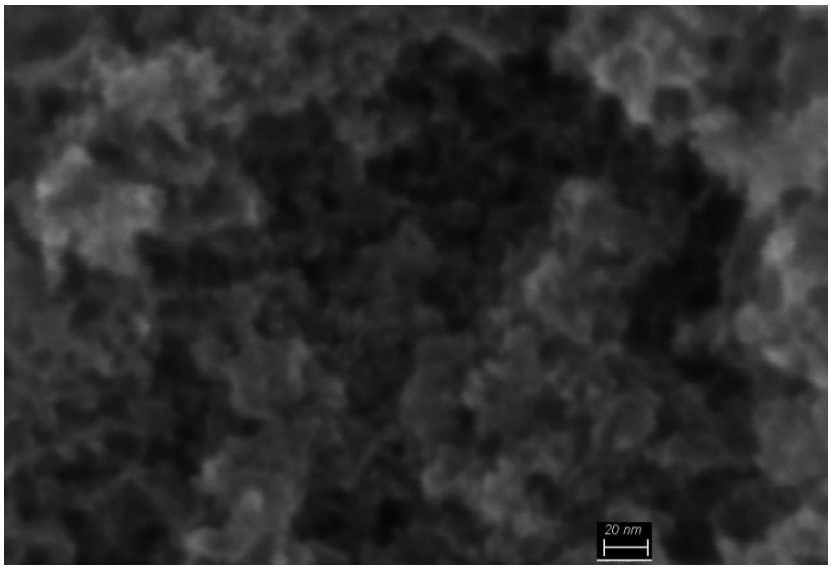

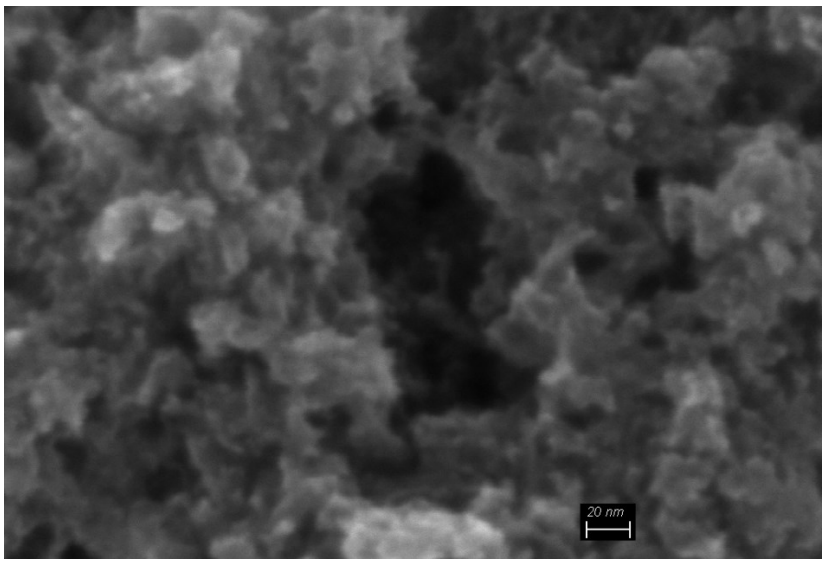

d)

Figure 3-16 a-b shows the spongy morphology of HC-CNS after calcination. Some micrometric compact pieces are visible. A further treatment was carried out with ball-milling to reduce the HC-CNS particle size.

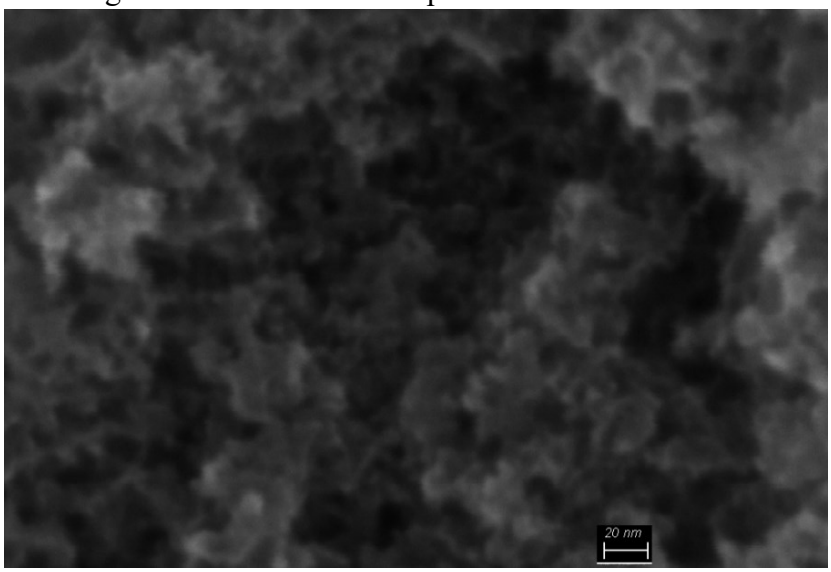

c)

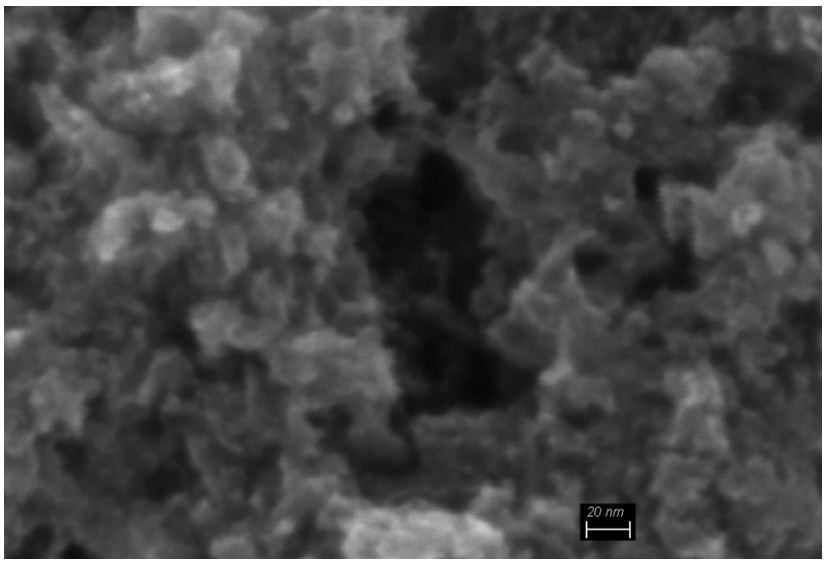

d)

Figure 3-16 c-d show very homogenous structure of the sample after ball-milling.

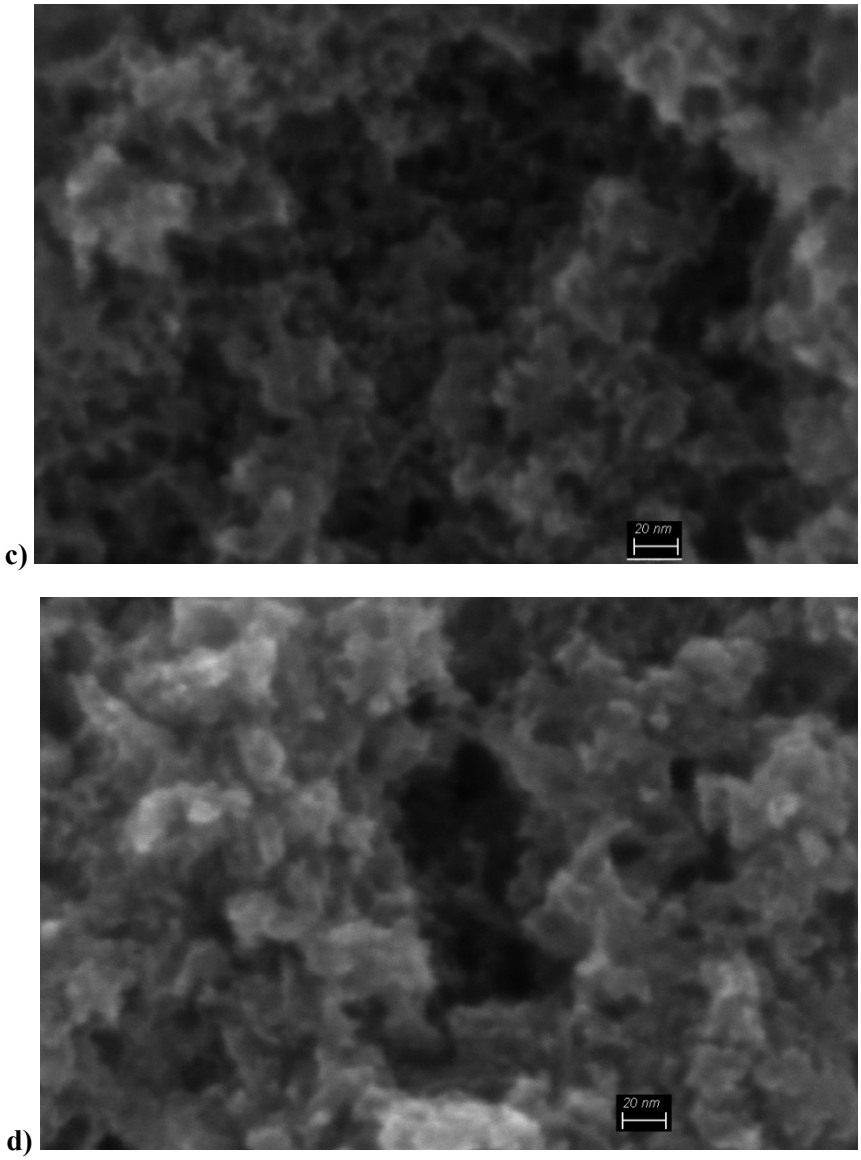

Figure 3-16: FESEM images of HC-CNS

The specific surface area and porosity of HC-CNS were determined by nitrogen adsorption–desorption isotherms at 77K obtained with an automatic adsorption instrument (ASAP 2010, Micromeritics). The samples were degassed at 300°C for 12 h. The profile of nitrogen isotherms is essential for understanding the type of porosity which is present in the sample. Figure 3-17 shows a typical Type IV isotherm (according to the IUPAC classification). The hysteresis loop is related with the presence of mesopores in HC-CNS, sign of capillary condensation.

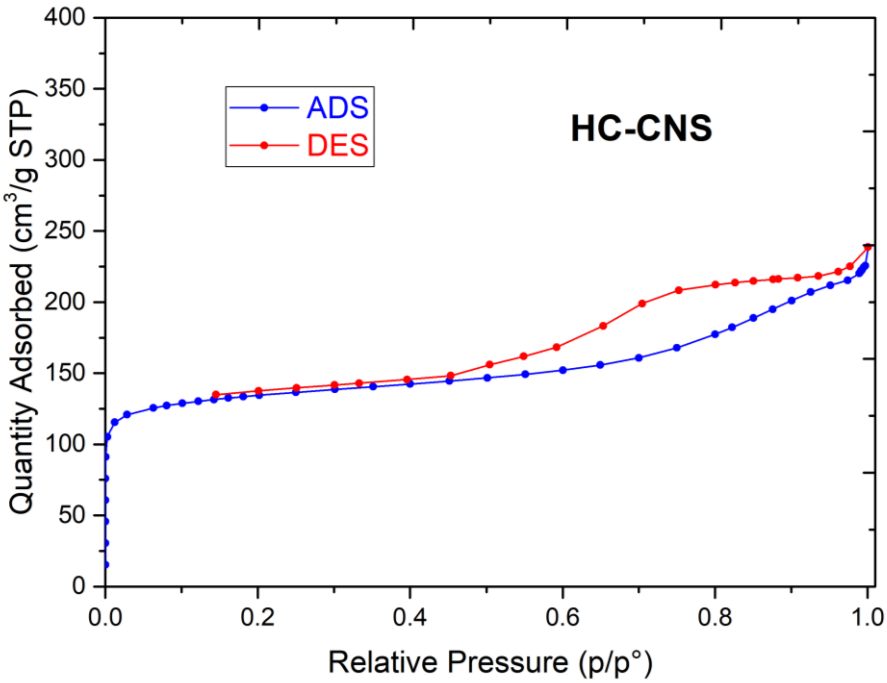

Figure 3-17: Nitrogen adsorption isotherm of hierarchical carbonized nanosponges

HC-CNS has lower specific surface area but higher pore volume. This can be explained by the presence of silica nanoparticles during pyrolysis which creates hierarchical pores with higher total volume of micro-mesopores. The HF treatment was performed after carbonization of SiO_2@NS because HF might destroy or weaken the structure of nanosponges. Moreover, the presence of silica nanoparticles (7 nm) is necessary for mesopores formation and to avoid structure collapse. The total volume of pores in HC-CNS was 0.35 cm^3/g which means it is a carbon with 45% porosity. The application of HC-CNS as conductive matrix for sulfur cathode is reported in chapter 5.

Table 3-6: Specific surface area, cumulative pore volume and pore of HC-CNS

	Specific surface area (m2/g)	Volume of Micropores (cm3/g)	Micropores width (Å)	Volume of Mesopores(cm3/g)	Mesopores width (Å)
HC-CNS	**455**	**0.20**	**30-100**	**0.15**	**5-20**

3.6 Silicon Anode- Embedded in CNS

The semi-conducting nature of silicon nanoparticles requires a conductive matrix to increase the electrical conductivity. In addition, to buffer the volume change of silicon during charge-discharge cycling an amorphous shell is needed. In this section, the process of silicon dispersion during the synthesis of cyclodextrin-based nanosponges is reported as an efficient method to prepare silicon anode. This process can create chemical bonds between silicon particles and cyclodextrin inside

the nanosponges. Among the synthetized nanosponges explained in the previous section, PDMA-NS was selected because of its higher porosity and carbon residue. Different combinations of molar ratios of βCD:PDMA were tested and the molar ratios of 1:4, was found to be optimum in terms of mechanical and electrochemical features.

The embedding process of silicon nanoparticles in nanosponges was conducted by dispersion of SiNPs in dimethyl sulfoxide (DMSO) and sonication for 2 hours then βCD was added to the mixture and sonication was continued for further 30 min. Finally, triethylamine (TEA) and pyromellitic dianhydride (PDMA) were added and leaved to react at room temperature. Once the reaction was complete (gel formation), the obtained solid was broken, ground and washed several times with water. This process ensures the complete removal of unreacted reagents and the purification of the final polymer product. The solid material was finally dried under vacuum overnight, which is generally a sufficient time to achieve an acceptable level of moisture. Figure 3-18 schemes the procedure of incorporation of silicon nanoparticles in the polymeric matrix.

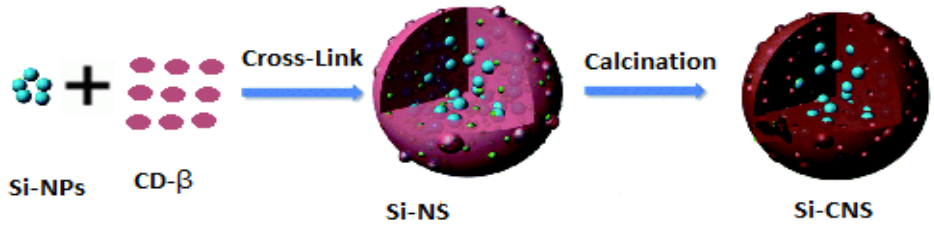

Figure 3-18: Embedding of silicon nanoparticles in nanosponge

3.6.1 Pure Silicon and Silicon with passivate layer

Initially pure silicon was used as active material in the composite. After obtaining promising results of silicon with 3% passivate layer of silica (Si3), the synthesis was repeated for both types of silicon. The pure silicon nanoparticles (SiNPs) formed a yellowish solid while silicon nanoparticles with oxide layer (Si3NPs) formed a brownish gel (Figure 3-19).

a)

b)

Figure 3-19: Gel formation of a) Si@CNS and b) Si3@CNS

The sonication during all steps of the synthesis is essential to guarantee a homogeneous distribution of silicon in the nanosponges bulk. As the nanoparticles are highly reactive in the presence of oxygen, to guarantee a controlled condition for such sensitive nanoparticles, the solvent (DMSO) and catalyst (TEA) were degassed before use. In addition, cyclodextrin was dried in the oven under vacuum. The inert atmosphere was created to avoid oxidation of silicon particles during the experiment. Figure 3-20 shows the experimental setup. The starting time of gel formation, change by the residual content moisture of cyclodextrin. In sufficiently anhydrous batches, after some minutes (less than 5 min) the solution was solidified, while time for others batches reached even 3 hours.

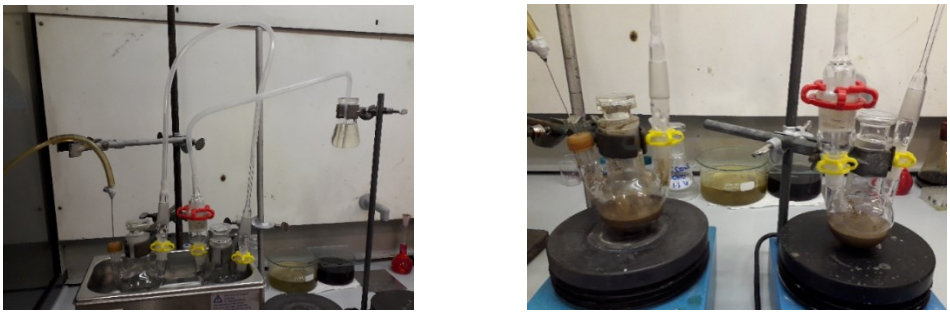

(a) (b)

Figure 3-20: a) Sonication of reagents under Nitrogen flux, b) Gel formation of nanosponges under nitrogen flux with magnet stirring

3.6.2 Silicon percentage in Nanosponge

To increase the electrode specific capacity, three percentages (10%, 20%, 30%) of silicon were used for the synthesis of Si3@NS composite. In the case of 10% and 20% the reaction was successful but in 30% case no gel formation was observed. To explain the effect of silicon mass loading during the synthesis of Si3@ NS, the presence of SiNPs inside the nanosponges can be considered like a filler in a polymeric matrix of a composite. The maximum content of active material in carbonized nanosponges (mass loading) can be attributed to the following main factors:

i) The volume of solvents (DMSO) which affects the sample viscosity
ii) The settings of sonication such as time, frequency and power
iii) The molar ratio between cyclodextrin and PDMA (1:4)
iv) The size of nanoparticles
v) The starting time of gel formation

Our experimental attempts confirmed that 20% is the optimum value, while the polymer was not able to host 30% of guest material and a part of particles was remained in the round-bottom flask. The synthesis improvements and electrochemical characterization of the embedded silicon in nanosponges are discussed in chapter4.

Chapter 4 Innovative Anode Active Material Based on Si Nanoparticles

Silicon with a theoretical capacity almost 10 times that of graphite is a promising anode. Its application is limited because of large volume change and semi-conduction nature of silicon. Electrochemical lithiation/delithiation of silicon and the formation of $\boldsymbol{Li_xSi}$ alloy are reported in chapter2.

Different nanostructured silicon compounds such as nanowire, nanoparticles, core shell, hierarchical structures and porous siliconhave been used as anode materials.[93] There is a strong relation between size of particles and their fracture during lithiation and delithiation. Lui et al demonstrated that 150nm is the particles critical size: below that size cracking does not occur.[94]

Siliconnanoparticles are produced through physical, physicochemical and chemicalmethods. In Pulsed Laser Ablation-PLA, the SiNPs (Si Nano Particles) are prepared by a femtosecond or nanosecond laser pulse irradiating a silicon wafertarget under inert gas atmosphere. The diameter of crystalline SiNPs is proportional to the pressure of inert gas, repetition rate, pulse duration and energy.[95] Knipping et al. used microwave-induced decomposition of Silane (SiH_4) as precursor to synthetize SiNPs with particle size ranging from 6 to 11nm.[96] In chemical methods, generally silicon halides precursors are used to obtain SiNPs. Different reducing agents such as sodium naphthalenide, lithium–aluminum hydride and lithium naphthalenide are applied. In this method, surfactants have essential effect on the size distribution of nanoparticles.[97]

In this work,silicon nanoparticles were purchased from Sigma-Aldrich (nanopowder<100nm particle size (TEM)). Despite all attentions during handling, a native oxide layer forms on the surface of SiNPs that means, the surface of pure SiNPs is surrounded by SiO_2 layer or better, with Si-O bonds. To convert all the Si to the elemental state a reduction step should be added which makes the electrode preparation step more complicated and more expensive from the industrial viewpoint. However, it is reported in the literature that a double layer of carbon and SiO_2 improves the electronic conductivity, enhances the adhesion of the carbon to the Si core and alleviates the effects of the volumetric changes during cycling.[98]

4.1 Experimental Set-up

In this chapter, the results of various experimental investigations on the silicon nanoparticles as anode material for post-lithium ion batteries are reported. Two main strategies are discussed:

-Wrapping SiNPs in graphene

-Embedding SiNPs in cyclodextrin-based nanosponges

4.1.1 Electrode preparation

To evaluate the electrochemical properties of the anode material, the electrodes were prepared by slurry casting on a copper foil. The slurry composition is 70% silicon active material, 20% carbon black (TIMICAL SUPER *C45* Conductive Carbon Black*)* and 10% poly vinylidene fluoride (PVdF, Solvay Solef 6020) as binder. All dry powders are mixed in a mortar and introduced in a Becher, then N-methyl-2-pyrrolidone (NMP, Aldrich) is added. The volume of NMP depends on the required viscosity. Normally to obtain a slurry with applicable viscosity, 500µl solvent used for each 100mg of total powder. The cleaning of copper foil before casting is performed to remove eventual contaminations. The suspension is casted a copper foil using a film applicator together with doctor blade. Two types of blade were used to fabricate the electrodes; a blade with two screws to adjust the distance from the foil and a four sides blade with fixed distance that guarantees precise thickness of casting. Figure 4-1 shows the film applicator and adjustable doctor blade respectively. After evaporating the solvent under the hood, some disks with 15mmΦ(coin cell)and 18mmΦ for use in EL-CELL were punched and subsequently dried in 100ºC under vacuum for about 4 hours.

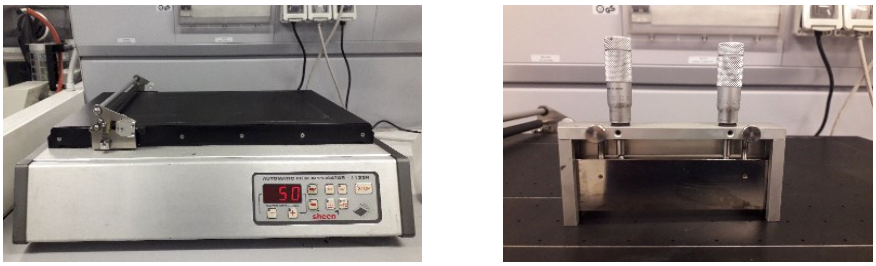

(a) (b)

Figure 4-1: a)Film applicator, b) Adjustable blade

The dried disks were transferred in Ar-filled glove-box to assemble the cells. The weight of the coated material on the disks were calculated by subtraction the average weight of the copper foil from the total weight of eachdisk. The anode electrodes are used in EL-CELL or coin cell with lithium metal (pure lithium foils, Rockwood) as the counter electrode. A glass-fiber (Whatman GF/A) discs with 250µm thickness soaked by the electrolyte is used as the separator. Figure 4-2 shows the EL-CELL and coin cell components.

4.1.2 Cell assembling

The EL-CELLs are assembled in the glove-box as follows. At first a 18mmΦ lithium disk is cut from the foil and put in the bottom of the cell, then a peek sleeve is pushed inside the cell. The separator is inserted in the peek sleeve and the electrolyte was added dropwise. The anode disk is the last component which is added to the cell. Finally, the upper stainless-steel part and spring as electric

contacts are inserted. The standard liquid electrolytes 1M LiPF6 + EC:DMC (v:v) is used for the electrochemical testing.

(a) (b)

Figure 4-2: a) EL-CELL, b) coin cell

The coin cells were assembled with 15mm diameter anode disks in the glove-box and crimped in the dry-room. The sequence of the coin cell assembling is similar to the EL-CELL. To guarantee stable electric contact, one spring and two spacers in both sides were used (Figure 4-2).

4.1.3 Electrochemical Tests

Galvanostatic cycling tests applied by constant current is applied. The cell voltage (versus the lithium metal as counter electrode) is measured as a function of time. The range of potential is selected between 0.01-2 V. The amount of the charge passed during complete charge or discharge is registered for calculation of the specific capacity. The current density was calculated based on the mass of the silicon active material.

4.2 Graphene preparation

As previously explained graphene has an outstanding importance in our investigation so it has been prepared on purpose. Silicon nanoparticles were purchased from Sigma-Aldrich. Graphene oxide was prepared in our laboratory by oxidation of graphite. Here the synthesis of graphene oxide is reported.

Graphene oxide was produced by means of chemical exfoliation of oxidized graphite according to the modified Hummers and Staudenmaier's method. A suspension of 500 mg of graphite in H_2SO_4, H_3PO_4, and $KMnO_4$ (82 mL, 10 mL, and 8.34 g, respectively) was prepared and left under magnetic stirring for 3 days (Figure 4-3). The viscous resultant suspension was cooled in ice bath and the non-reacted MnO_4^- was titrated with H_2O_2 (30%).

a) b)

Figure 4-3: a) Mixing, b) Dialysis

The brownish graphite oxide was separated by centrifugation (4000 rpm) after being washed with 1M HCl then with water for three times. During the washing procedure, graphite oxide underwent exfoliation and a viscous brown suspension of GO was produced. The obtained GO suspensions were purified by dialysis against water with Dialysis Sacks Sigma (molecular weight (MW) cut off 12000 Da) until the pH value reaches 4 (Figure 4-3). To estimate the content of graphene oxide in the sample, 1 mL of GO suspension was weighed and dried in air then weighed. The dried material was around 40 mg.

A series of reduction methods and their effective performance are presented in Table 4-1. The capacities are calculated based on the mass of reduced graphene oxide.

Table 4-1: Result of different strategies for reduction of Graphene Oxide. The specific capacity was considered after at least 50 cycles.

	Reduction Method	Current Density	Specific Capacity	Ref
1	Thermal reduction	0.17 mA/g	2000mAh/g	[99]
2	L-ascorbic acid & Thermal	0.1 mA/g	1640mA/g	[100]
3	Magnesiothermic reduction	1.2 mA/g	1610 mAh/g	[101]
4	Thermal reduction	0.2 mA/g	1200 mAh/g	[102]
5	Magnesiothermic reduction	0.2 mA/g	1100 mAh/g	[103]
6	Hydrazine	0.5 mAh/g	1600 mAh/g	[104]
7	Thermal reduction	0.1 mA/g	1100 mAh/g	[105]
8	Thermal reduction	0.5 mA/g	1000 mAh/g	[106]
9	Thermal reduction	1.2 mA/g	1200 mAh/g	[107]
10	Thermal reduction	2.5 mA/g	1200 mAh/g	[108]

The reduction of GOwas carried out by thermal reduction in Ar (97%)/H_2(3%) atmosphere. The reduction was performed in tubular oven at 700ºC for 2 hours with a temperature ramp of 10ºC/min. Figure 4-4 shows image FESEM of reduced graphene oxide.

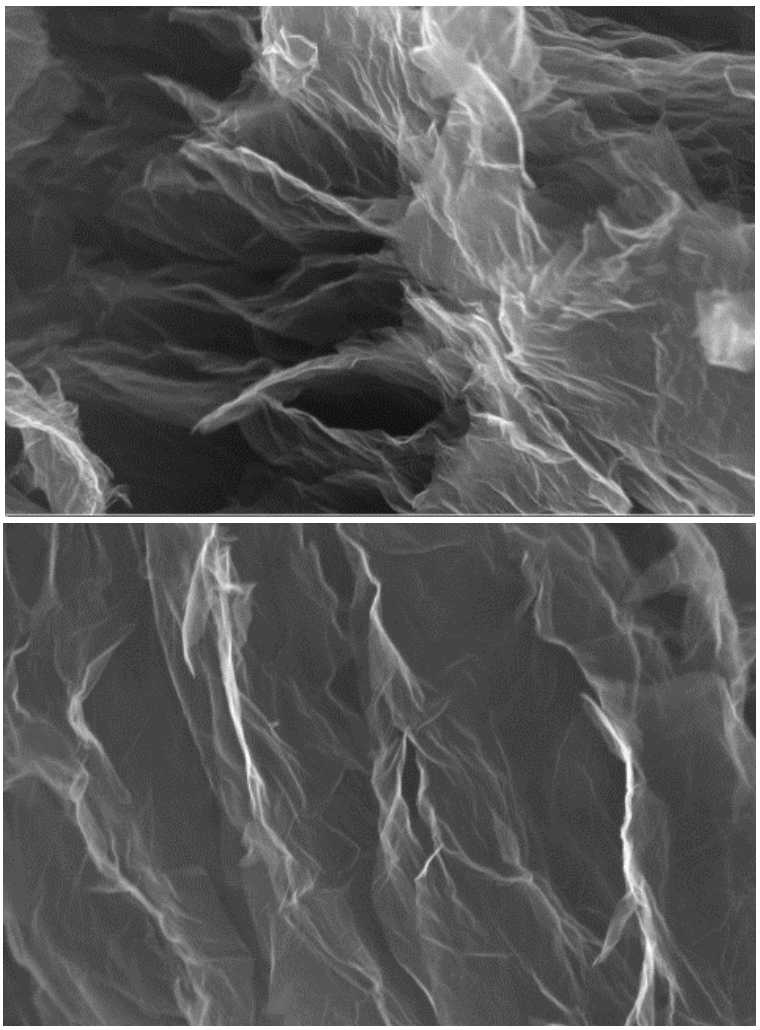

Figure 4-4: FESEM image of reduced graphene oxide-rGO

4.3 Silicon wrapped in Graphene

4.3.1 Bare Silicon-SiNPs

This first sample was prepared and studied to get information on the electrochemical behavior of bare SiNPs for sake of comparison with SiNPs embedded in carbonous matrix. Bare silicon nanoparticles were used to prepare slurry. 70 mg SiNPs powder was mixed with 20 mg carbon black (C45) and 10 mg PVDF binder. The mixture was poured in a Becher, then 500 µL NMP were added. The resultant mixture was magnetically stirred for 4 hours. Since the active material was pure silicon, the final percentage of silicon in the electrode was considered 70%. Figure 4-5 shows the galvanostatic cycling of SiNPs vs lithium. As expected, very low specific capacity was observed at first cycle with current density of 0.1C and 1C at successive cycles. Indeed, this low capacity confirms that SiNPsdo not participate electrochemical reactions. The delivered capacity around 60 mAh/g could be attributed to the presence of the carbon black which is 20% of total weight of electrode.

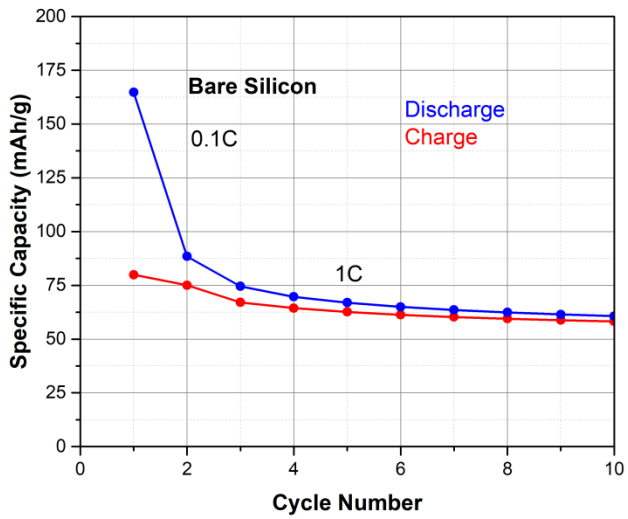

a)

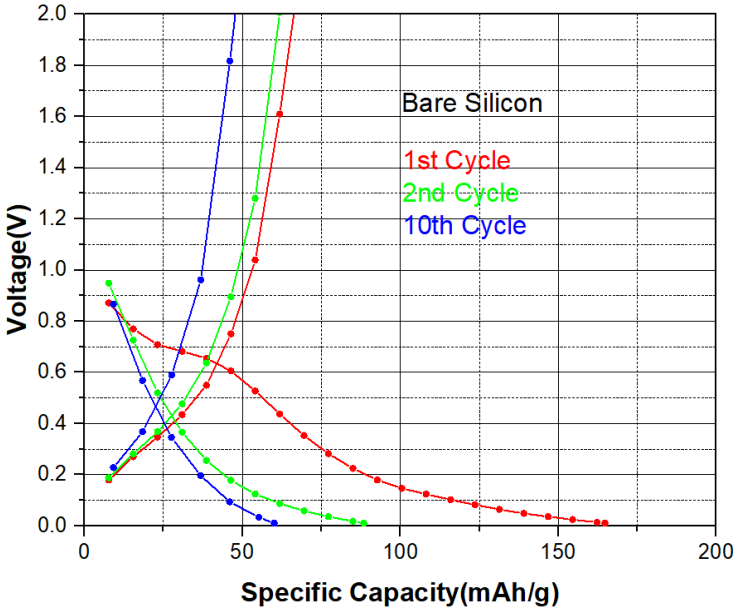

b)

Figure 4-5: a)Galvanostatic cycling, b) Charge and discharge capacity of Bare silicon

Even at the first lithiation, the activity of Si appears very limited with respect to the theoretical value. The subsequent delithiation is even more limited. The following cycles indicate that the electrochemical activity is related just to the presence of the carbon black in the slurry.

In addition, the voltage profile for the first lithiation suggests that Li^+ have reacted irreversibly with SiO_2 to form silicon compounds.[109]According to the reaction of lithiation of SiO_2 at voltage 0.8V Figure 4-5.b.

i) $\mathbf{4Li^+ + 4e^- + 5SiO_2 \rightarrow 2Li_2Si_2O_5 + Si}$

ii) $\mathbf{4Li^+ + 4e^- + 3SiO_2 \rightarrow 2Li_2Si_2O_3 + 2Si}$

iii) $\mathbf{4Li^+ + 4e^- + 2SiO_2 \rightarrow 2Li_2Si_2O_{54} + Si}$

iv) $\mathbf{4Li^+ + 4e^- + SiO_2 \rightarrow 2Li_2O + Si}$

In the following step Li^+ reacts reversibly with the Si core to giving rise to a reversible lithiation.[110]

$$\mathbf{15\ Li^+ + 15\ e^- + 4Si \rightarrow\ Li_{15}Si_4}$$

The irreversible, lithium silicon compounds formation is no more present in the subsequent lithiations. Moreover, the low capacity at the following lithiation suggests that all the available active materials, have completely reacted at the first lithiation. The obtained results put well in evidence that SiNPs are not sufficiently connected to conductive network. Moreover, the presence of SiO_2 without any carbonaceous matrix did not show any positive effect.

4.3.2 Silicon-rGO Composite

To create a conductive support for silicon nanoparticles, a silicon-graphene system was prepared. However, the dispersion of SiNPs for interaction with graphene oxide was the first facedproblem. It was observed that a stable dispersion of SiNPs in water even with high energy sonication, was impossible to obtain. For this reason, CTAB (cationic surfactant) was used in order to disperse nanoparticles in water.

The silicon nanoparticles are dispersed in a equivolume mixture of ethanol/ water. It is expected that basic pH of solution is able to modify the surface of nanoparticles and the hydroxyl groups make the surface negatively charged. After the addition of CTAB, the positive head of surfactant starts to interact with the negative charges on the surface of the nanoparticles and form micelles.

Initially 300 mg SiNPs were sonicated in 200ml of ethanol/ water mixture, then 10 mg CTAB were added to sample and sonicated for 2h. Separately 200 mg of reduced graphene oxide were dispersed in 50 ml ethanol/ water mixture and left under sonication for 2h. Finally, the two dispersions were mixed in a Becher and sonication was continued for another 4h. After 3 days the sample was deposited and the transparent supernatant was drained. The Si-rGO sample was collected, dried and weighed for the slurry preparation. The percentage of silicon in the final slurry was about 60%.

FESEM image of Figure 4-6 shows that an agglomerated mass of SiNPs is formed between graphene sheets. These silicon agglomerations have not any contribution in electrochemical reactions due to lack of contact with conductive

matrix. Moreover, this inhomogeneity in active material lowers the efficiency of the material and affects the reproducibility of the results.

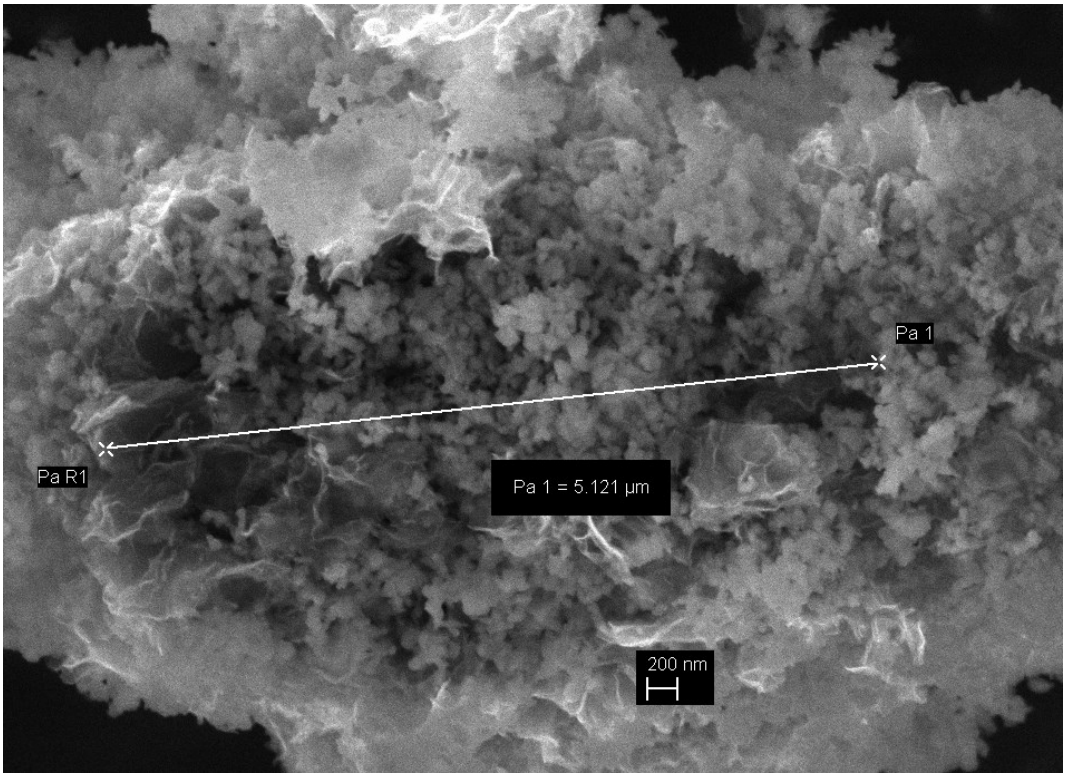

Figure 4-6:FESEM images of agglomerated silicon nanoparticles between graphene sheets

Lithium-Silicon half-cells were assembled with Whatman fiber glass separator was soaked in lithium-ion standard electrolyte (LP30). Galvanostatic cycling was performed at current density 0.1C.

Figure 4-7depicts the cycling performance of the Si-rGO anode. The specific capacity of the sample prepared with CTAB surfactant was around 550 mAh/g after 25 cycles. This low specific capacity can be explained by the agglomeration of silicon nanoparticles among rGO sheets.

Figure 4-7.a shows the low initial coulombic efficiency of Si-rGO. This means that the total charge inserted into the electrode during lithiationis higher than the charge extracted during delithiation. This behavior is due to the irreversible formation of the Li_4SiO_2 alloy. As can be seen in Figure 4-7.b the profile of the cell is similar to that of bare SiNPs but the specific capacity is markedly higher suggesting the beneficial effect of graphene. Beyond the positive effect of SiO_2, this could be related to crystalline- amorphous transition of silicon nanoparticles.[98] The rate of capacity loss is progressively reduced and after 50 cycles reaches 500 mAh/g.

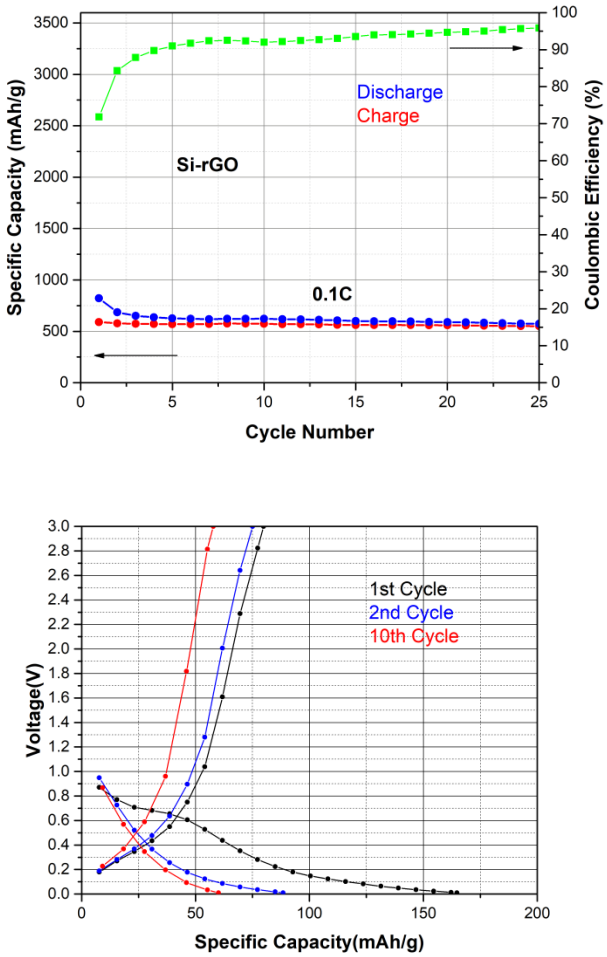

Figure 4-7: a) Galvanostatic cycling, b) Charge and discharge capacity of Si-rGO

Figure 4-8 shows the thermogravimetric analysis (TGA) in air flux which was performed to determine the percentage of Silicon nanoparticles. The mass loss was around 40% which well agrees with the initial percentage of SiNPs (60%). The last increase of mass above 520°C is related to the oxidation of SiNPs.

4.3.3 Silicon Nanoparticles in 3D-rGO (Si-rGO-PAM)

During the preparation of Si-rGO, centrifugation method was used for separation of sample from supernatant. It is supposed that this step is responsible for the graphene sheets collapse and agglomeration of SiNPs. In order to solve this problem, a three-dimensional conductive structure (scaffold) was introduced into the composite structure by the use of a polymer acting as a cross-linker among rGO flaks. Different polymers were tested. Finally, it was found that Polyacrylamide (PAM) provides the best performance. The application of used polyacrylamide as cross-linker was reported by Lin et al.[101] 300 mg of SiNPs after being exposed in

air for 24h(to form silicon oxide) were dispersed in 100 ml of water and sonicated for 2 h. Subsequently 10 mg CTAB (Hexadecyltrimethylammonium bromide) were dissolved in 100 ml of water added to the dispersion and left for other 2h. The sonication was stopped and the sample was left for a whole night. The day after 50ml of GO(4 mg/ml) was added to obtain the final ratio of SiNPs:GO (3:2). Polyacrylamide solution(PAM1%)was added drop by drop in the above suspension to start a cross-linking reaction until the flocculate appeared and the solution became clear and transparent. Then the sample was centrifuged at 200 rpm and finally was filtered without vacuum condition. To avoid graphene flakes collapsing, water was removed by freeze-drying method. A low density dried sample was collected and treated by annealing at 700 ºC in H2/Ar atmosphere for 2 h.

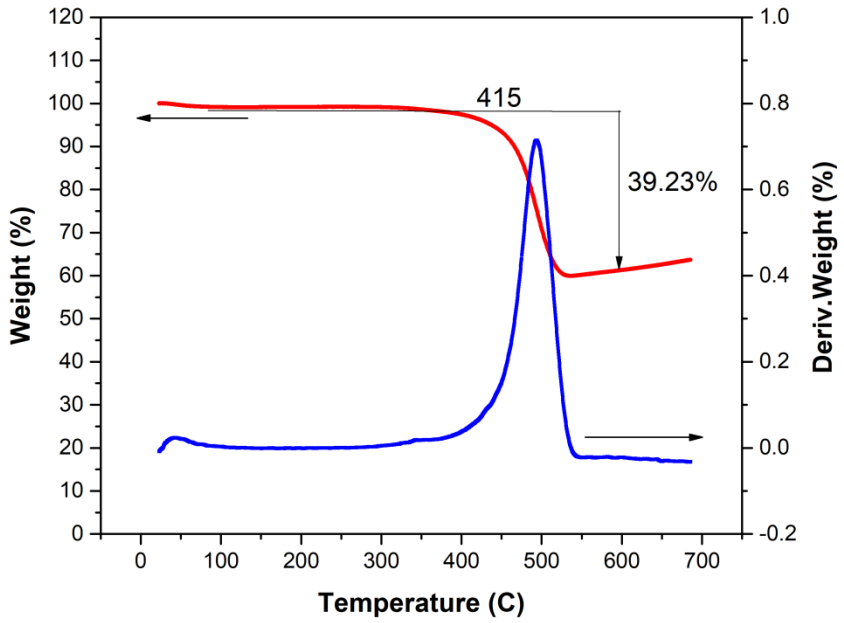

Figure 4-8: TGA analysis of silicon nanoparticles in Si-3D-rGO

FESEM images in Figure 4-9, show a three-dimensional structure created by the polymer scaffold. The SiNPs are distributed homogeneously in the rGO network. In the Figure 4-9.a, a spongy structure with some channels is recognizable. Figure 4-9.b(higher magnitude)demonstrate graphene sheets wrap silicon nanoparticles. No sign of aggregation between nanoparticles and graphene sheets was observed. The graphene flakes are oriented in different direction without any evidence of collapse.

a)

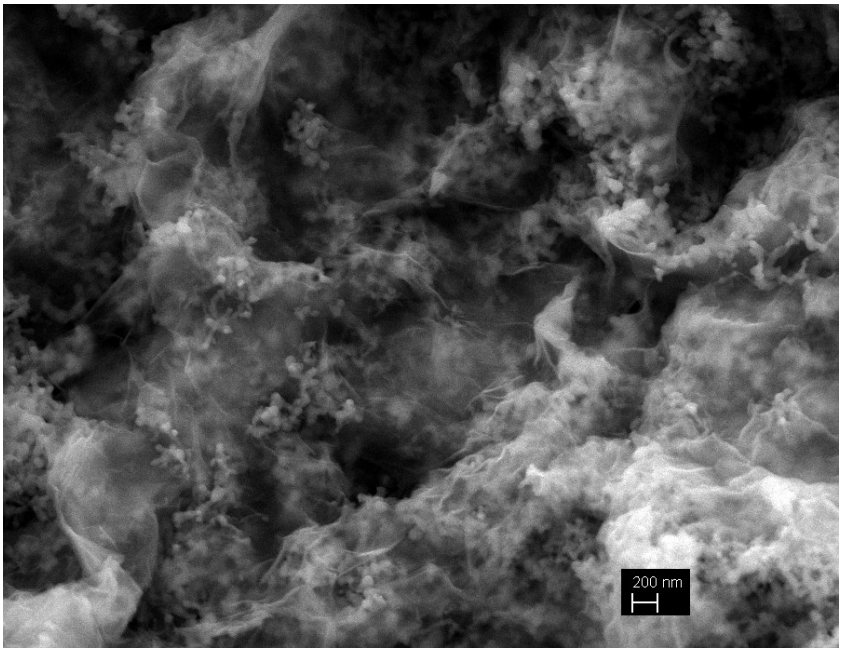

b)

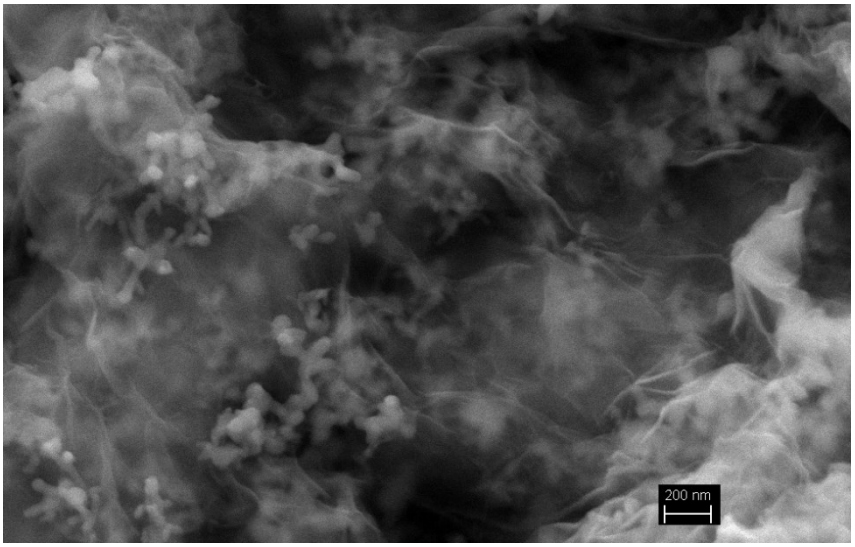

Figure 4-9: FESEM images of silicon nanoparticles in 3D-graphene (Si-3D-rGO)

The distribution of the elements on the surface of the sample was studied by Energy Dispersive X-ray Analysis (EDX). The percentage of silicon on the sample surface is around 52% which is reasonably in a good agreement with the ratio obtained by TGA method (Figure 4-10).

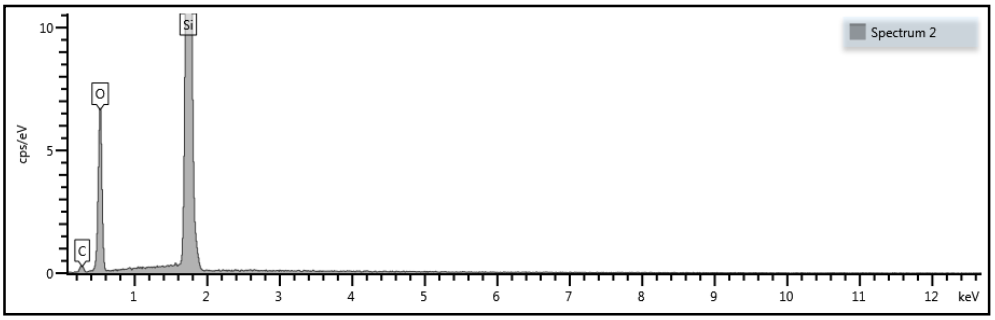

Element	C	O	Si	Total
Wt%	7.65	40.04	52.31	100.00

Figure 4-10: EDX analysis of silicon nanoparticles in 3D-graphene (Si-3D-rGO)

The electrode was prepared by dissolution of 70 mg (70%) of Si-3D-rGO as active material, 20mg (20%) carbon black and 10 mg (10%) PVDF as binder in NMP. The slurry was casted with film applicator at 200µm thickness. The final percentage of silicon was calculated by 42% based on precise result obtained by TGA.

Figure 4-11.a shows the galvanostatic cycling which was performed for a half-cell assembled in Argon filled glove-box. The specific capacity of silicon is improved which can be attributed to the homogenous distribution of SiNPs among the graphene sheets (as shown in Figure 4-9).

The initial irreversible capacity can be attributed to SEI (Solid Electrolyte Interphase) formation. The large difference between capacity of first and second cycle is due to the crystalline-amorphous transformation. The capacity of the cell starts to increase after ten cycles and reaches about 1000 mAh/g.

The initial irreversible capacity is to be attributed to the formation of a SEI-like layer. The large difference between the capacity of the first and second cycle is due to different current values and the Silicon-Lithium compounds formation. The capacity of the cell starts to increase slightly after ten cycles and reaches about 1000 mAh/g. Analysis of the curves ofFigure 4-11.b shows that lithiation is always more extended than delithiation but in the following cycles this difference decreases.

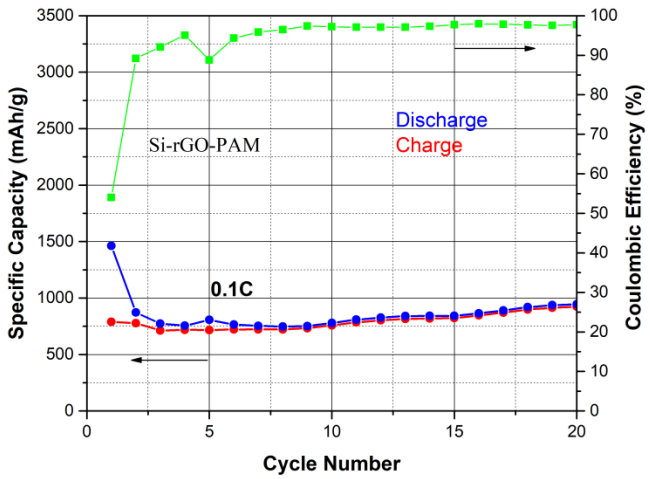

a)

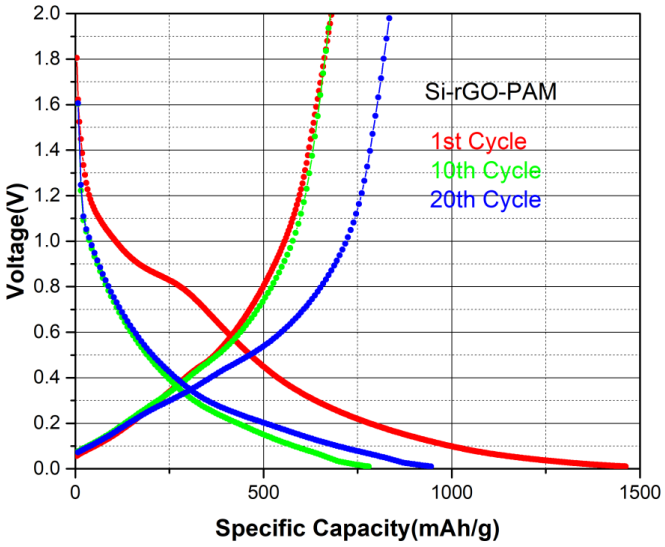

b)

Figure 4-11: a)Galvanostatic cycling and Coulombic efficiencies, b) Charge and discharge capacity of silicon nanoparticles in 3D-graphene (Si-3D-rGO)

4.3.4 Si3-rGO-PAM-Passivate silicon nanoparticles

A possible drawback of the spontaneous forming of the SiO_2layer is uncontrolled growth-up with different thickness. To overcome this problem and guarantee a constant thickness of the silica layer, a silicon nanoparticle with a passive oxide layer of 3% in weight (Sigma-Aldrich nanopowder, <100 nm (BET), <3% oxygen passivation) was investigated.

The presence of the passive oxide layer on the silicon surface can protect SiNPs from further reaction with the electrolyte. The silica insulating layer creates a low reversible specific capacity and increases the interfacial charge transfer impedance.[111] Despite such increase in cell resistivity, a thin silica layer improves the electrochemical performance of the Si-based anode.

These passivate silicon nanoparticles were used to prepare Si3-rGO-PAM. For the sample preparation the same procedure of Si-rGO-PAM was applied. The slurry was prepared with a weight ratio of 70:20:10. Figure 4-12shows TGA analysis of the sample. The percentage of silicon in final electrode was around 53%. This reduced mass loading can be related to the difficulty of interaction between Si-O groups on the surface of Si3 and carbonyl / carboxyl groups of graphene oxide.

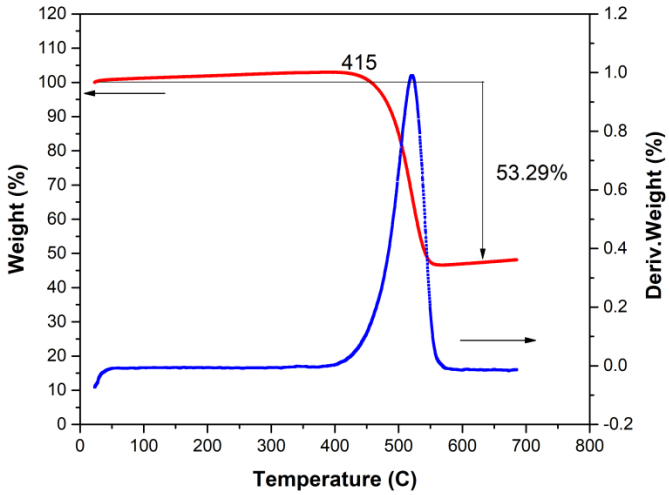

Figure 4-12: TGA analysis of passivated silicon nanoparticles in 3D-graphene (Si3-3D-rGO)

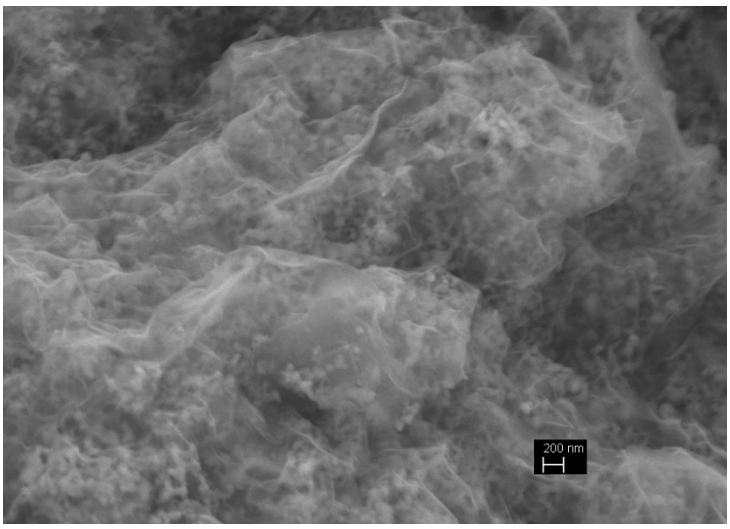

Figure 4-13:FESEM images of passivated silicon nanoparticles in 3D-graphene Si3-3D-rGO

To evaluate the electrochemical performance of Si3-rGO-3D, the cells were assembled with the same method followed for Si-rGO-3D.

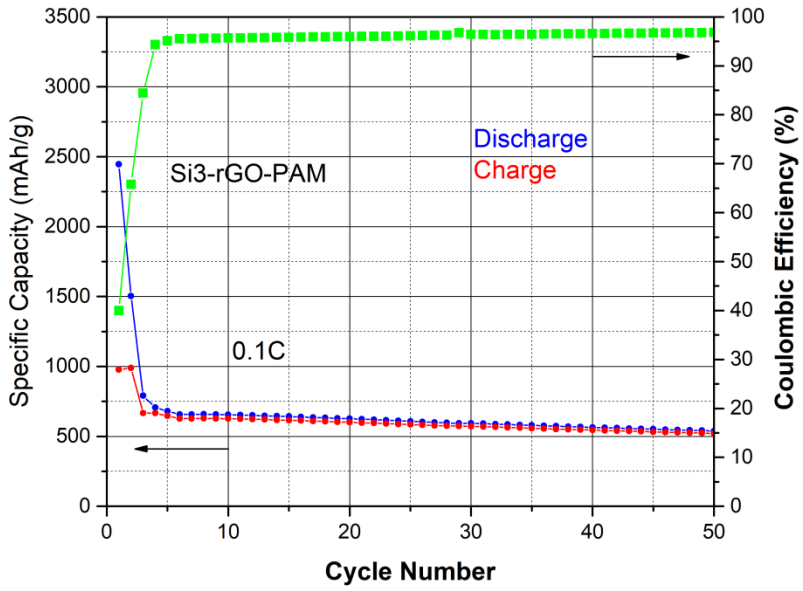

a)

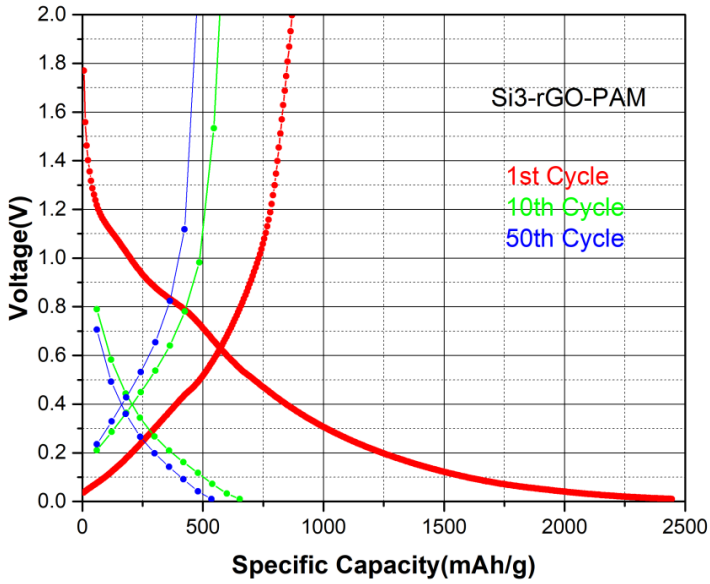

b)

Figure 4-14: a)Galvanostatic cycling and Coulombic efficiencies,b)Charge and discharge capacity of passivated silicon nanoparticles in 3D-graphene (Si3-3D-rGO)

Figure 4-14.a shows galvanostaic cycling of Si3-rGO-3D. The initial capacity fade was observed also in this case. In the following cycles the capacity remained stable with high coulombic efficiency. Figure 4-14.b compares the capacity profile among the 1st, 10th and 50th cycles. After the first cycle capacity fade, the trend in charge/discharge capacity is stable. The presence of the silicon oxide layer seems to effectively improves the coulombic efficiency. Moreover, the homogeneous distribution of Si3NPs in combination with the three-dimensional graphene structure has synergic effect on the both specific capacity and coulumbic efficiency.

Although graphene makes a conductive network that facilitates the electron conduction, it doesn't provide protective layer on the Si3NPs because of its low physical interactions with silicon. This weak interaction between Si3NPs and graphene can be associated to their chemical structure; the graphene sheets can cover homogenously the nanoparticles, but they cannot form stable links with the silicon nanoparticles. It means that a chemical interaction is needed to create intimate and strong contact between the compounds.

4.4 Embedded silicon nanoparticles in CD-NS

The silicon nanoparticles embedded in cyclodextrin-based nanosponges (discussed in chapter3) are used as anode active materials. In order to obtain conductive electrode, different carbonization methods were tried. The optimum combination of operative parameters such as maximum temperature, time of heating, heating ramp and inert gas flux were selected based on the optimized porosity and surface area.[91]

4.4.1 Carbonization of Si@ NS

The samples before calcination were grinded, washed and dried at room temperature to optimize the exposure to the inert gas and uniform heating. The grinded Si@NS was heated up to 800°C and rest for 2 hours at this temperature. The heating ramp and nitrogen flux were 10°C/min and 100 ml/min respectively. The furnace was cooled naturally and the composite was maintained under nitrogen flux until the ambient temperature. The sample grinding grade was an important factor to obtain a homogenous carbonized sample.

a) 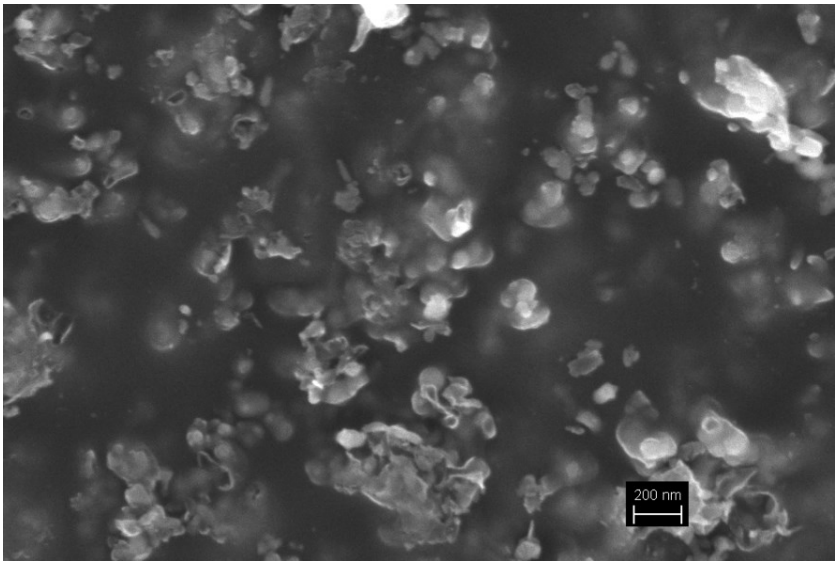

b) 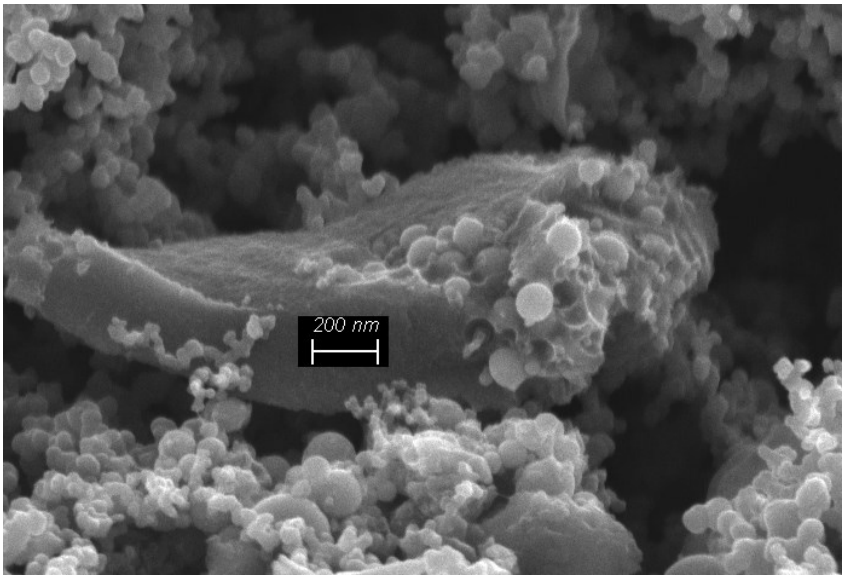

Figure 4-15: FESEM images of passivated silicon nanoparticles embedded in carbonized nanosponges (Si3@CNS)

Figure 4-15.a shows FESEM images of the Si3@CNS with micrometric dimensions while in the Figure 4-15.b a cross section image of these silicon particles embedded in CNS can be seen. The silicon nanoparticles with dimensions less than 100nm can be distinguished in the carbonaceous matrix. Since the nanoparticles are buried in carbonaceous bulk, they are not accessible to the electrolyte. This means, lithium ion cannot reach the particles inside the core of CNS. A strong mechanical force is required to make all or most of the particles free from the carbon bulk. Moreover, the heat treatment process induces sintering to the material and causes the formation of agglomeration, hence, it is necessary to repeat sample grinding after calcination.

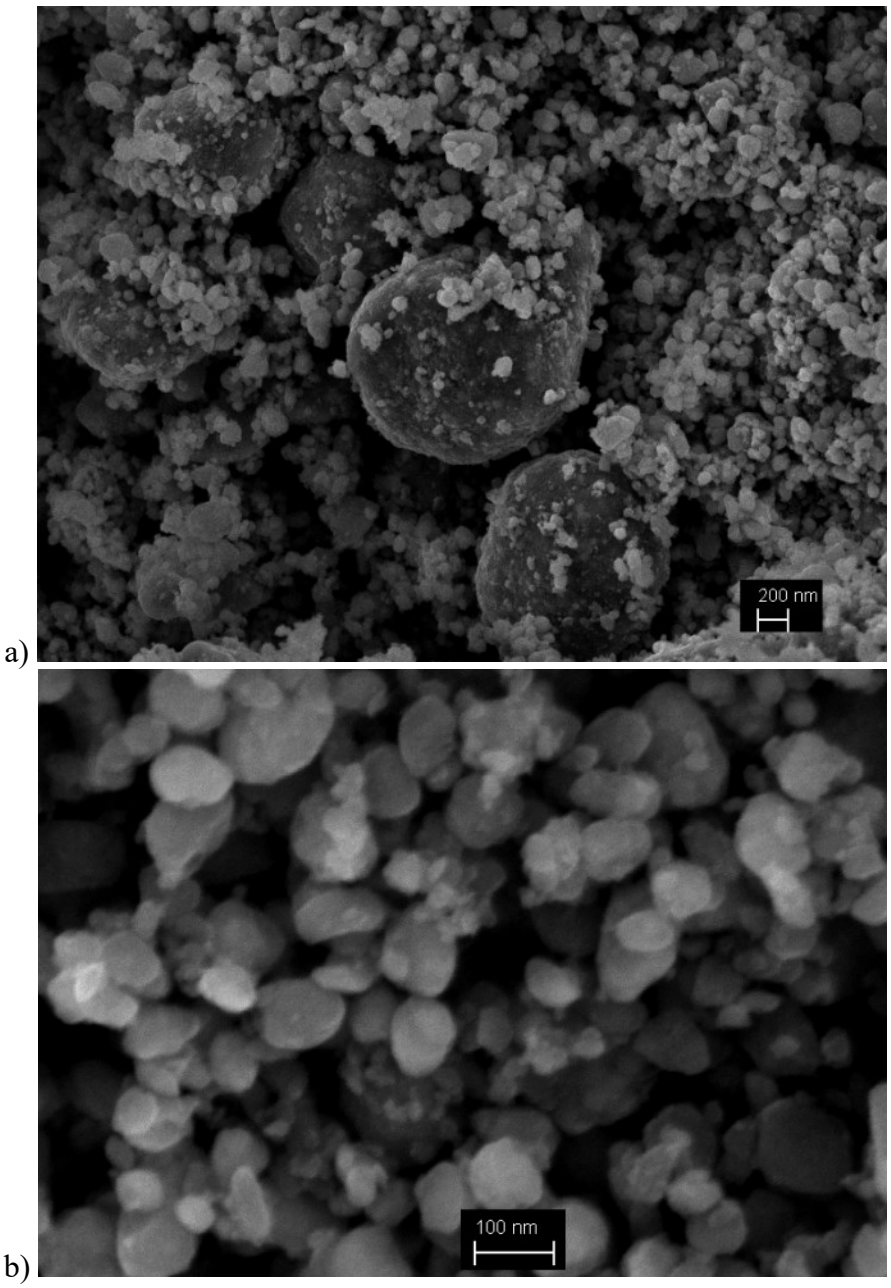

Figure 4-16: FESEM images of Si3@CNS a) before, b) after ball milling

Figure 4-16 shows FESEM images of Si3@CNS before and after ball milling, the most part of silicon nanoparticles are expelled from the carbon bulk. Moreover, nanoparticles without any metallization are well recognizable in this image. It means that on the surface of the spheres expelled from carbon bulk, a very thin conductive layer formed which is visible with electron microscopy.

4.4.2 Optimization of Silicon mass loading

To design an electrode material with a high specific capacity and conductivity, it is needed to optimize the ratio between the silicon content(as active material provides capacity) and the carbonaceous matrix (CNS) which creates a conductive network. The percentage of silicon in the composite material is a determinant factor for the anode performance.

The preparation of Si@CNS/Si3@CNS samples was carried out for the samples with 10 and 20% silicon. Initially Si:βCD samples with a weight ratio equal to 1:9 (10% Si) were synthesized and then calcinated. Figure 4-17-a shows the thermal degradation of Si@CNS in air fluxup to 800°C. The degradation starts at 300ºC and occurs in one step with the inorganic residue measured around 19%.

The synthesis was repeated for the sample with Si:βCD weight ratio equal to 2:8 (20% Si) and subsequently was calcinated. Figure 4-17.b, shows the thermal degradation of Si@CNS which was carried out in air flux up to 800°C. The first step occurs at lower temperature, between 220 and 350°C, with a 30% of weight loss. The second step goes from 350to 600°C showing other 27% of weight loss. The overall weight loss was around 57% that means the silicon percentage after calcination raised to 43%.

These different behaviors in thermal degradations, reveal two different kinds of host–guest interactions in the composite. These results show good approximation for both pure silicon and silicon with passivate oxide layer.

Despite the sample with 19% silicon provides high specific capacity, it was not an ideal candidate as silicon anode material because the lithiation/delithiation of silicon was shielded by carbon. A similar behavior was observed when the composition of slurry was 50:40:10 instead of 70:20:10. The increase in the percentage of carbon black or CNS is supposed to be an important factor to improve the conductivity of electrode and specific capacity. However, the apparently high specific capacity is associated to low quantity of active material.

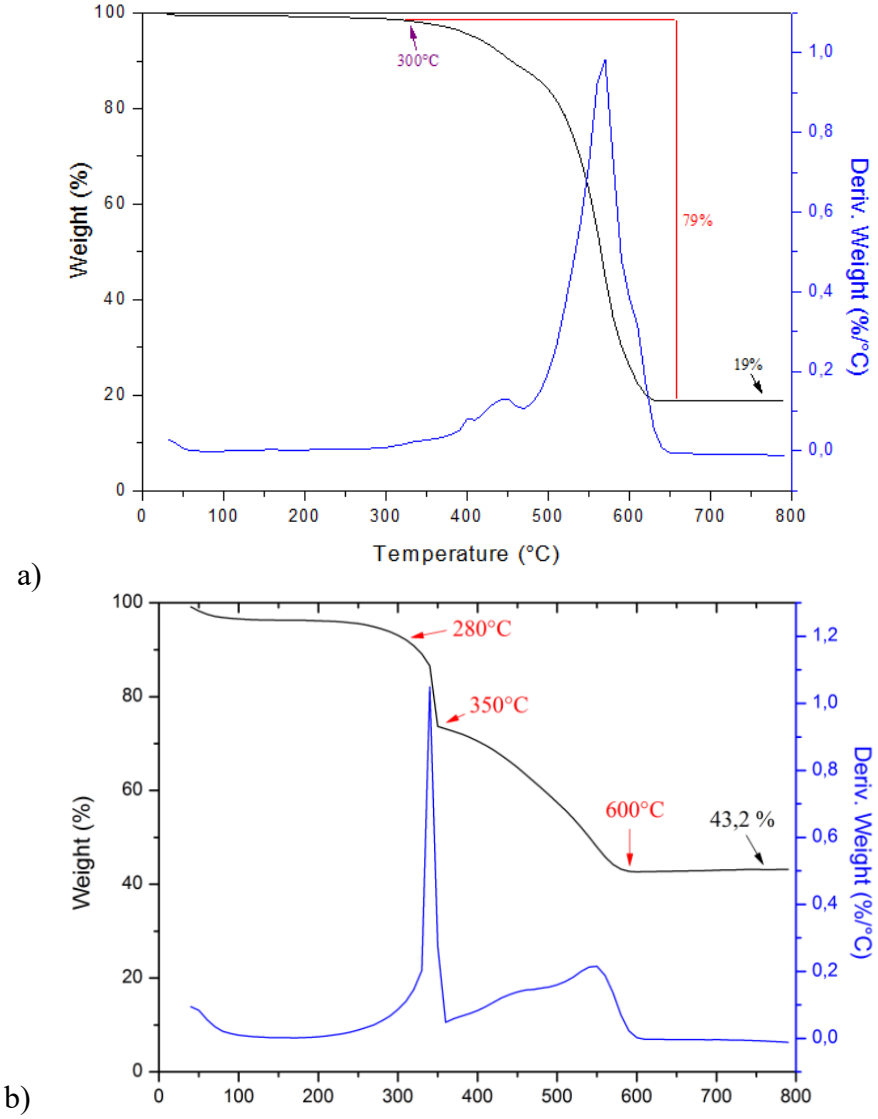

Figure 4-17: TGA analysis of silicon nanoparticles embedded in nanosponge with initial silicon a) 10%, b) 20%

The specific surface area and porosity of Si3@CNS were determined by the ASAP 2010 volumetric analyzer. Figure 4-18 illustrates the shape of the nitrogen isotherm which coincides with the typical Type I isotherm according to the IUPAC classification. At low relative pressure it can be seen a steeply increase which indicates adsorption or condensation of nitrogen in micropores. The constant amount of adsorbed nitrogen with no sign of capillary condensation, confirms the absence of mesopores. The Langmuir equation was applied to calculate the specific surface area of the carbon. The Density Functional Theory (DFT) method was applied to evaluate the micropores volume and the pore size distribution. The Cumulative pores volume and pores size in Si3@CNS are remained almost the same as CNS. The reduction in specific surface area from 560 to 431 m^2/g is associated to the presence of silicon nanoparticles in CNS structure. A comparison between the physical properties of Si3@CNS and PMDA-CNS is reported in Table 4-2.

Table 4-2: Specific surface area, cumulative pore volume and pore of Si3@CNS

Sample	Surface Area m^2/g	Cumulative pore Volume cm^3/g	Pore width Å
PMDA- CNS	560	0.11	5-16
Si3@CNS	431	0.11	5-18

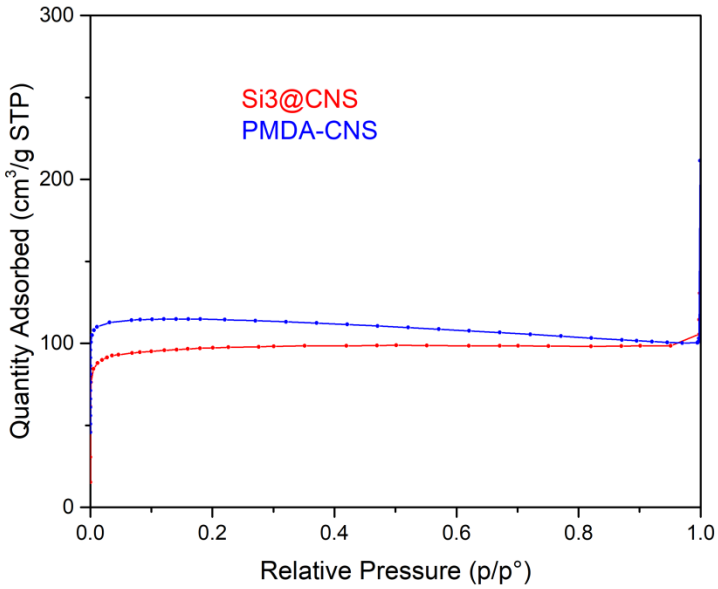

Figure 4-18: Nitrogen adsorption isotherm of the Si3@CNS at 77K and PMDA-CNS

To evaluate the role of carbonized nanosponges, both Si@CNS and Si3@CNS were used to prepare slurry with a ratio 70:20:10 with the method already used for the previous samples. The EL-CELL were assembled by 18 mm disks of electrode with the use of Whatman separator and LP30 as electrolyte. In these cells metallic lithium was used as counter electrode. The galvanostatic cycling was performed at different current regimes.

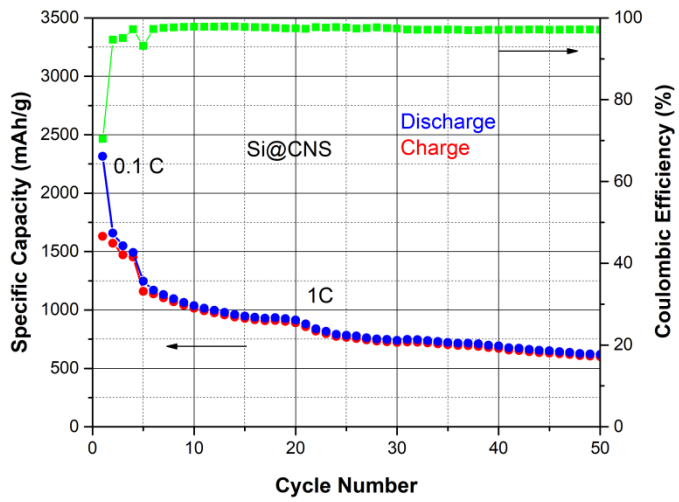

a)

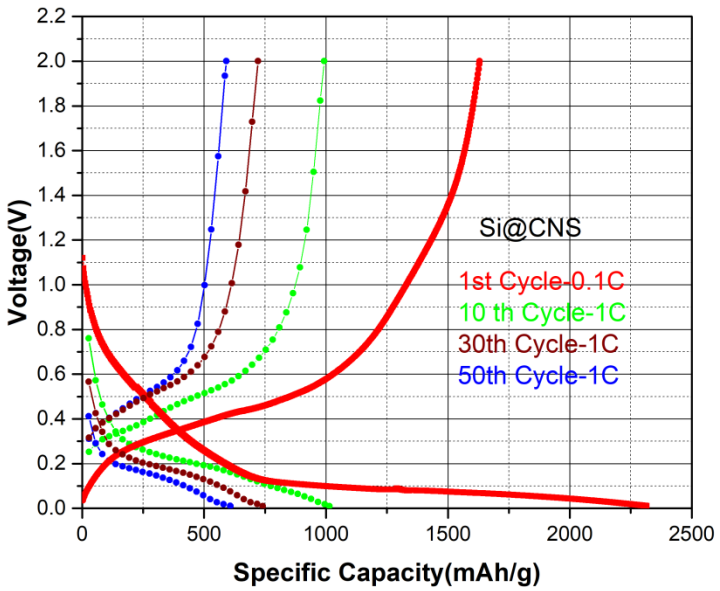

b)

Figure 4-19: a) Galvanostatic cycling and Coulombic efficiencies, b) Charge and discharge capacity of (Si@CNS)

From the performance viewpoint, the use of nanosponges gives much better results (Figure 4-19.a). The initial irreversible reaction of the silica layer here(Figure 4-19.b) is less evident while the reversible lithiation of silicon is more evident:

$$\mathbf{15}\ \boldsymbol{Li^{+}} + \mathbf{15}\ \boldsymbol{e^{-}} + \mathbf{4}\boldsymbol{Si} \rightarrow\ \boldsymbol{Li_{15}Si_{4}}$$

The lithiation capacity is always slightly higher than the subsequent delithiation which draws to a slow decrease of the cycling capacity. The use of SiO_2 passivated Si in combination with nanosponges gave great results (Figure 4-20.a). After 30 cycles the capacity is constant, almost 30% higher than the case with SiNPs. The first cycle (low current) of the lithiation step Figure 4-20.b clearly shows the alloying

process (0.25V) and the Li intercalation in the carbon material (0.1V). The reversed reactions are also visible in the delithiation process (0.45 and 0.25V).

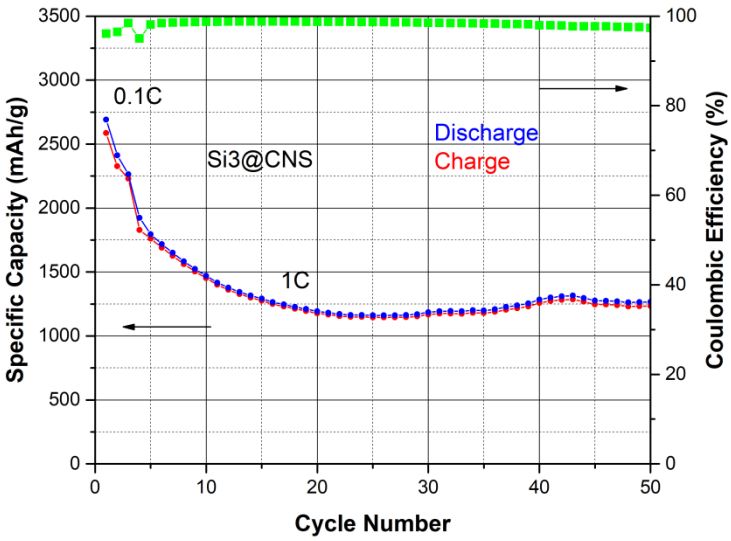

a)

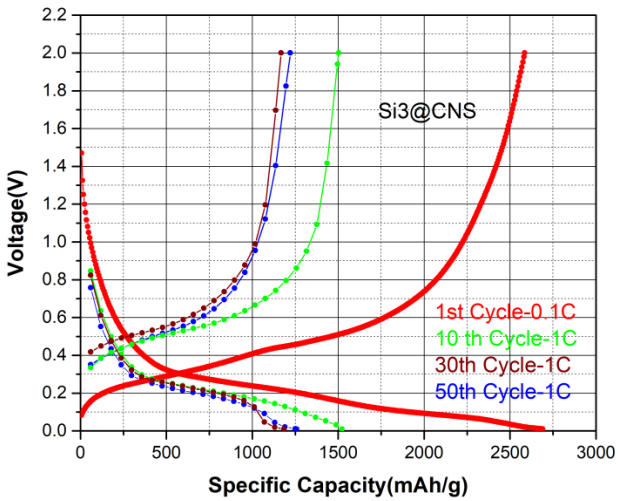

b)

Figure 4-20:a) Galvanostatic cycling and Coulombic efficiencies,b) Charge and discharge capacity of Si3@CNS

Figure 4-21 shows galvanostatic cycling performance of both Si@CNS and Si3@CNS. The cells were cycled at the same current density 0.1C for first two cycles and subsequently for 50 cycles at 1C. The significant effect of carbonized nanosponges(CNS) layer on the specific capacity is evident. All samples which were prepared onlywith reduced graphene oxide (Si-rGO, Si-rGO-3D,…), in the best condition didnot provide specific capacity more than 800 mAh/g even at a low current density of 0.1C. They demonstrate high capacity fading after first cycle.

In the embedded silicon samples, the capacity fading was very limited which means that CNS shell can buffer volume change of silicon nanoparticles. Moreover, the efficient ball milling made useable the most part of the active materials and obviously increased the specific capacity. Both samples demonstrate analogous

behavior for the first 20 cycles with a significant difference in specific capacity. For Si3@CNS, the capacity fade was lower than that of Si@CNS which can be attributed to the synergic effect of passivate oxide layer and CNS. Its specific capacity is around 1400 mAh/g while for the electrode without oxide layer this value decrease down to 600 mAh/g. It can be deduced that the presence of oxide layer on the surface of silicon nanoparticles is essential for buffering the volume change after lithiation and delithiation. After 20th cycle, the two cells follow completely different pathways. The sample with oxide layer seems to start to reconstruct its structure while the capacity of the sample without passivate layer is continuously fading.

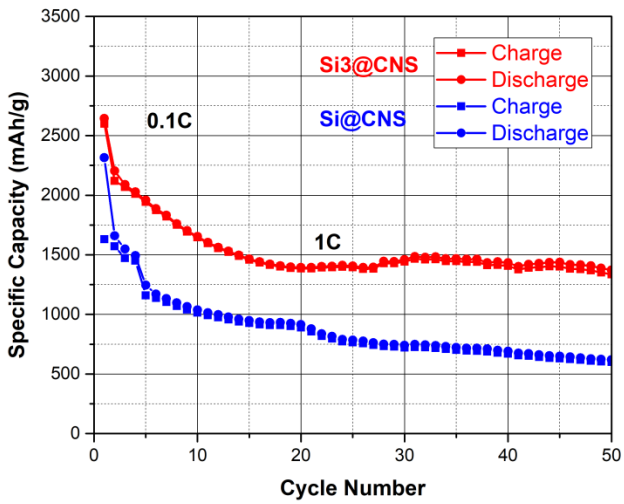

Figure 4-21: Comparison between galvanostatic cycling of Si@CNS and Si3@CNS

Based on the better performance of Si3@CNS with respect to Si@CNS it was decided to use the silicon with oxide layer for further studies.

Although the carbon black and binder can provide an integrated uniform structure to involve the Si3@CNS in electrochemical interactions, it was decided to wrap the Si3@CNS by a graphene layer for further enhancing of the electronic conductivity.

4.4.3 Graphene wrapped Silicon anode-Si3@CNS-rGO

The graphene layer wrapping was realized by homogeneously mixing the milled Si3@CNS with the graphene oxide (GO) dispersion. Magnetic stirring and sonication were used to homogenize the sample. Different ratio of GO and Si3@CNS were tested and finally the ratio GO:Si3@CNS(1:4) was selected due to the high distribution of particles on the graphene layers. Subsequently, the sample was dried and introduced in the tubular oven and the reduction processes were carried out in H_2/Ar flux in 700°C. The drying method had a notable roll on the material performance. As an initial attempt, the centrifugation and heating in air or heating under vacuum were applied for drying. The main drawback of these methods was the collapse of graphene layers and inhomogeneity of the distribution.

Finally, freeze-drying led to a very interesting improvement especially in terms of homogeneity of active material and good distribution of Si3@CNS on the reduced graphene oxide (rGO). In the previous preparations, surfactants or some polymers were used to better disperse or create the three-dimensional structure which in some cases increase the resistivity of electrode. In this work the addition of surfactant was substituted by the sonication and freeze-drying was performed without any additive. The frozen water creates an interconnected network which leaves pores after the sublimation.

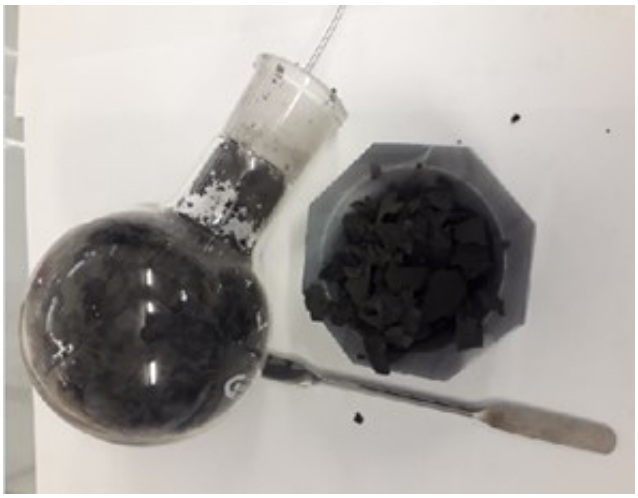

Figure 4-22: Low density Si3@CNS-rGO after Freeze-drying

400mg of Si3@CNS powder were dispersed in 100ml of deionized water in a round bottom flask and sonicated for 2 hours. Then 25ml of dispersion of GO (4mg/ml) were added and the sonication was continued for another 2 hours. The flask was quickly introduced in nitrogen Dewar and subsequently was connected to freeze-dryer for 48 hours at -50°C. At this temperature, the pressure was slowly reduced and the frozen water was sublimated. The time of freeze-drying has a crucial role to make an exfoliated material. Figure 4-22 shows the sample prepared with the explained method.

In Figure 4-23 FESEM images of Si3@CNS-rGO are reported. The graphene oxide sheets as a veil covering the nanoparticles are clearly visible. The Si3@CNs are distributed homogeneous on the surface of rGO. Moreover, it is possible to verify directional channels which facilitate electrolyte accessibility.

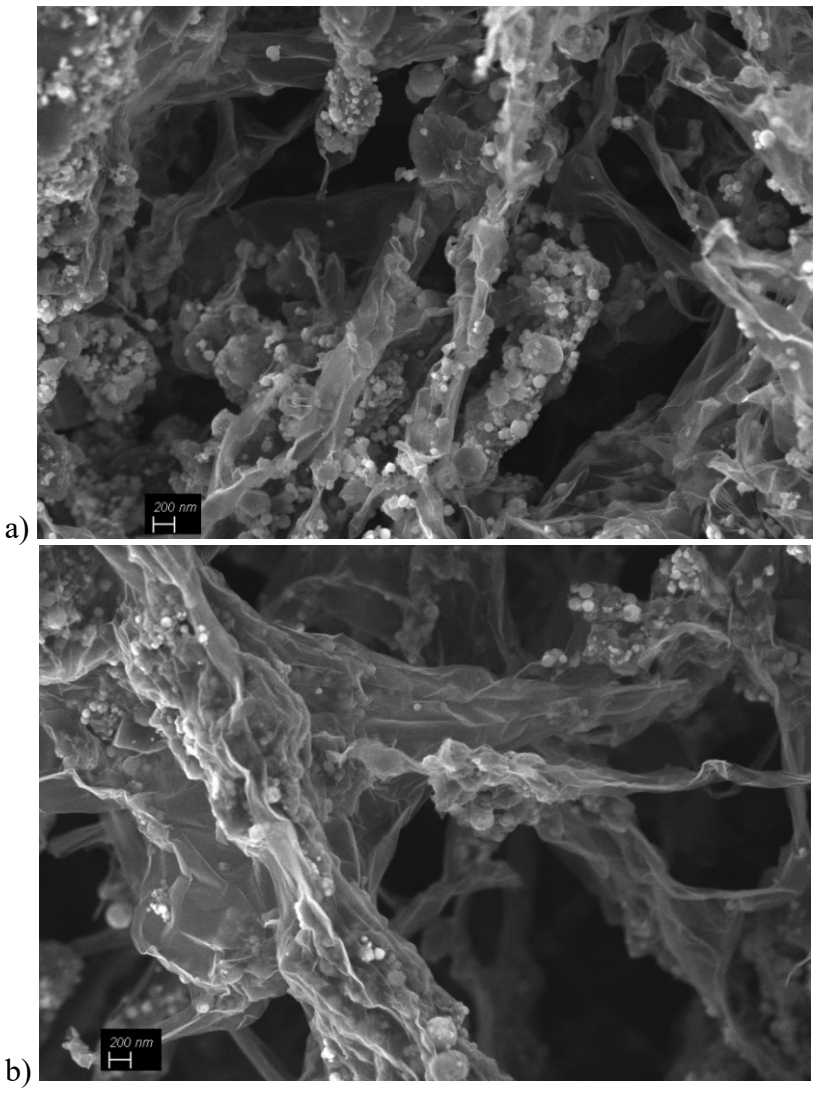

Figure 4-23: FESEM images of Si3@CNS-rGO

Figure 4-24.a illustrates the Transmission Electron Microscopy (TEM) images revealing the presence of conductive shell on the surface of nanoparticles. The inhomogeneity through layer thickness can be explained by the effect of mechanical force applied by ball milling which may be improved by further sonication. Figure 4-24-b reveals the presence of oxide layer on the surface of silicon nanoparticles. In Figure 4-24.c the rGO flakes, wrap in Si3@CNS are evident. This observation is in good agreement with FESEM images of distributed particles on the graphene network. Moreover, the thin shell on the surface of Si3 is obviously recognizable between CNS layer and graphene sheets.

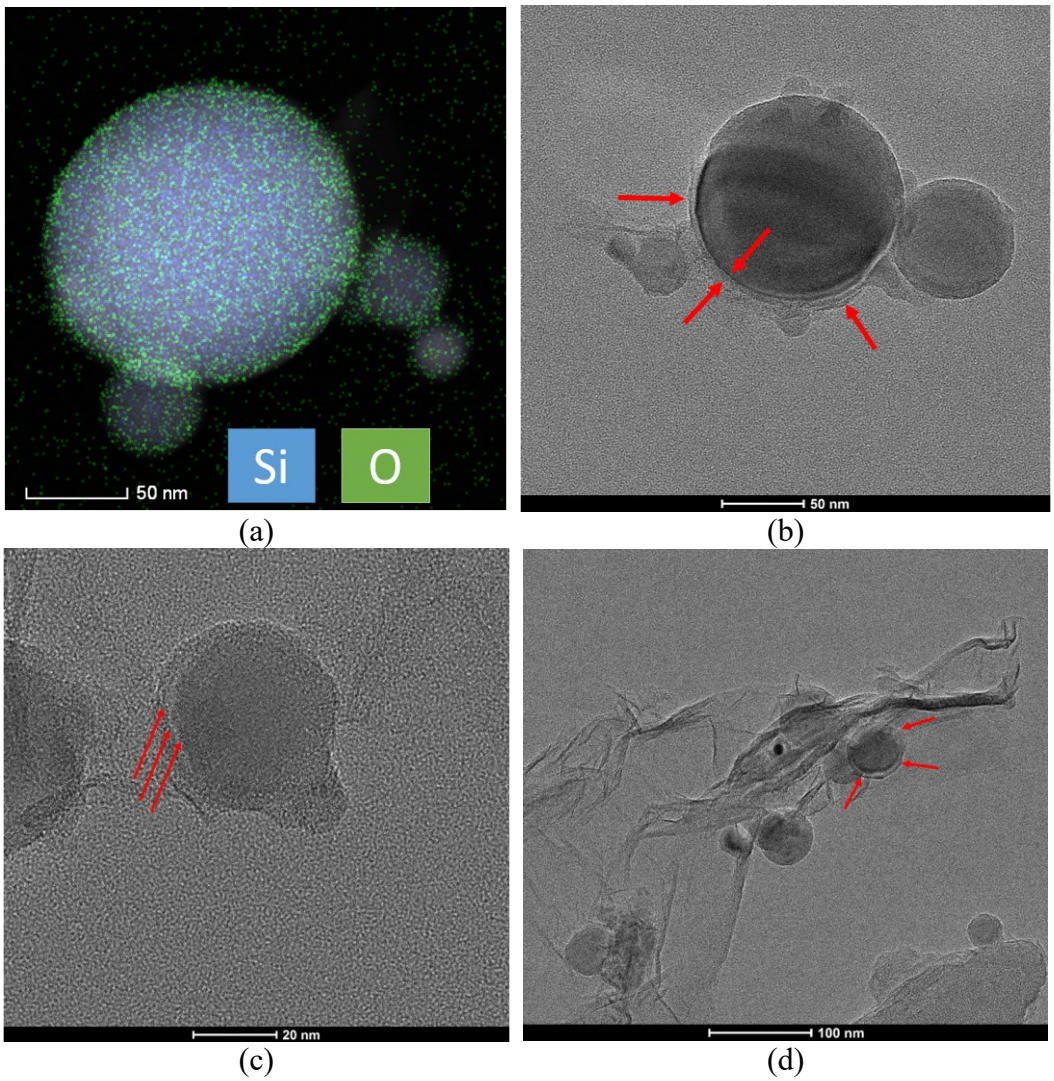

Figure 4-24: TEM images of Si3@CNS-rGO a) distribution of oxygen on the surface of SiNPs, b) presence of homogeneous carbon shell on the SiNPs,c) presence of inhomogeneous carbon shell on the SiNPs,d) the distribution of Si3@CNS on the rGO

To study crystalline structure of the final product, X-ray diffraction (XRD) was performed. The XRD patterns of Si3@CNS-rGO and Si3NPs are reported in Figure 4-25. All diffraction peaks of Si3NPs can be seen also in the final product, indicating that the silicon crystalline structure in the Si3@CNS-rGO composite retained after the embedding in nanosponge, pyrolysis, freeze-drying and GO thermal reduction treatments. The sharp diffraction peaks of fresh silicon and embedded one at 28.5, 47.5 and 56.3are overlapped and can be indexed to the lattice planes of (111), (220) and (311) of Si respectively (JCPDS no. 27-1402).

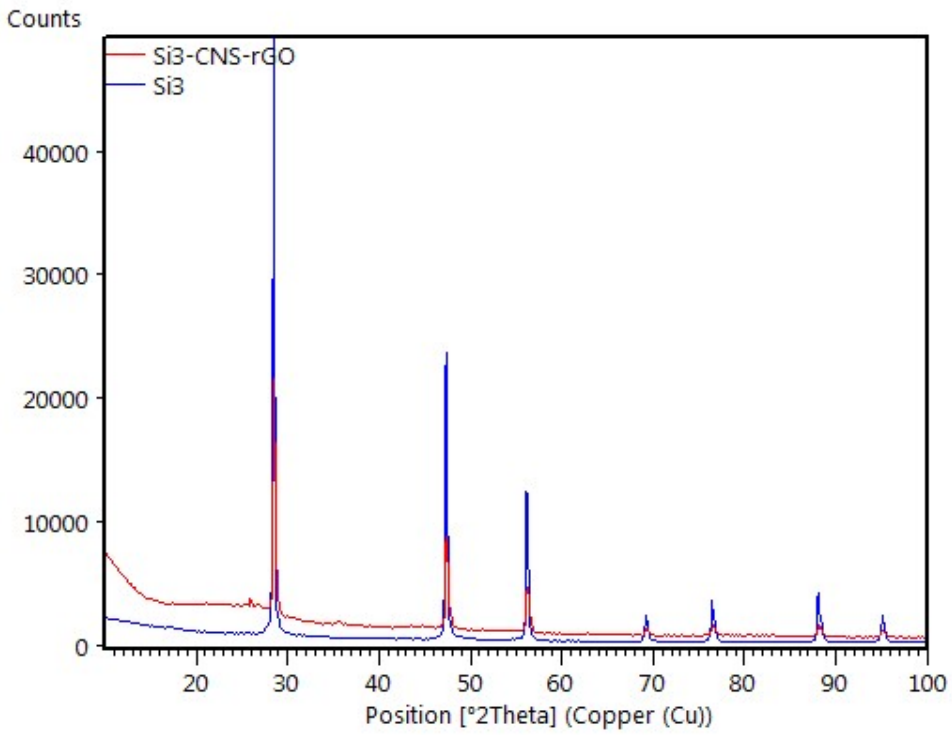

Figure 4-25:XRD analysis of passivate silicon nanoparticles before treatment (Si3) and after final synthesis (Si3@CNS-rGO)

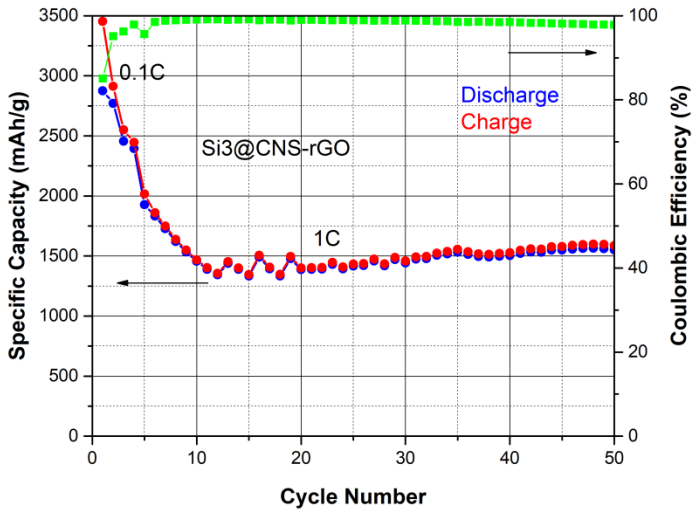

a)

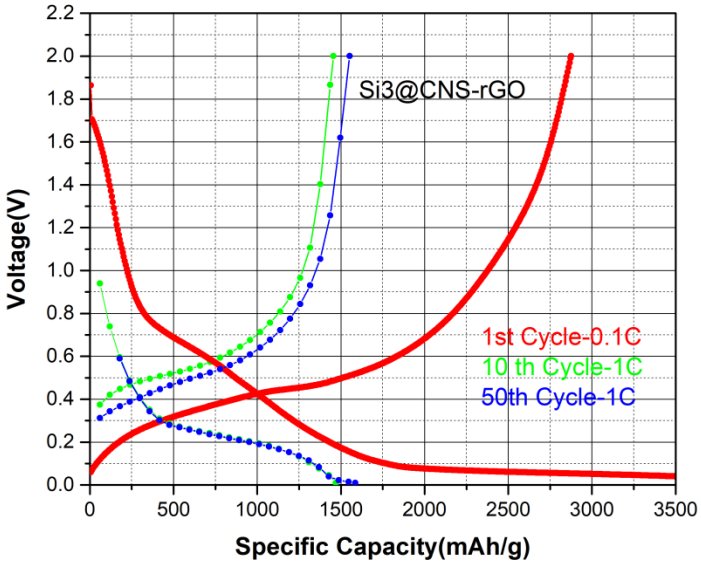

b)

Figure 4-26:a) Galvanostatic cycling and Coulombic efficiencies,b) Charge and discharge capacity of Si3@CNS-rGO

Figure 4-26.a shows the galvanostatic cycling of Si3@CNS-rGO which confirms the efficiency of embedding silicon in CNS and wrapping in rGO. The specific capacity remained more than 1500 mAh/g after 50 cycles. Figure 4-26.b depicts the voltage profile of the sample. The formation of SEI layer is evident in the first cycle. The best electrochemical performance of the material synthesized was obtained with Si3@CNS-rGO which provides a capacity slightly higher than 1500 mAh/g. Different modification methods were applied to enhance silicon active material, but they were unsuccessful. Here some of these attempts are reported:

1. To increase the conductivity of nanoparticles, during the synthesis of nanosponges, instead of pure Si, Si-rGO was introduced to create internal conductive connections between silicon and nanosponges. This method did not bring notable results because in the presence of graphene, the polymerization of cyclodextrin was not completed.
2. To increase the mass loading of silicon in the Si@CNS-rGO, after the reduction of graphene oxide, 20% extra silicon was added to the sample. The FESEM images in Figure 4-27 confirmed a surface decorated particles (Si@CNS-rGO-Si) but this material did not demonstrate significant electrochemical activation because of lack of electrical conductivity of silicon.

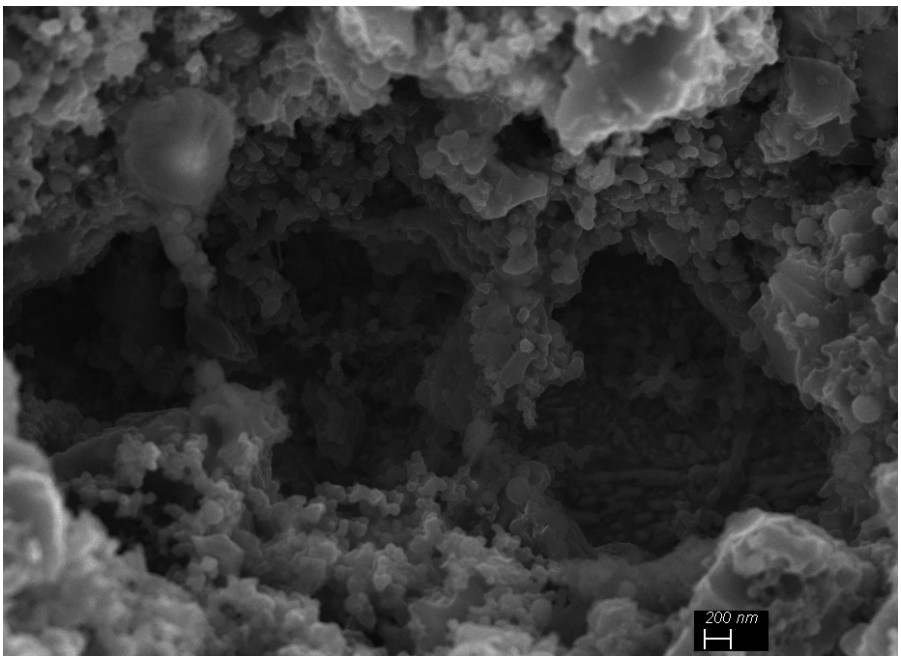

Figure 4-27: FESEM images of micrometric channel inside the electrode structure.

4.5 Electrode Fabrication

The electrode performance depends strongly on the uniformity of slurry coated on the conductive support. Generally, the slurries for electrodes contain a solvent, active material, carbon black and a binder for the cohesion between these elements and the adhesion of the electrode layer to the copper foil current collector. Inhomogeneity and different mass loadings on the electrode means a variation in the concentration of the active material which creates hot spots in the battery. The presence of hot spots leads to decreased battery life or performance and in some cases can lead to short circuit and subsequent battery explosion.[112] The fabrication of silicon electrodes must optimize the electronic and ionic conductivity. The network of solid carbonaceous particles creates pathways for electron conductivity and the pores between these solid structure are reservoir for the electrolyte which can form an ionic conductive path. The double function of the electrode is a challenging point for microstructure design because of the competition between the electronic and ionic conductivity.[113] To obtain a homogenous and flexible electrode, slurry formulation, binder effect, mixing method, electrode thickness and casting condition have to be optimized.

4.5.1 Binder effect

An ideal binder must guarantee perfect adhesion between slurry components and metallic current collectors. In fact, formation of uniform, mechanically stable and electrically conductive film electrode is the main role of binder. In case of

alloying anode like silicon with huge volume change during the lithiation/delithiation, the mechanical stability has a more significant role. Initially, non-aqueous binders such as PVDF (polyvinylidene difluoride) and organic solvents like NMP (N-Methyl-2-pyrrolidone) were used. Toxicity and cost are the main drawbacks of NMP which must be considered for an economic and eco-friendly battery.[114] In this work, different aqueous binders such as CMC (Carboxymethyl cellulose) and Sodium alginate (SA) were tested. The best results were obtained by Sodium alginate which extracted from brown algae. The high content of carboxyl group in the molecular structure of sodium alginate which are uniformly distributed, increases the possibility of bond formation with nanoparticles. [115] The network created by binder and its interaction with electrolyte, eases access of Li^+ to the particles and facilitates the formation of a stable SEI on the silicon surface.[116]

4.5.2 Mixing Method

Initially, the mixing procedure was carried out by introducing all ingredients of slurry and the solvent in a Becher under magnetic stirring for at least 2 hours. The accumulation of unmixed materials in the bottom of Becher is the main drawback of this method. Moreover, low quantity batches (around 100 mg), increases the probability of weighting error. Therefore, an innovative method by use of ball milling for slurry preparation was applied. The method consists in mixing all solid powders (silicon active material, carbon black and binder) in a mortar. Then, the powder and solvent were introduced in an Eppendorf with two balls. The Eppendorf is closed to avoid leakage and subsequently fixed in the ball milling's vessel. The optimized time and vibrational frequency were 30 minutes and 20 Hz respectively. This method was ideal for aqueous binder especially for sodium alginate. The optimal amount of deionized water was stabilized based on the porosity of carbon black and the required final viscosity.

In this method apparently trivial notions were considered which at the end drastically affect the viscosity and homogeneity of the slurry. For example, the order of introducing of the balls and powder was very important to avoid the accumulation of unmixed powders. For this reason, at first one ball was introduced in the Eppendorf and then, mixed powder, water and other ball were introduced. Figure 4-28 shows an electrode prepared by innovative method.

Figure 4-28: Flexible anode prepared with innovative method

Figure 4-29.a.b shows the FESEM images of the surface of Si3@CNS-rGO anode before and after galvanostatic cycling. There is no evidence of electrode pulverization and peeling from the current collector and the integrity of anode is conserved.

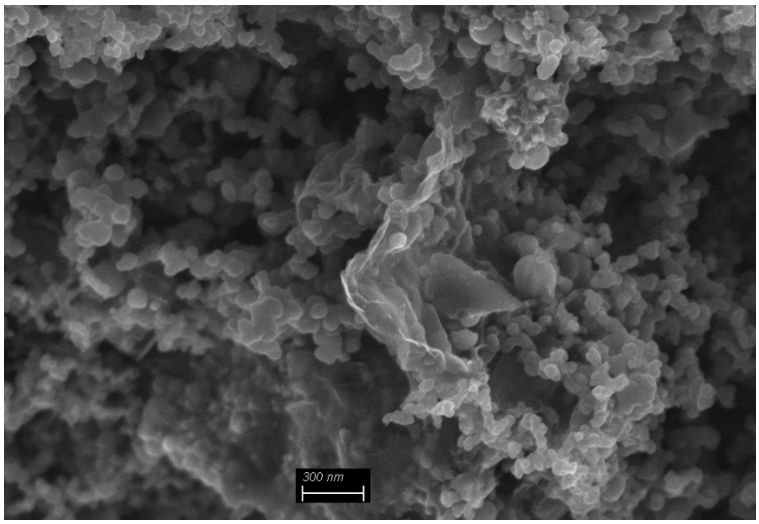

(a)

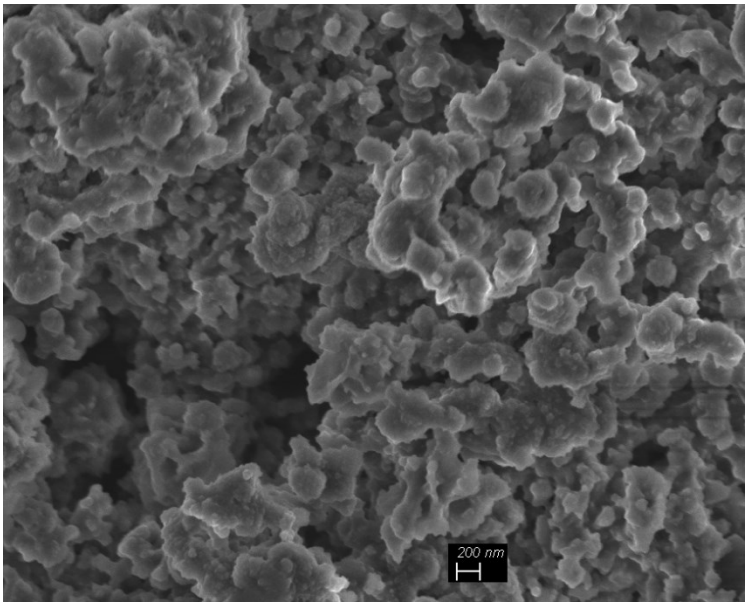

(b)

Figure 4-29: FESEM images of Si3@CNS-rGO a) before, b) after galvanostatic cycling

Figure 4-30depict the silicon nanoparticles at higher magnitude. It can be clearly seen that the silicon nanoparticles after cycling were agglomerated after lithiation/delithiation. Moreover, these particles are expanded inside carbonous matrix which facilitates theirvolume changes buffering.

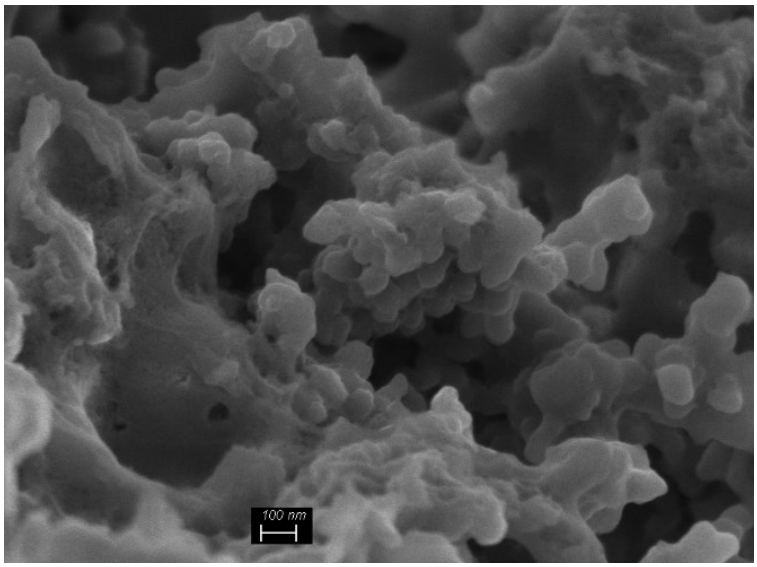

(a)

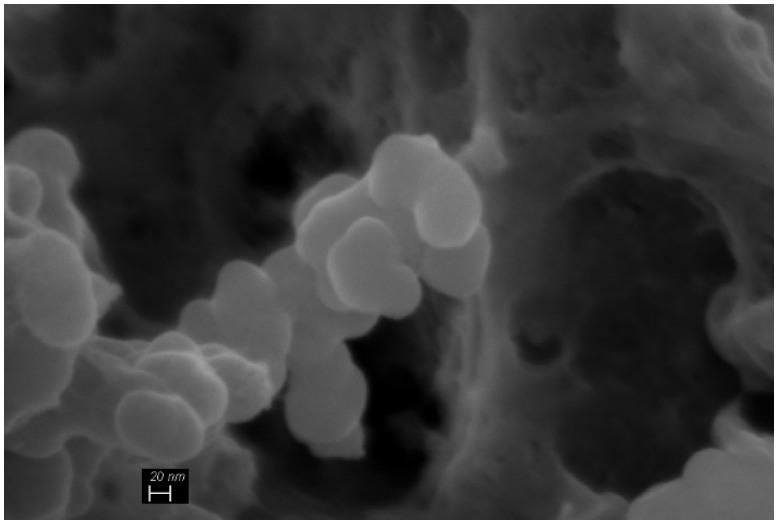

(b)

Figure 4-30: a) Agglomerated SiNPs after lithiation/delithiation, b) expanding inside carbonous matrix

4.6 Electrolyte with LiTFSI Salt and FEC Additive

To improve the performance of the silicon anode an innovative electrolyte composition was used. The idea was application of the same salt of the lithium-sulfur standard electrolyte. Moreover, different studies demonstrate the efficiency of fluoroethylene carbonate (FEC) as additive for silicon anode. L. Michan et al, suggested the reduction of FEC to vinylene carbonate (VC) and LiF, followed by subsequent VC reduction.[117]The addition of FEC significantly improves the discharge capacity retention and coulombic efficiency. This enhancement is related

to formation of smoother and more stable SEI layer structure on the silicon active material.[118] Schroder et al, demonstrate that fluoride ion formation from reduction of the FECcan attack silicon-oxide surface passivation layers and form stable SEI.[119]

Figure 4-31 shows the galvanostatic cycling of two cells assembled with Si3@CNS and Si3@CNS-rGO respectively as the active material. The electrolyte was prepared by equivolume mixture of Ethylene carbonate (EC) and Dimethyl carbonate (DMC), 1M LiTFSI and 1% FEC. The cells were cycled at 0.1C for three cycles and followed by further another 50 cycles at 1C and subsequently 50 cycles at 2C. The Si3@CNS-rGO cell demonstrate high specific capacity (2500 mAh/g) until 40th cycle. A capacity fading was observed between 40th and 50th cycles. The specific capacity at current density 2C reached to around 750 mAh/g after 50 cycles.

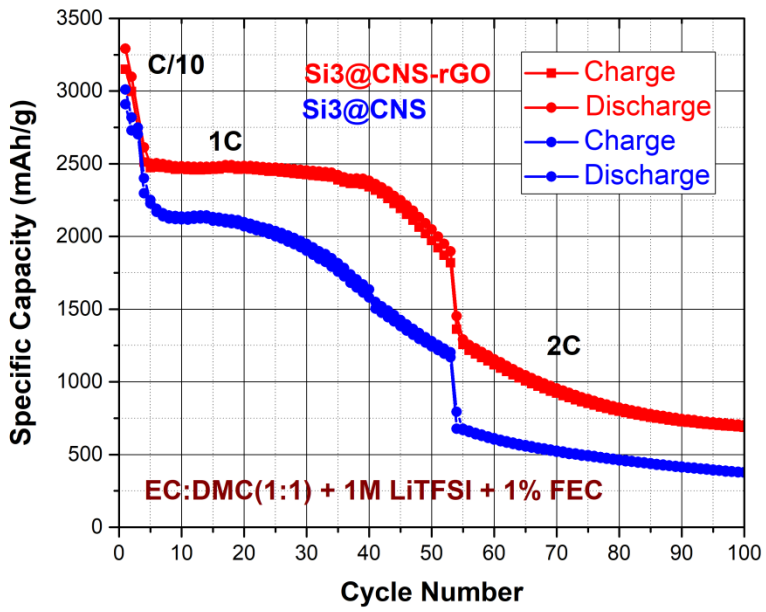

Figure 4-31: Comparison between galvanostatic cycling of Si3@CNS and Si3@CNS-rGO in the modified (EC:DMC(v:v) + 1M LiTFSI + 1%FEC)

Chapter 5 Sulfur Cathode Preparation

The insulating nature of sulfur and the dissolution of polysulfide intermediates in the electrolyte are the main issues of Li-S batteries. The cathode approach (explained in chapter 2) as a solution to reduce polysulfide dissolution requires a performant material which:

i) Creates electronic and ionic pathway with intimate contact between sulfur particles and conductive matrix
ii) Increase the utilization of sulfur active materials
iii) Mitigate the polysulfides shuttling by hosting the electrochemical reaction products in the proximity of the surface.[15]

In sulfur cathode preparation, the interaction between sulfur and the conductive matrix is the main factor which affects the cathode performance of cathode. Covalent bonds between sulfur and host carbon material seems to be the most probable interactions. The principal methods for infiltration of sulfur into carbon-based material are reported in this section.[13]

5.1 Sulfur Cathode Preparation Methods

Mechanical Intrusion:

By applying simple mechanical methods for mixing sulfur and carbon it is possible to produce some C/S composite with sulfur principally on the surface of carbon and not inside the pores.[120] With this method sulfur is physically adsorbed on the carbon suggesting weak interactions between host and gust in this composite.

Solution Infiltration:

Carbon disulfide (CS_2) at room temperature is the solvent with the highest solubility of sulfur (35 wt%). The dissolved sulfur in the solvent can reach the pores and the low evaporation temperature of CS_2 (46.3°C) makes the process independent ofheating.[121] The disposal of this solvent because of its high toxicity is a factor which must be considered.

Vapor Phase Infiltration:

This method facilitates infiltration of sulfur vapor into microporous carbon at high temperature. Most of the sulfur molecules at their boiling point (445ºC) are present in the ring-form with 6-8 atoms. At higher temperature the allotropes with 2-4 atoms appear. Smaller allotropes demonstrate different electrochemical characteristics and make the use of carbonate-based electrolytes possible.[122]

Melt Infiltration:

Elemental sulfur with S_8 allotropes has melting point at 115.2°C and in the range between 119º C and 159º C, it has low viscosity which is essential for melt infiltration into carbon. Usually the samples are heated up to 155º C to have high sulfur diffusion rate. This simple and scalable method provides sulfur mass loading control that is crucial for the C:S ratio optimization.[13]

5.2 Sulfur Cathode Active Material Based on HC-CNS

The hierarchical porous (HC-CNS) was used to prepare simple standard sulfur cathode for electrolyte characterizations. The method was previously published in paper "Journal of Solid State Electrochemistry".[92] The solution impregnation was performed by dissolving of 3 g sulfur powder (Sigma Aldrich) in 10ml carbon disulfide (CS_2) in a sealed reactor under hood. Then, 1 g of HC-CNS was added to the solution mixture under continuous stirring until complete evaporation of the solvent. For infiltration of sulfur inside the carbon pores, the dried sample was heated to 155°C for 10 h under argon atmosphere with heating ramp equal to 1°C/min. Low heating ramp was chosen to guarantee capillary penetration of sulfur in micro-pores. The sample has been naturally cooled to trap the crystallized sulfur in meso and micropores (Figure 5-1).

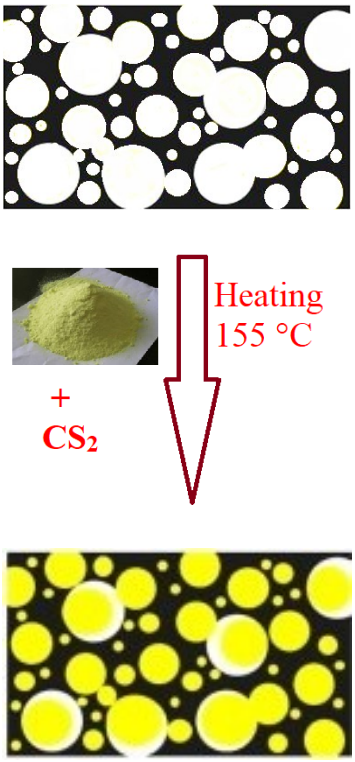

Figure 5-1: Preparation of cathode by sulfur infiltration in HC-CNS

To verify the amount of sulfur loaded in S@HC-CNS cathodes, thermogravimetric analysis was performed by a (TGA 2950 – TA Inc.). The sample was heated from room temperature to 800 °C at 10°C/min under argon flux. The TGA results confirm perfectly the ratio of sulfur: carbon (3:1) in the initial synthesis. During the TGA measurementsthe cathode sample lost 74.77% of its initial weight while the synthesis recipe was 75% (Figure 5-2).

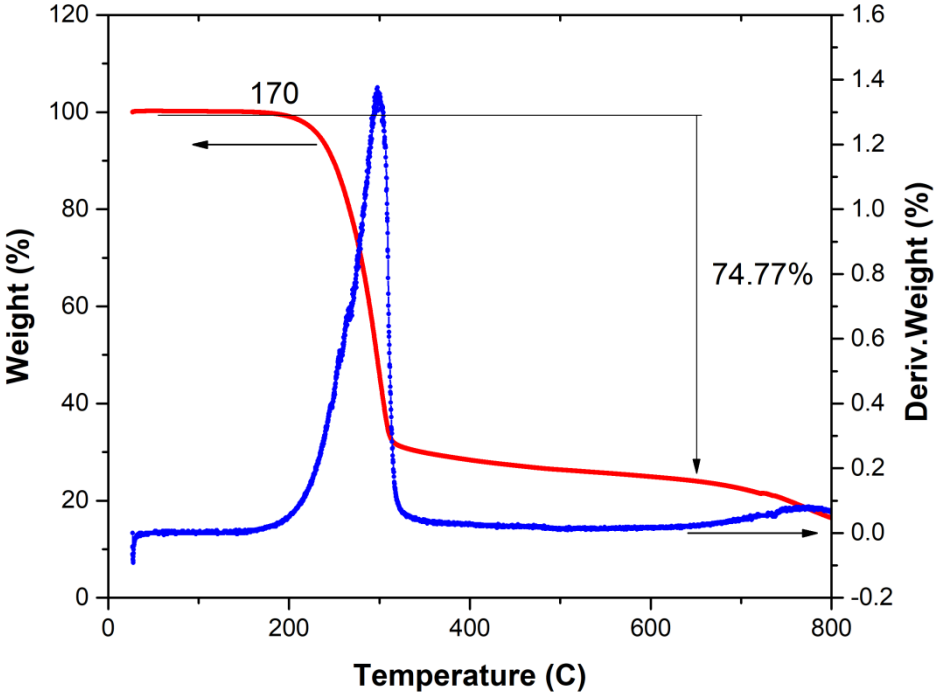

Figure 5-2: TGA curve of S@HC-CNS

High sulfur content may not correspond to the optimal S/C ratio because of the insulating nature of sulfur which could reduce the electronic conductivity of cathode. In some cases, change in the composition of slurry from 70:20:10 to 50:40:10 can improve the electronic conductivity.

Figure 5-3.a shows the morphology of porous carbon HC-CNS before sulfur loading. The presence of the mesopores with average pore width around 20 nm is evident. The Figure 5-3-b depicts the cross-section images of the sulfur loaded carbon (S@HC-CNS) composite. It can be seen that the carbonous matrix is completely covered by sulfur.

a)

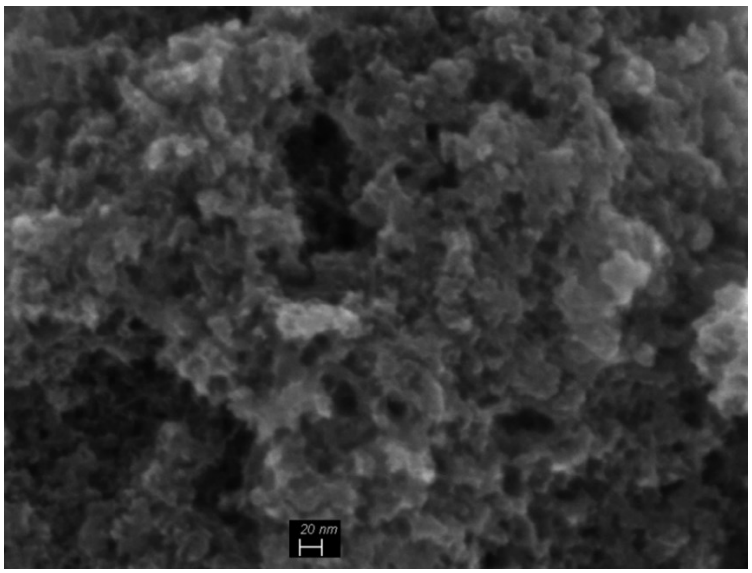

b)

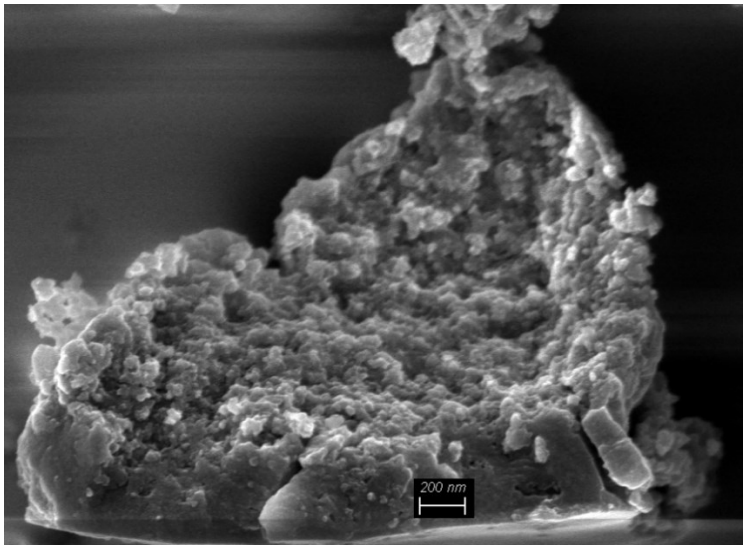

Figure 5-3: FESEM images of a) HC-CNS carbon,b) S@HC-CNS cathode

Energy Dispersive X-ray spectroscopy (EDX) was used to study the distribution and diffusion of sulfur in the carbon structure after thermal treatment. Figure 5-4 shows mapping images of S@HC-CNS sample. The accumulation of sulfur inside the pores is higher than the distributed sulfur on the whole surface of S@HC-CNS.

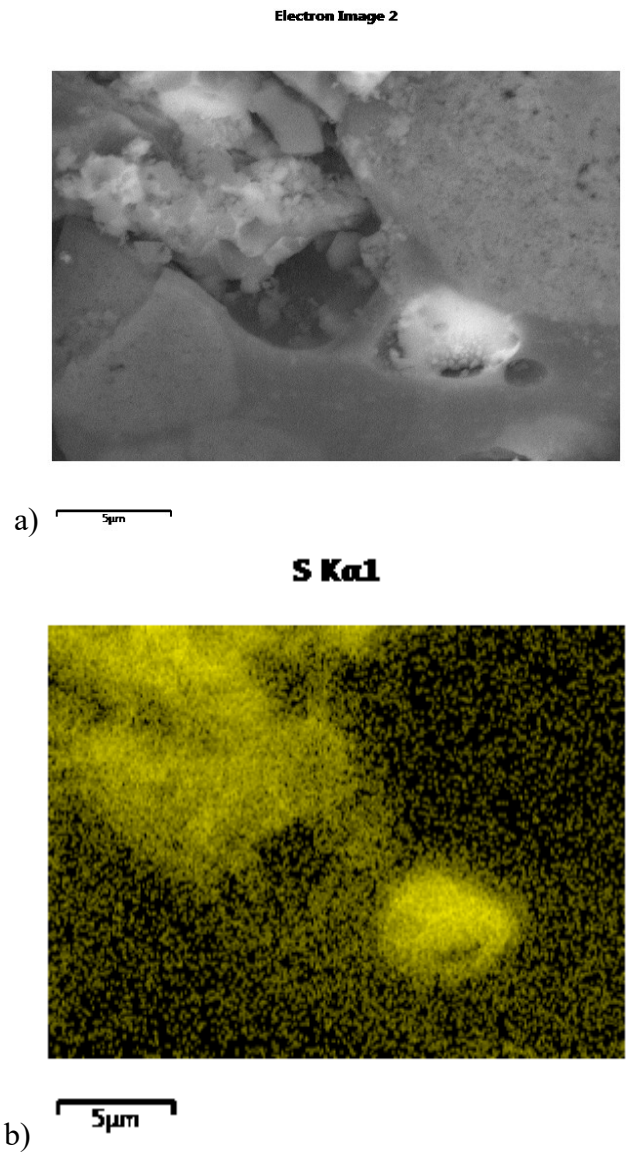

Figure 5-4: a) FESEM images of S@HC-CNS,b) Mapping distribution of sulfur on the surface and inside the pores of HC-CNS

Raman spectroscopy measurement was performed on HC-CNS, S@HC-CNS and elemental sulfur to investigate the presence of sulfur in active material. The characteristic spectra of elemental sulfur match completely those reported with literature. In case of the HC-CNS sample, at 1350 cm^{-1} D- band and at 1580 cm^{-1} G-band are fingerprint of graphitic structures. In the spectra of S@HC-CNS, the signal of sulfur is attenuated, indicating small fraction of sulfur remained on surface where as the most part is absorbed in the pores. Moreover, D-band can be associate to the effect of sulfur (Figure 5-5).

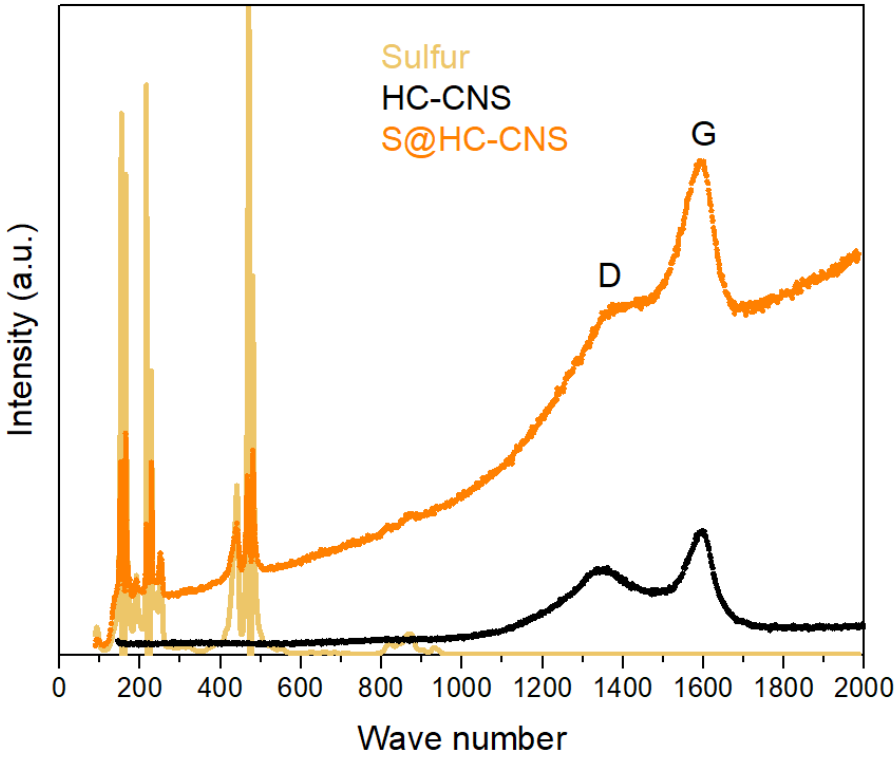

Figure 5-5: Raman spectra of S@HC-CNS

The cathode prepared through melt infiltration method provided high sulfur loading (75%). Moreover, the most part of the sulfur was inserted in the micro and mesopores which conducts sulfur reduction reactions inside the pores. Because of reproducible results, the S@HC-CNS was selected as standard cathode for electrolyte characterizations.

Chapter 6 Electrolyte for Lithium–Sulfur Cell

The dissolution of polysulfide intermediates in the electrolyte is the responsible of low charging efficiency, poor safety, short cycle life and a high self-discharge rate of the Li-S system[14]. The electrolyte has a crucial role in controlling the shuttle phenomena. To reduce the effect of polysulfide dissolution, the electrolyte has been modified according to the available strategies, in particular evaluating the possible positive effect of ionic liquids addition.

In this chapter, the attempts to find an optimum electrolyte for lithium-sulfur batteries are reported. Firstly, the solubility of common salts in the organic solvents were examined. In the second phase, different mixtures of solvents were prepared to exploit the advantages of the synergic effect of each single component. After determination of solvent mixture composition and salt type, the effect of salt concentration was investigated. Finally, the effect of ionic liquids as additives in order to reduce polysulfide dissolution was intensively investigated. In view of obtaining an electrolyte readily usable in the full Li-S cells, the choice has been limited to typical materials already widely used in the field.

6.1 Experimental Methods

The ionic conductivity of the electrolytes wasmeasured at different temperature. The measurments were carried out with AMEL conductivity cell to verify the effect of salt type and concentration. Moreover, EL-Cell was used to study the effect of separator in an assembled cell with certain quantity of electrolyte.

The dissolution of polysulfides were studied by UV-Vis on the samples extracted from separators. In addition, FESEM was used to investigate the effect of dissolved polysulfides on the metalic lithium surface.

6.1.1 Electrolyte Conductivity – Conductivity of Cell

The ionic conductivity of the electrolytes was measured by AMEL conductivity cell. The cells wereconnected to CH Instruments and the EIS was performed in the range of 1Hz - 100KHz.The resistivity of each electrolyte was calculated by reading the real term of the impedance at the highest frequency.The results were generally in agreement with the literature.

6.1.2 Electrolyte/Separator Conductivity – EL Cell

EL-Cell was used to study the effect of the separator on electrolyte conductivity.Symmetriccells were assembled by Steel/separator-electrolyte/ Steel architecture in Argon-filled glove-box. The cells were put in an environmental

chamber (temperatures from 25 to 80°C) and connected to CH Instruments. The EIS was performed in the range of 1Hz - 100KHz. Firstly, the samples were scanned at room temperature then the temperature was increased by 10º C for further measurements until 80ºC. At each step, the cell was left for at least one hour to assure a homogenous thermal distribution in the core of the cell. The resistivity of each electrolyte was calculated by reading the real term of impedance at the highest frequency.

6.1.3Polysulfide Measurement

In the literature there are many works reporting on the characterization of polysulfide in electrolyte by ex-situ, in-situ and in-operando methods for measurement of dissolution of polysulfides in electrolyte. Han et al. applied ex-situ Raman and XRD which confirmed the effect of TEGDME additive to reduce lithium polysulfides shuttle effect.[123] In-situ XRD was applied to study the morphological and structural changes of the sulfur cathode during the cycling. This method provides information about the Li_2S which forms at the second plateau at 1.8V and the recrystallization of sulfur as smaller particles.[124]Diao et al. measured the total content of sulfur by ICP-OES (Inductively coupled Plasma-Optical emission spectrometer) and LC-MS (Liquid chromatography coupled with mass spectrometry) to separate polysulfide with different order. Li_2S_4 and Li_2S_6 were proved to be the most stable form of lithium polysulfide species.[125]

UV-Vis spectra can provide useful information about the sulfur reduction mechanism. Barchasz et al, applied ex-situ method and reported UV-Vis bands for different species which form during S_8 reduction. The elemental sulfur S_8 has a sharp peak at 280 nm while the peaks in the range 400-600nm are associated to long chain polysulfides. The intermediate species such as S_6^{-2}or S_4^{-2} have shoulder peaks in the range 300-400 nm.[126] In operando UV-Vis can reveal quantitatively and qualitatively sulfur reduction intermediate products. In the UV-Vis spectra, five peaks are recognizable which are associated to different order polysulfides.[127]

For polysulfide measurement a sulfur-carbon cathode based on carbonized nanosponges (S@HC-CNS) was prepared as reported in chapter 5 and used as the standard cathode for electrolyte characterizations. Such an electrode proved to be simple in its preparation and yet with a stable and reproducible behavior. The type of separator, the composition and quantity of electrolyte were the variables under examination. The galvanostatic cycling of the cells were performed at current density 0.2C and the cells were left in discharged state. Later on, the cellswere opened in argon-filled glove-box in order to analyze separator and lithium anode. The separators were immersed in DME/DIOX (v:v) mixture to extract dissolved polysulfides. The UV-visible analysis was performed on the solutions extracted from the separators.

6.2 Ether-Based Solvent Mixture Electrolytes

The low viscosity and low surface tension in liquid electrolytes provide good electrode wetting and enable the electrolyte to penetrate into the porous cathode structure. In addition, the large dielectric constant of organic solvents facilitates the dissolution of lithium salts which consequently leads to higher ionic transfer rate.[66]Kikuko et al, suggest a mixture of solvents having a high dielectric constant and viscosity with a co-solvent having a low viscosity and dielectric constant to obtain synergic effect on the ionic conductivity.[66]

In chapter 2 the most important organic solvents were discussed. The ether-based solvents as the most proper candidate for lithium-sulfur batteries were also reviewed.

Gao et al. have studied the effect of solvents combination with different ratios on the specific capacity by in situ X-ray absorption spectroscopy (XAS). The four solvent mixtures included DOL-DME (1:1), PC/EC/DEC (1:4:5), EMS/DEC(8:1) and EMS/DOL/DME (4:1:1).[65]They demonstrated that an equivolume mixture of DOL/DME provides the highest discharge capacity. Instead, PC/EC/DEC and EMS/DEC electrolyte delivered very low capacity. XAS analysis revealed similar stable discharge products in ether-based electrolytes, while in the carbonate-based ones the reduction products are radical anions which chemically react with the solvent.[65]

Based on the results of previous cited works, DOL/DME (1:1) was chosen as the organic solvents mixture for the electrolyte study.

6.2.1 Lithium Salts

To evaluate the effect of salt type, three 1M$LiClO_4$ and three 1MLiTFSI solutions with different solvent ratio mixtures were prepared. Different studies show the effect of lithium nitrate ($LiNO_3$) as electrolyte additive in Li–S cells to increase the coulombic efficiency and cycling stability. It is supposed that $LiNO_3$ reacts with metallic lithium to form a protective layer which limits the effect of polysulfides.[128] Forthis reason, 0.25M$LiNO_3$ + DME:DIOX (1:1) was used as electrolyte mixture. To further investigate the effect of solvent volume ratio, the DME:DIX (7:3) and (3:7) were also prepared. The ionic conductivity of each sample was measured by AMEL cell and the results were found to be in agreement with the literature.[129]

Table 6-1: Effect of salt and solvents mixture ratio on the ionic conductivity

	DME:DIOX (7:3)	**DME:DIOX (1:1)**	**DME:DIOX (3:7)**
1M $LiClO_4$	3.2 mS/cm	4.8 mS/cm	3.9 mS/cm
1M LiTFSI	4.5 mS/cm	8.1 mS/cm	5.8 mS/cm

LiTFSI salt, showed higher ionic conductivity with respect to $LiClO_4$ salt in all mixtures. The electrolyte with (1:1) volume ratio of solvents and LiTFSI salt (DME:DIOX (1:1) + 1M LiTFSI + 0.25M $LiNO_3$) showed the highest ionic conductivity (8.1 mS/cm).

6.2.2 The Effect of Salt Concentration on the Ionic Conductivity

High lithium salt concentration can improve the safety of cell by suppressing dendrite growth on the lithium metal surface. Moreover, it is supposed that high salt concentration can inhibit the dissolution of polysulfide intermediates in electrolyte.[130] Thesalt concentration is a crucial factor to determine the mobility and diffusivity of the ions. On the other hand, the salt concentration can drastically change the viscosity of electrolyte. As mentioned before, the DME:DIOX (1:1) + 1M LiTFSI + 0.25M $LiNO_3$demonstratedhigher ionic conductivity. To investigate the effect of salt concentration, two solutions (2M and 4MLiTFSI)were also prepared.

Symmetric EL-Cell cells were assembled by Steel/separator-electrolyte/ Steel architecture in argon-filled glove-box.Arrhenius plots of the ionic conductivity of the electrolytes are reported in Figure 6-1. It can be seen that the electrolyte with the lowest salt concentration showed the highest ionic conductivity at almost all temperatures. Based on these observations, it was decided to use the conventional electrolyte of lithium-sulfur (DME:DIOX (1:1) + 1M LiTFSI + 0.25M $LiNO_3$) with C2500separator.

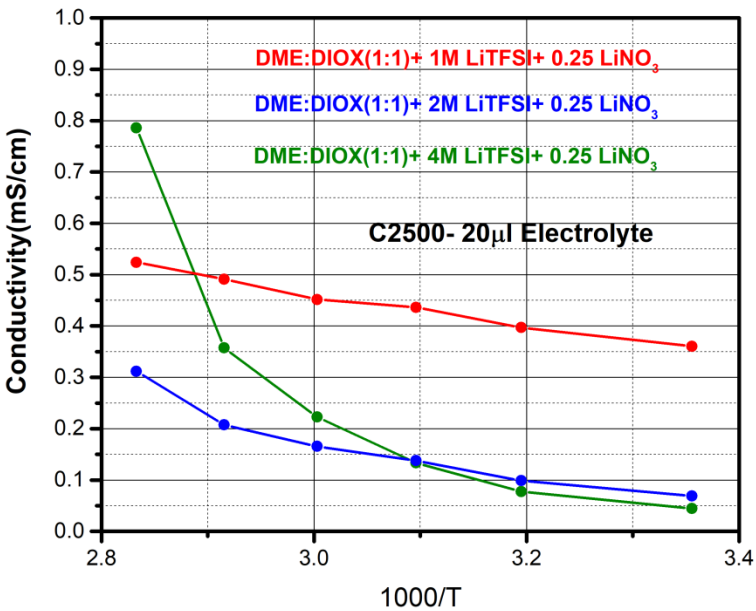

Figure 6-1: Arrhenius plots of the ionic conductivity of the electrolyte with three (1M,2M,4M) concentrations-C2500

6.2.3 Performance of Li-S Cell with Ether-based Electrolyte

To evaluate the effect of electrolyte composition on the performance of the Lithium-Sulfur battery, EL-Cells were assembled with architecture Li/Separator-Electrolyte/S@HC-CNS. Initially, the measurements were performed with use of Celgard2500. In addition, Whatman fiber glass separators with pore size 1.6 µm and thickness around 250 µm were applied.The required quantity of electrolyte for C2500 is around 20 µL while this value for Whatman fiber glass is at least 80 µL to complete wetting.

Figure 6-2depicts the galvanostatic cycling of the cell with standard electrolyte and Whatman separator. The first cycle (Figure 6-2.a) provides a specific capacity around 1000 mAh/g but it is followed by capacity fading in the next cycles. This behavior is related to the continuous dissolution of polysulfide in ether-based electrolyte. The first cycle at current density of 0.1C shows the profile of the charging – discharging potential curves (Figure 6-2.b) is typical of the Li-S system.[14] In the further cycles at current density of 0.2C the dissolution of polysulfide in the high quantity electrolyte (80µL) causes rapid capacity fade. Moreover, the low coulombic efficiency is related to unrecovered sulfur and polysulfide after each cycle. After 20th cycle almost all sulfur is dissolved in electrolyte. This also evident from the intense color of the extracted solution from the separator.

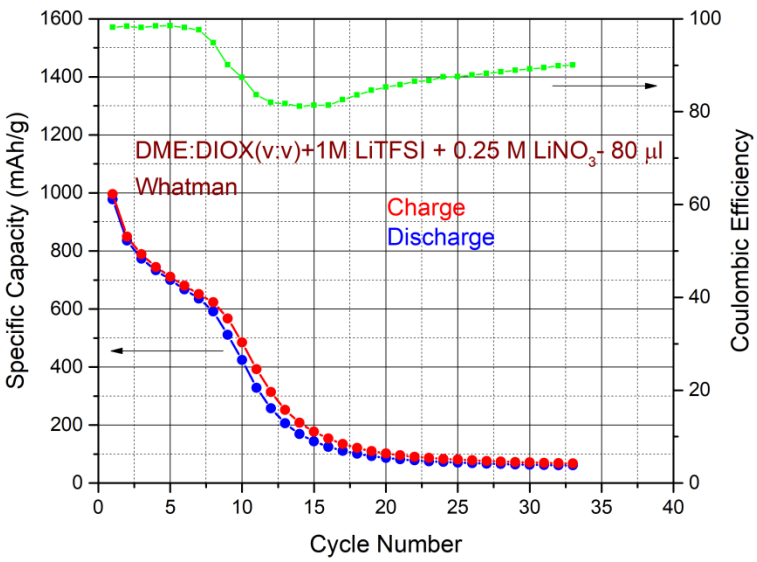

a)

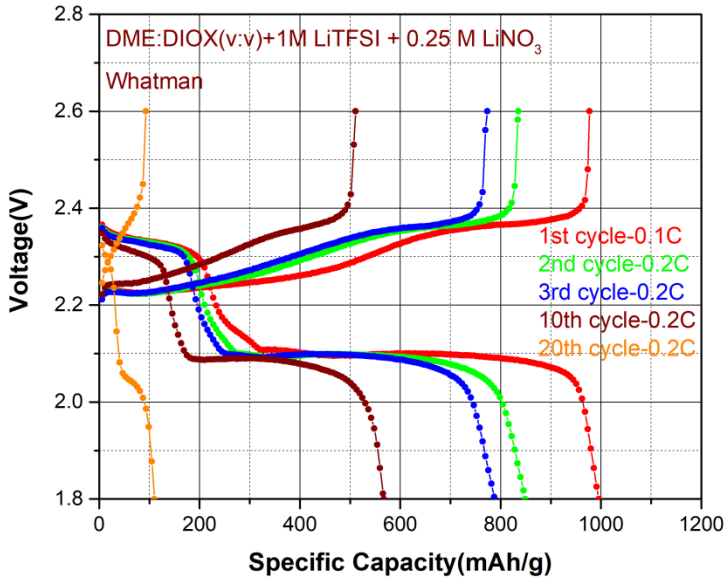

b)

Figure 6-2: a) Galvanostatic cycling and Coulombic efficiencies,b) Charge and discharge capacity of the cell with STD.W

To evaluate the effect of polysulfide on the metalic lithium and its solubility in the electrolyte,the galvanostatic cycling of the cells was performed at current density 0.2C and the cells were left in the discharged state then were opened in argon-filled glove-box in order to studythe separator and lithium anode. The separators were immersed in DME:DIOX (1:1) mixture to extract dissolved PS. The UV-visible analysis was performed on the solutions extracted from separators. The metallic lithium was conserved in the glove-box for morphology characterization.

Figure 6-3.a shows the FESEM image of the surface of lithium with standard electrolyte and Whatman separator. The micrometric lines that are formed on the surface of lithium disk are signs of interaction with polysulfides. Figure 6-3.b reports the EDX and mapping of distribution of sulfur on the surface of the anode. The corrosion lines confirm remarkable reaction at the anodic surface which is related to the presence of sulfur-based compounds dissolved in the electrolyte. Figure 6-3.c demonstrates the solution extracted by DME:DIOX mixture from the separator. The intense color is due to the high concentration of polysulfides dissolved in the electrolyte.

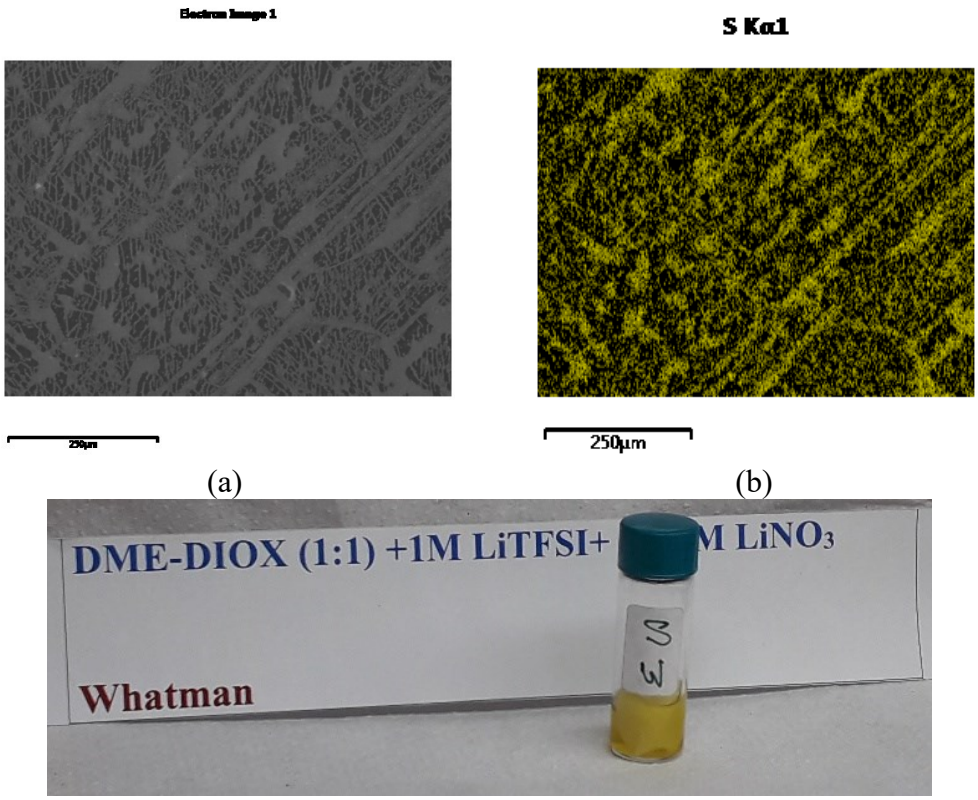

(a) (b)

(c)

Figure 6-3: a)FESEM image of lithium surface, b) sulfur mapping on the surface of lithium,c)extracted polysulfides from separator of the cell with STD.W

Figure 6-4.a shows the galvanostatic cycling of the cell with standard electrolyte and Celgard2500. In the first cycle at current density of 0.1C the discharge–charge is lower than the Whatman cell. The capacity fading was observed for cycles at 0.2C but after 5th cycle the capacity starts to increase. This behavior can be associated to the lower wetting of the Celgard separator with the electrolyte. The increase in capacity, may be due to the progressive wetting of the separator and the cathode. The difference between discharge and charge capacity was observed also in this case which is related to the polysulfide dissolution and non-complete recovered sulfur compounds. The cell provides higher specific capacity with 36% capacity loss after 50 cycles while the cell with Whatman, lost more than 90% of its initial capacity. The two separators appear to markedly influence the cell performance. Celgard allows a high initial capacity value which shows rapid fading while Whatman shows a lower capacity which is maintained throughout the cycles. It is important to take it account also the difference between electrolyte volume (Celgard2500- 20µl and Whatman 80 µL).

Figure 6-4.b shows voltage profile of the cell with standard electrolyte and Celgard2500 separator. The formation of Li_2S_8in high reduction potential (around 2.3V) is almost the same for all cycles. The plateau in lower reduction potential (around 2.1V) shows different trend by increasing the cycles.

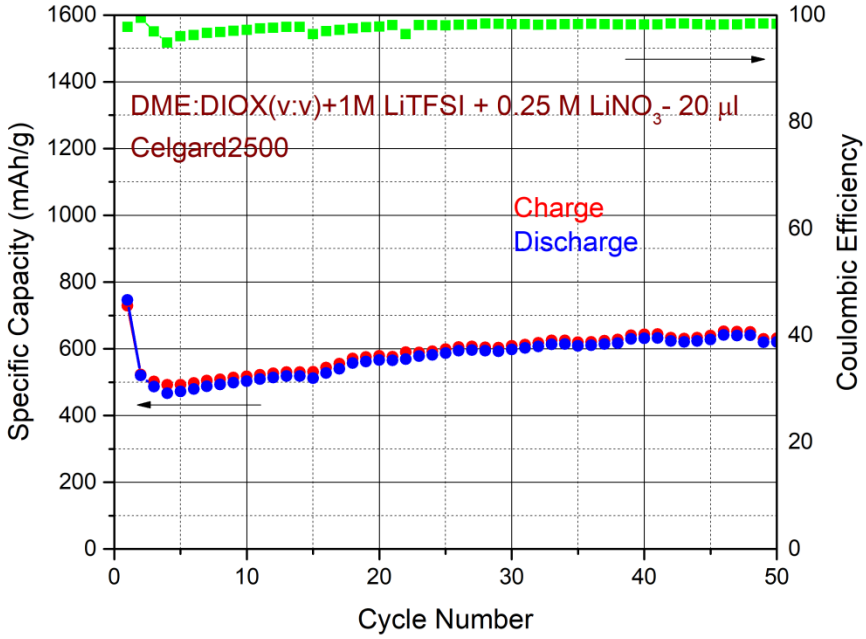

a)

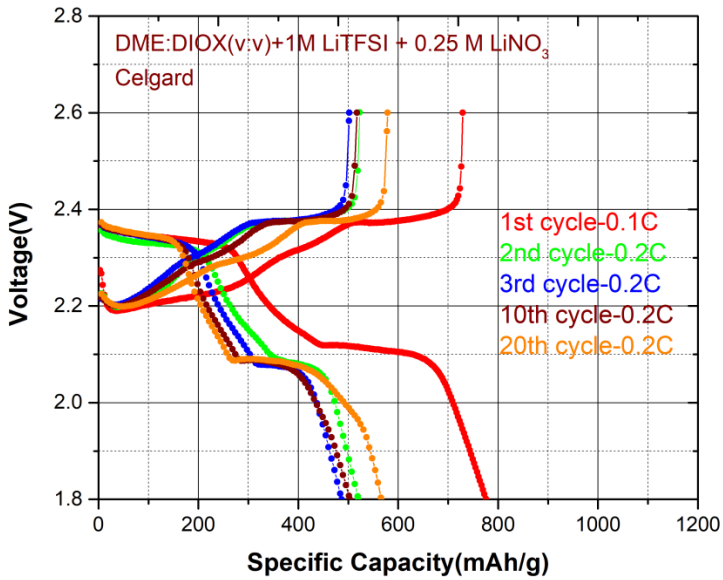

b)

Figure 6-4: a)Galvanostatic cycling and Coulombic efficiencies, b) Charge and discharge capacity of the cell with STD.C

Figure 6-5.a shows the FESEM image of the surface of lithium with standard electrolyte and Celgard2500 separator. The difference between the corrosion pattern in this case and Whatman separator is evident. Figure 6-5.b depicts the distribution of sulfur compounds on the surface of lithium. In this case, the less corrosion on the surface was observable even with naked eyes. Figure 6-5.c shows the solution extracted by DME:DIOX mixture. The extracted solution from the

separator in this case has lighter color because of the lower amount of dissolved polysulfides in 20µL electrolyte.

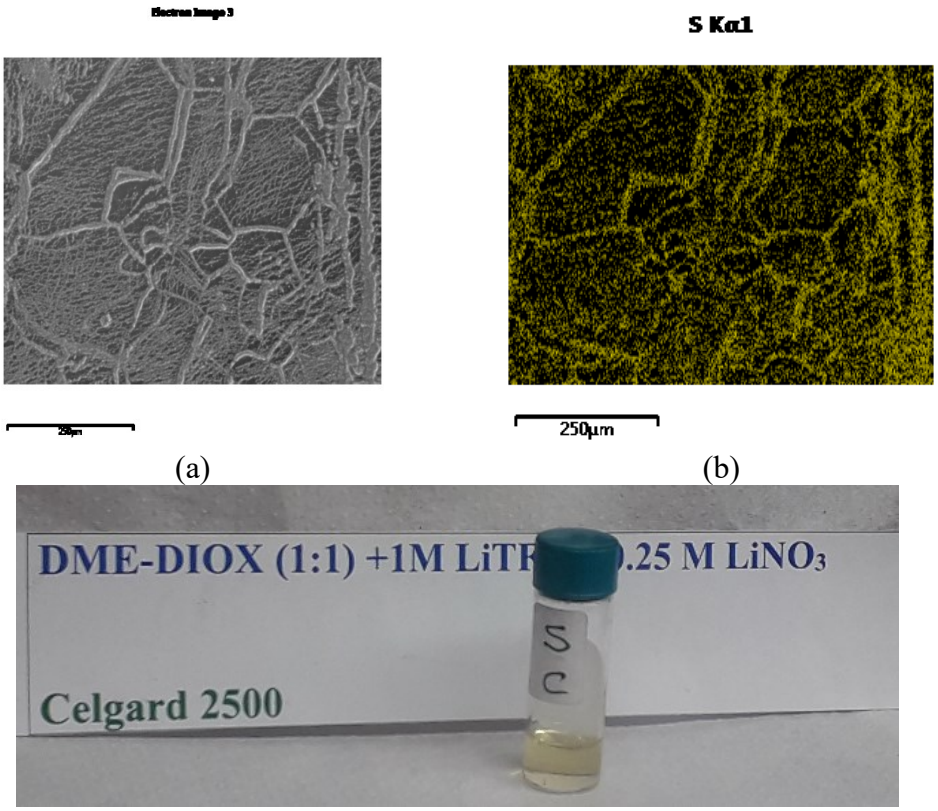

Figure 6-5:a)FESEM image of lithium surface,b)sulfur mapping on the surface of lithiumc) extracted polysulfides from separator of the cell with STD.C

UV-visible analysis was performed on the solutions extracted from the both of the separators. In both separator cases the peaks around 260 and 340nm are attributed to S_6^{-2} species. The peak observed at 420nm confirms the presence ofS_4^{-2}.[131] The peak at 610nm is in agreement with the peak at 620nm found by Patel et al. attributed to long chain polysulfides.[127]In any case, peak intensity of Whatman cells is higher than Celgard2500 cells. It was also seen in difference between colors of two extracted samples.

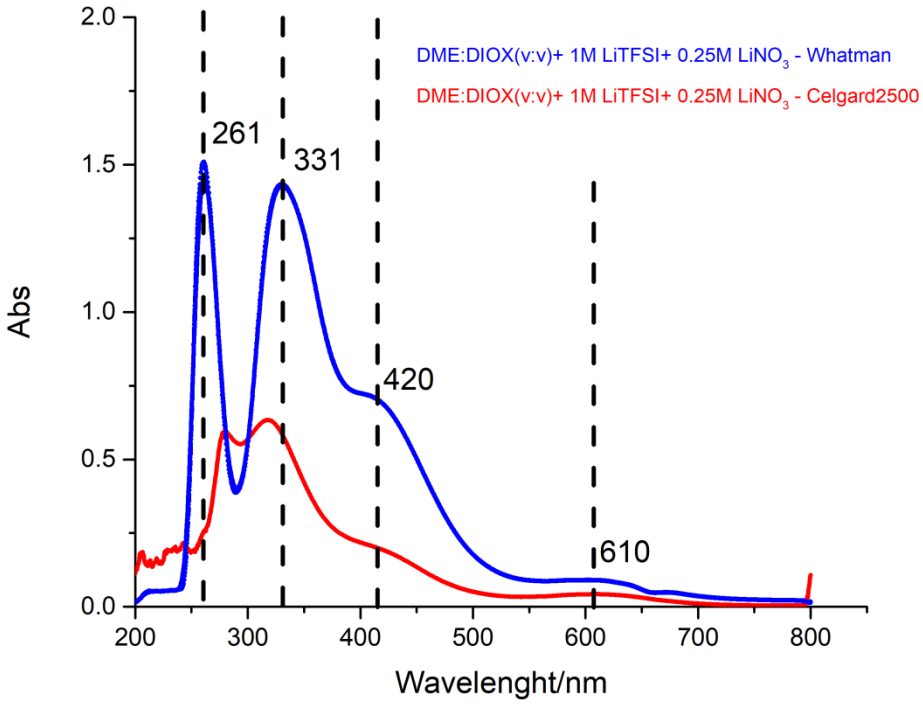

Figure 6-6: UV-Vis spectra of standard electrolyte

6.3 Ionic Liquids-Based Electrolyte for Lithium-Sulfur Batteries

Ionic liquids demonstrate low polysulfide solubility which could help in reducing shuttle effect. Wu et al, showed that a Li-S cell having a mixture of TEGDME and P1,2O1TFSI with weight ratio (7:3) as an electrolyte, provides a capacity retention around 93% after 100 cycles.[132] A mixture of high viscosity of PP13-TFSI and DME in the electrolyte provides high coulombic efficiency, cycling stability and specific capacity.[133]

The choice of anion/cation of ionic liquids is based on its compatibility with organic solvents and salt of lithium-sulfur battery. Since LiTFSI is the most common salt used in lithium-sulfur batteries, $TFSI^{-}$was selected as anion for ionic liquid.

Park et al. demonstrated the low solubility of sulfur and different polysulfides in PYR13TFSI. In addition, the cell with PYR13TFSI electrolyte showed high stability in galvanostatic cycling.[134]

PYR13TFSI ionic liquid was chosen due to the above mentioned characteristics which improves the performance of Li-S batteries. In this section the synthesis of ionic liquids is reported.

6.3.1 Ionic Liquid Synthesis

The synthesis of the hydrophobic PYR_{13} TFSI ionic liquid through the aqueous route was performed through five iterative steps:

I. Purification of chemicals
II. Synthesis of PYR13Br precursor
III. Purification of the PYR13Br precursor
IV. Synthesis of the PYR13TFSI ionic liquid
V. Rinsing of the PYR14TFSI ionic liquid

I. Purification of chemicals

N-methylpyrrolidine (PYR1, Acros, 98 wt.%) and 1-bromoropane (1-Br-Pro, Aldrich, 99 wt.%) were chosen as chemicals. To achieve high purified ionic liquid, the chemicals were purified through activated carbon and alumina.

The purification of PYR1 was performed by adding activated carbon and alumina with respectively 30% of the PYR1 weight (total 60%) to glass reactor and maintain under stirring for 12 hours. Br-Pro was purified with the same materials with 15% of weight(total 30%). The separation of chemicals from the purification agents was performed by vacuum filtration with PTFE filter.

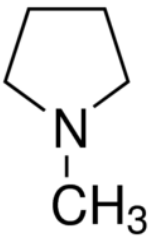

a)

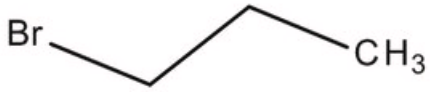

b)

Figure 6-7: The chemical structure of a) N-methylpyrrolidine, b) 1-bromoropane

II. Synthesis of PYR13Br precursor

The precursor (PYR13Br) was obtained through electrophilic addition reaction between PYR1 and 1-Br-Pro.

PYR1 with 0.5% excess with respect to the stoichiometric value (20.66 g) was dissolved in the same volume of deionized water (PYR1: H2O- 1:1). The reactor under magnetic stirring was immersed in an oil bath for homogenous heating at 70ºC. A previous study showed the highest yield at 70ºC.[135] Subsequently, 29.69 g of 1-Br-Pro was introduced into the reactor and the mixture was stirred about 20 min. As the 1-Br-Pro is not soluble in water, a biphasic mixture (separated liquid phases) was observed. The difference between densities (1-Br-Pro density = 1.354 g/cm^3; PYR1 density = 0.819 g/cm^3) made the lower phase rich in the heavier 1-Br-Pro while the upper one was mainly a PYR1/water mixture. A progressive decrease of the lower phase and increase in the upper one indicates formation of water soluble PYR13Br precursor. The reaction goes on until complete disappearance of the phase separator indicating yield of 100%.

PYR1(aqueous) +1−Br-Pro →PYR13Br(aqueous)

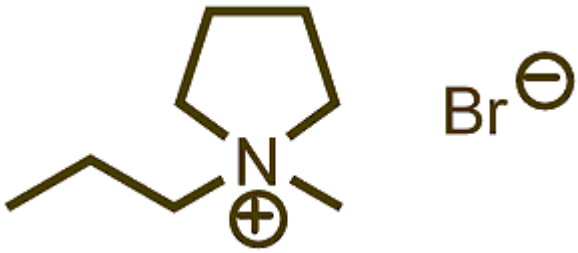

Figure 6-8: The chemical structure of N-Methyl-N-propylpyrrolidinium bromide

III. Purification of the PYR13Br precursor

The precursor (PYR13Br) was purified through standard carbon and alumina in weight ratio 60% and 90% respectively with respect to the weight of PYR13Br. The mass of precursor was (20.66+29.69=50 g) therefore 30g of activated carbon and 45g of alumina were added to sample and the resulting slurry was stirred at room temperature for 18 h. Then, the purification agents were separated from the liquid by vacuum filtration (Whatman-Polyamide).

IV. Synthesis of the PYR13TFSI ionic liquid

To prepare PYR13TFSI, 70g of LiTFSI salt (lithium bis(trifluoromethanesulfonyl)imide) with 3% excess was added to 50g PYR13Br. After rapid anion exchange reaction between the $PYR13^{+}$cation and the $TFSI^{-}$anion two liquid phases were formed. In this step, lithium bromide (LiBr) forms as a byproduct. For purification, PYR13TFSI was washed 7 times with deionized water. Argentometry method was applied to verify the purification level of ionic liquid after rinsing. After argentometry, the sample remained perfectly transparent andno sign of precipitation of silver salts was observed which means that the rinsing of ionic liquid was efficient.

Tocontrol further the presence of salt (LiBr), conductivity test was performed on aqueous supernatant. The initial conductivity was 6.81 mS/cm and the last one 0.7 mS/cm (700µS/cm).

PYR13Br(aqueous)+LiTFSI(solid)→PYR13TFSI(liquid)+LiBr(aqueous)

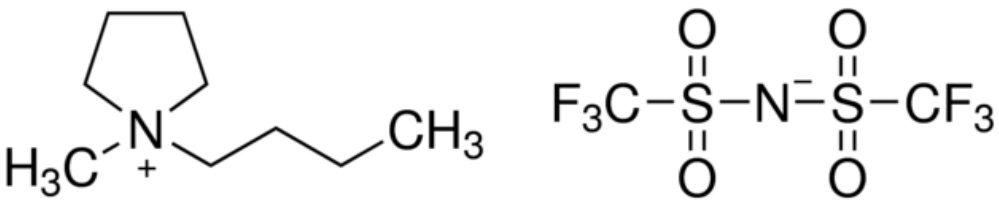

Figure 6-9: N-methyl-N-propylpyrrolidinium bis(trifluoromethanesulfonyl)imide

V. Rinsing of the PYR13TFSI Ionic Liquid

To remove unreacted LiTFSI salt, traces of LiBr and impurities from the ionic liquid (after removal of the upper aqueous phase), PYR13TFSI was rinsed five consecutive times with the same volume of deionized water. This rinsing method allows reducing the Li^{+} concentration in the ionic liquid down to 2 µg.dm^{-3} (2 ppb). The optimum water/ionic liquid volume ratio was fixed to 1/1 for each rinsing step.[136]

6.3.2 Empirical Characterizations of Ionic Liquid

Since as-synthetized ionic liquid was aimed to be used as additive for lithium-sulfur battery, the two following empirical tests were performed to evaluate their ability to wet the separators and limited solubility of PS.

I. Separator wetting test

To compare the ability of PYR13TFSI to wet different separators, Celgard2500 and Whatman disks were exposed to 20 µl of IL. In Figure 6-10.a the complete absorption of the electrolyte by Whatman separator can be seen while the IL drop on the C2500 separator is completely recognizable in Figure 6-10.b.

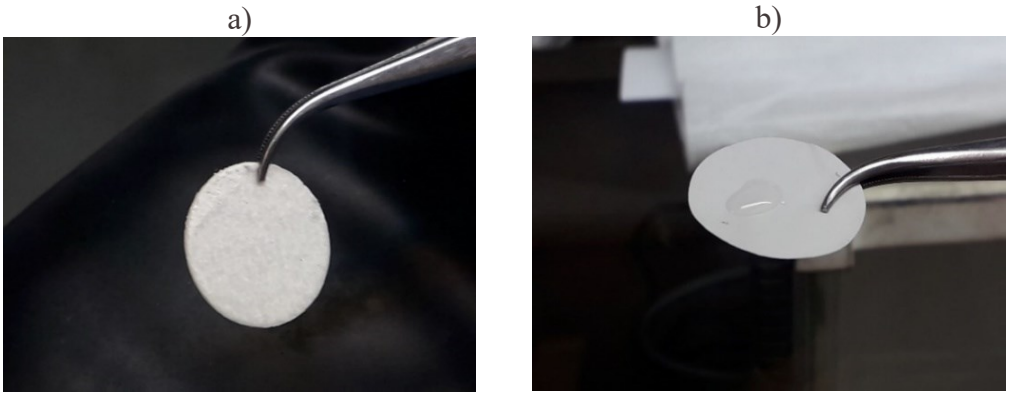

Figure 6-10: Ionic liquid separator wetting a) Fiberglass-Whatman, b)Celgard-C2500

II. Polysulfide in Ionic Liquids electrolytes

To have an idea about the solubility of polysulfide in ionic liquids, a simple test was carried out to verify the effect of density and viscosity of IL on the solubility of PS. The samples were prepared by addition the same volume of Polysulfide solution (2mM Li_2S_x in DME:DIOX-(1:1))to IL(PYR13TFSI). The higher density of ionic liquid causes very slow kinetic of spontaneous diffusion. Figure 6-11 shows the sample in different time lapse. It can be seen that even after 6 hours the diffusion of polysulfide in ionic liquid is not notable. Even in the following day, the two liquids are not fully mixed. However, this simple experiment confirms only the difficulty of the diffusion but not the complex condition of electrolyte during electrochemical reaction.

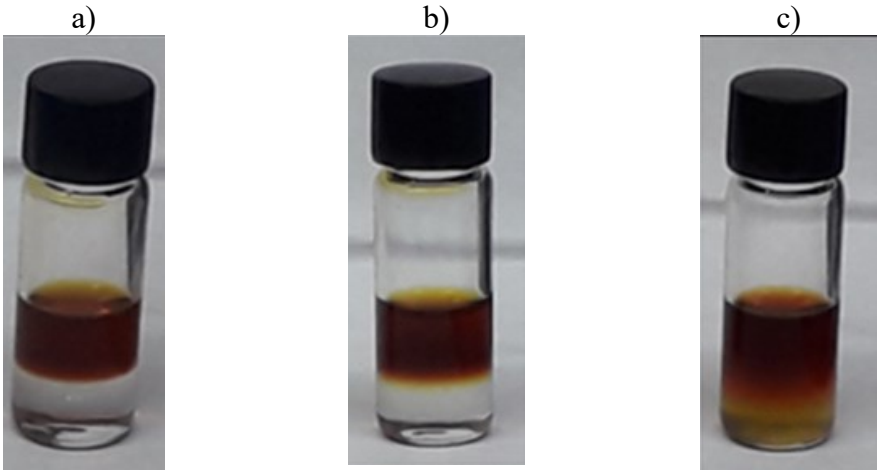

Figure 6-11:Diffusion-Solubility test a)initial, b) after 6 hours, c)after one day

6.3.3 Ionic Liquid; Effect of Celgard2500 and Whatman

The galvanostatic cycling of the cell with ionic liquid electrolyte and Celgard2500 separator (ILC) was performed and the cell was left in discharged state. Figure 6-12 shows the extracted electrolyte from the separator after cycling. The color of extracted solution was almost the same as pure ionic liquid which suggests not solved polysulfide.

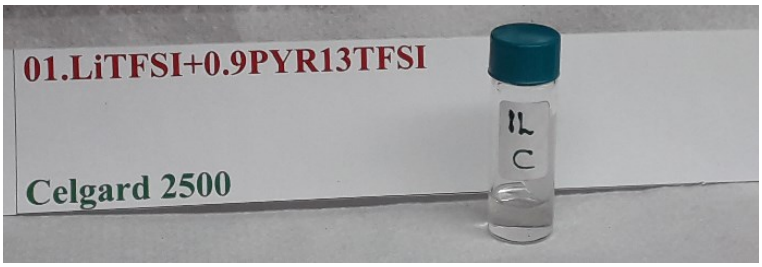

Figure 6-12: Extracted from separator of the cell with IL.C

Figure 6-13.a shows the galvanostatic cycling of a cell with pure ionic liquid and Celgard2500 (ILC). The very low capacity delivered by the cell is due to the lack of wetting of separator by pure ionic liquid. During cell assembly, the ionic liquid drops was remained on the surface of polymer without any sign of wetting. Probably after cell assembly by pressure application, the separator has been partially wetted and demonstrated very low electrochemical activity. The absence of plateaus in voltage profile (Figure 6-13.b) confirms the lack of sulfur reduction.

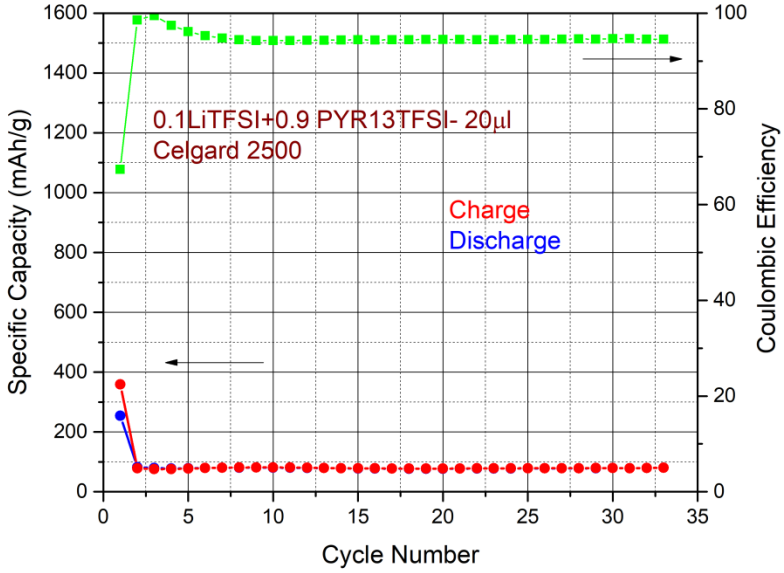

a)

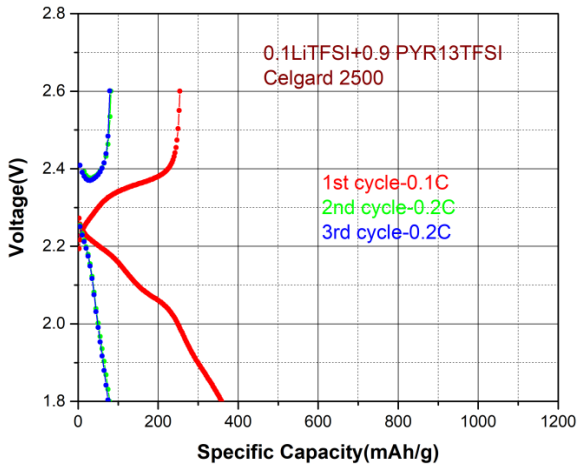

b)

Figure 6-13: a) Galvanostatic cycling and Coulombic efficiencies, b) Charge and discharge capacityof the cell with IL.C

The cell with pure ionic liquid and Whatman separator(ILW) shows a very interesting behavior. In Figure 6-14.a the FESEM images of the surface of lithium disk without any sign of corrosion is visible. Figure 6-14.b depicts the distribution of sulfur components on the anode. The sulfur-based compounds are present in spot and aggregate forms which confirms the low solubility of polysulfides in ionic liquids. However, the yellowish color of solution after extraction from the separator in this case is due to the higher quantity of sulfur present in 80µl electrolyte (for Celgard the quantity was 20µl) used during the assembly of cell with fiberglass separator (Figure 6-14.c).

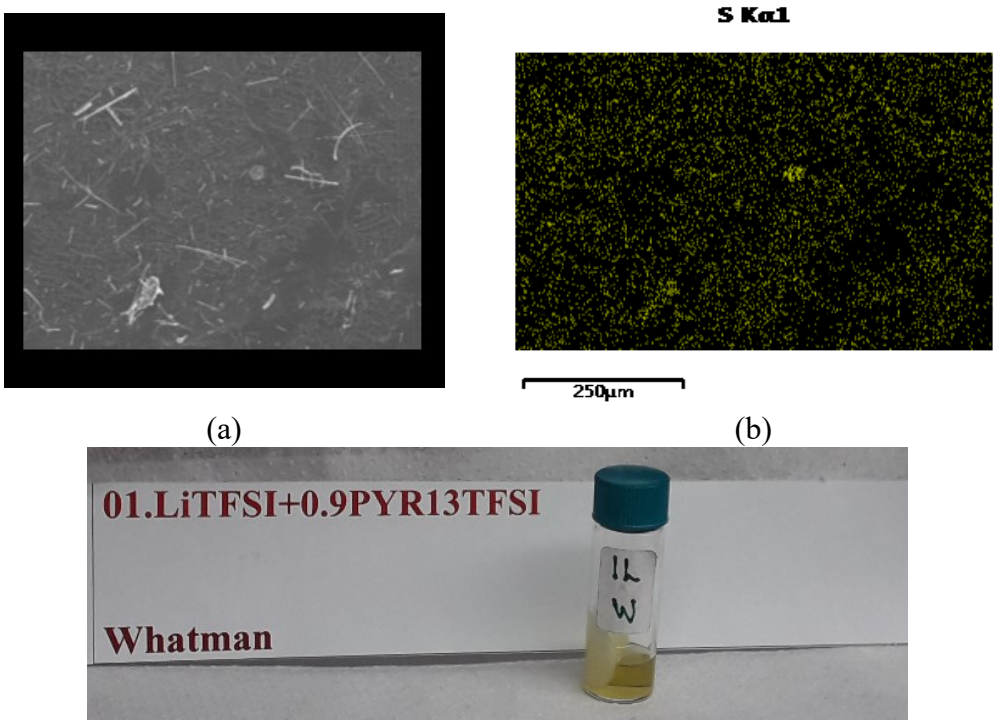

(a) (b)

(c)

Figure 6-14: a) FESEM image of lithium surface, b)sulfur mapping on the surface of lithium,c)extracted polysulfides from separatorthe cell with IL.W

Figure 6-15 depicts the galvanostatic cycling of cell with pure ionic liquid and Whatman separator(ILW). After the first cycle at 0.1C, the capacity fades continuously at current density of 0.2C. This continuous fading is related to the deposition of polysulfide on the cathode and limiting the access of the lithium ions to the fresh sulfur. It seems that the use of pure ionic liquid reduces the sulfur utilization. In Figure 6-15.b, some plateau can be recognized which is related to the low capacity of the cell.

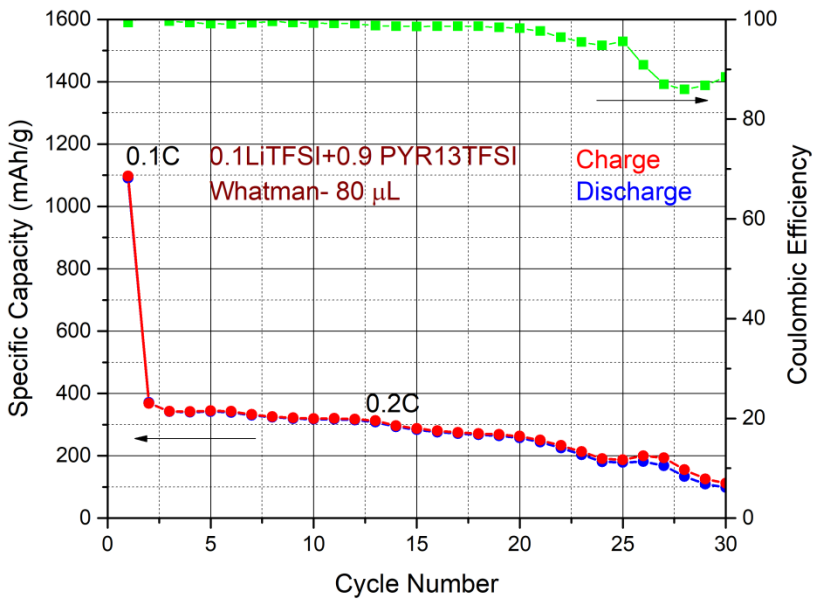

a)

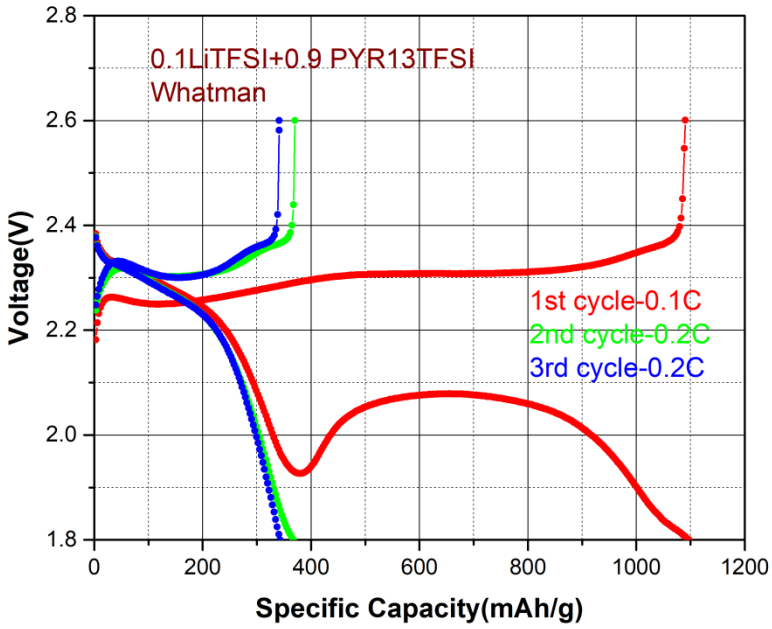

b)

Figure 6-15:a) Galvanostatic cycling and Coulombic efficiencies, b)Charge and discharge capacity of the cell with IL.W

The UV-Vis spectra of polysulfide solutions extracted from separators is reported in Figure 6-16. In the case of Celgard2500(ILC) the intensity of peak is very low as was expected of the color of the solution. In both cases a peak at 282nm is observed which corresponds to S_6^{-2}.[137] The asymmetry of the peak is due to the convolution of two peaks one approximately at 260nm and the other one at 340nm. The second feature of ionic liquid spectra is the absence of peak around 600nm.

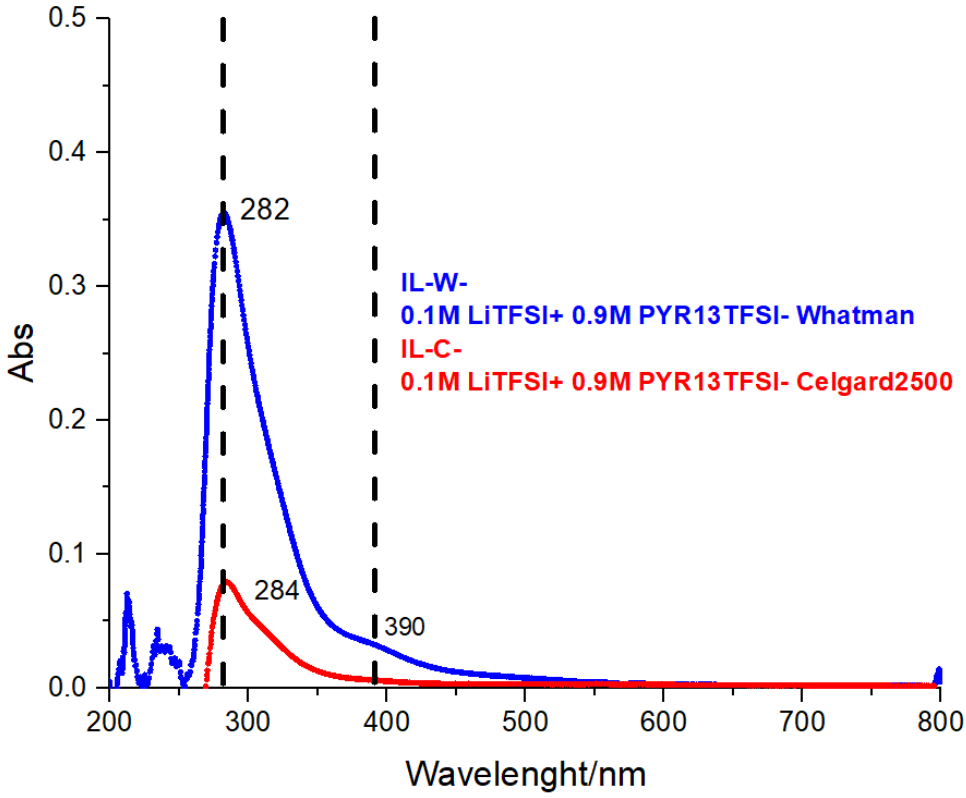

Figure 6-16:UV-Vis spectra of pure Ionic Liquid electrolyte

6.3.4 Ionic Liquids as Additive for Electrolyte

As the cells with pure ionic liquids did not provide an effective capacity, it was decided to use them as an additive for ether-based electrolyte. To this purpose, three electrolytes were prepared by adding different weight percentages of the synthesized ionic liquid PYR13TFSI to the lithium-sulfur standard electrolyte (Table 6-2).

Table 6-2: Composition of electrolytes with Ionic Liquid Additive

STD	DME:DIOX (1:1) + 1M LiTFSI + 0.25M $LiNO_3$
STD+IL10	DME:DIOX (1:1) + 1M LiTFSI + 0.25M $LiNO_3$ + 10% PYR13TFSI
STD+IL20	DME:DIOX (1:1) + 1M LiTFSI + 0.25M $LiNO_3$ + 20% PYR13TFSI
STD+IL50	DME:DIOX (1:1) + 1M LiTFSI + 0.25M $LiNO_3$ + 50% PYR13TFSI

The ionic conductivity of three electrolytes was measured by electrochemical impedance spectroscopy.The symmetric cells were assembled by Steel/Whatman-electrolyte/ Steel architecture in argon-filled glove-box.

Figure 6-17 shows the behavior of three electrolytes in comparison with ether-based standard one. The conductivity for all samples showed an increase with the temperature. The standard electrolyte has demonstrated the highest ionic conductivity followed by STD+IL10. Generally, an increase in the percentage of

the ionic liquid, make the ionic conductivity decrease. This behavior can be related to the high viscosity of the ionic liquids which reduces the ion mobility. It seems that the diminution of the ionic conductivity slows down in the case of additive percentage higher than 20% (Figure 6-17).

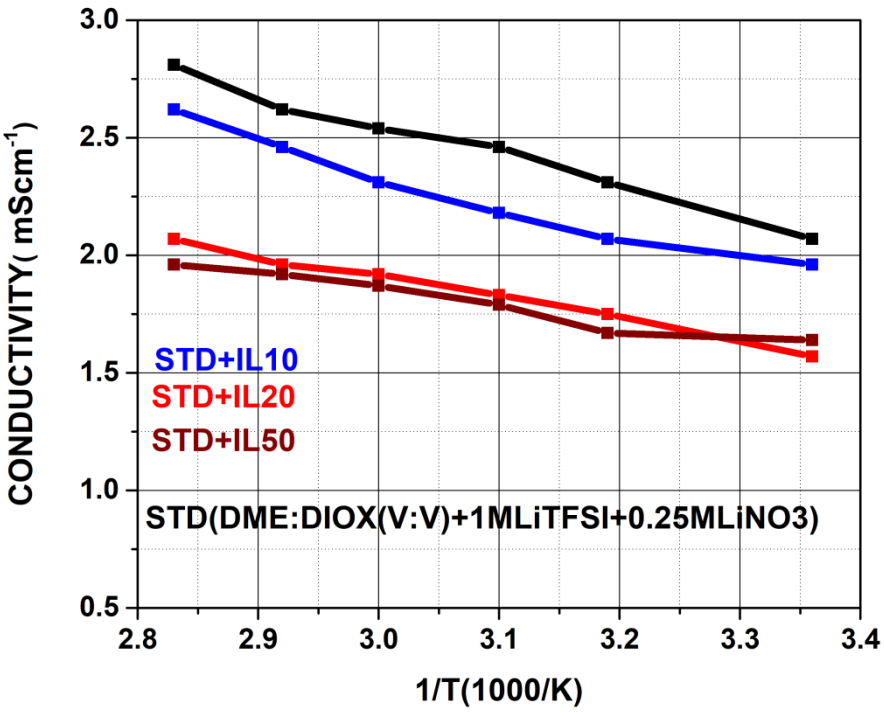

Figure 6-17: Conductivity Arrhenius plot for electrolytes with Ionic Liquid Additive

Figure 6-18 depicts the galvanostatic cycling of the cells with standard electrolyte and three electrolytes with 10,20 and 50% ionic liquid. The cells were cycled at current density 0.1C for the first cycle and 0.2C for the next 50 cycles. The cell with STD+IL20 showed a stable capacity around 600 mAh/g. This stability is due to the controlled polysulfide dissolution in the ionic liquid. The cell with SDT+IL50 delivered a low capacity around 300 mAh/g that can be related to its lower ionic conductivity. The cell with STD+IL10 stands in the middle of observed capacities. In fact, no relation between the specific capacity and ionic conductivity in these three electrolytes was observed.

Due to the higher delivered capacity, the cell with STD+IL20 has been selected for further studies.

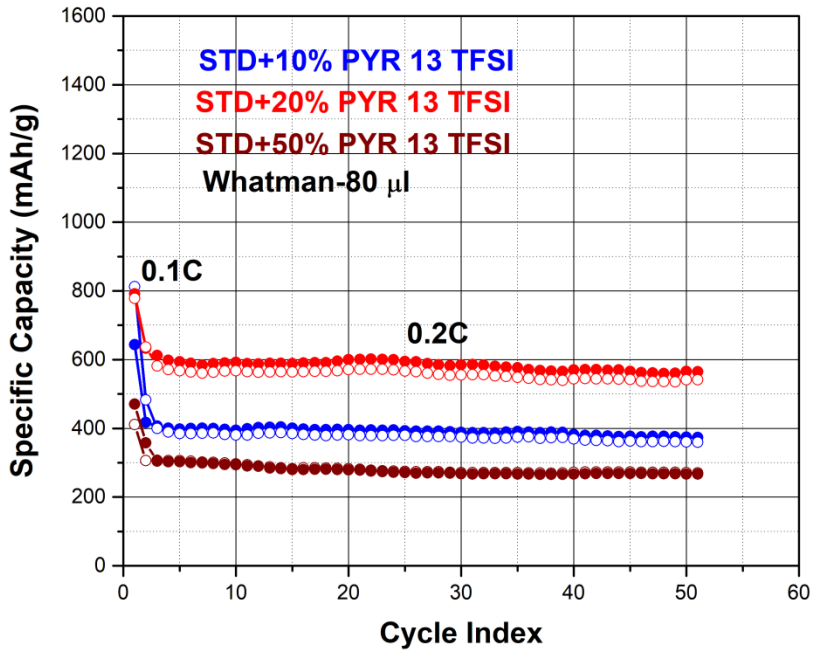

Figure 6-18: Galvanostatic cycling of the cells with ionic liquid additive electrolyte 10, 20, 50%

6.3.5 Standard Electrolyte and Ionic Liquid Additive; Effect of Celgard2500 and Whatman

To investigate the effect of ionic liquid additive on the performance of lithium-sulfur battery, a cell with standard electrolyte and 20% of ionic liquid (PYR13TFSI) and Celgard2500 separator(S.IL.C) was prepared. The galvanostatic cycling was performed and the cell was left in discharged state. The cell was disassembled in argon-field glove-box and the lithium foil was used for FESEM morphology and EDX analysis. Figure 6-19.a depicts the FESEM image of the lithium surface of cell with Celgard2500 separator. In Figure 6-19.b, the homogenously distributed sulfur spots on the lithium surface are visible. This type of distribution could be explained by competition between ether-based electrolyte to diffusion polysulfide and ionic liquid tendency to block them and the resulting accumulation in some points. The separator was immersed in an equivolume mixture of DME:DIOX(1:1) to extract dissolved sulfur and polysulfide in the electrolyte (Figure 6-19.c).

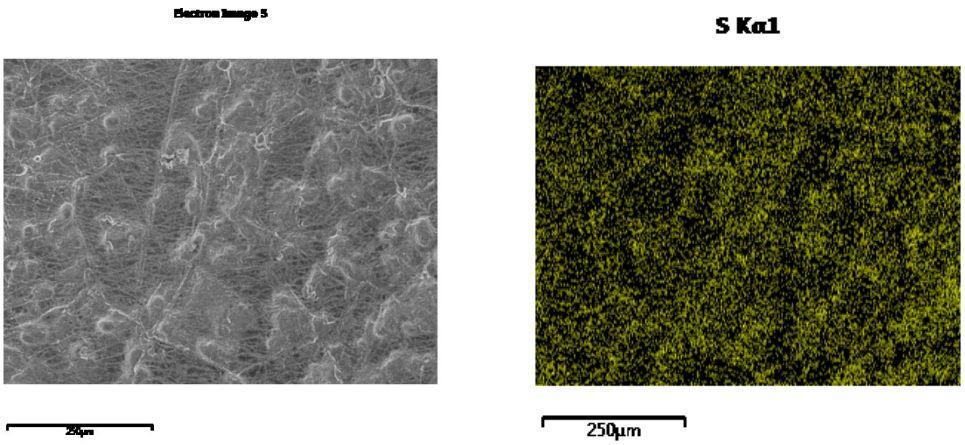

(a) (b)

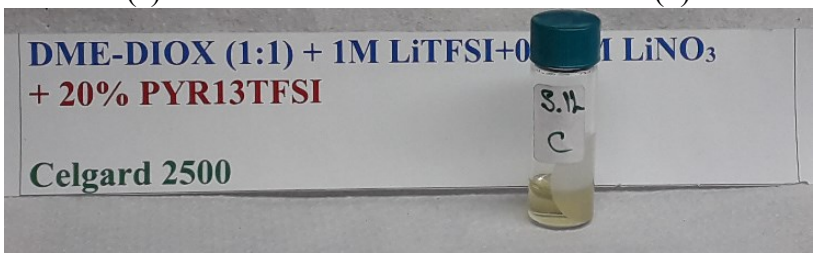

(c)

Figure 6-19: a) FESEM image of lithium surface, b)sulfur mapping on the surface of lithium, c) extracted polysulfides from separator of the cell with STD.IL.C

Figure 6-20.a shows the galvanostatic cycling of the cell with STD+IL20 and Celgard2500. Initially at 0.1C, the cell provides a capacity around 1050 with low coulumbic efficiency. At 0.2 C the capacity continuously fades and after 30 cycles reaches to around 500 mAh/g. Figure 6-20.b shows the charge-discharge capacity at different cycles. In none of cycles, the higher reduction potential plateau was not observed. In the initial cycles, the second reduction potential were observed which are responsible of the cell capacity. In the further cycles, the reduction of capacity may be related to the increase of the viscosity of electrolyte.

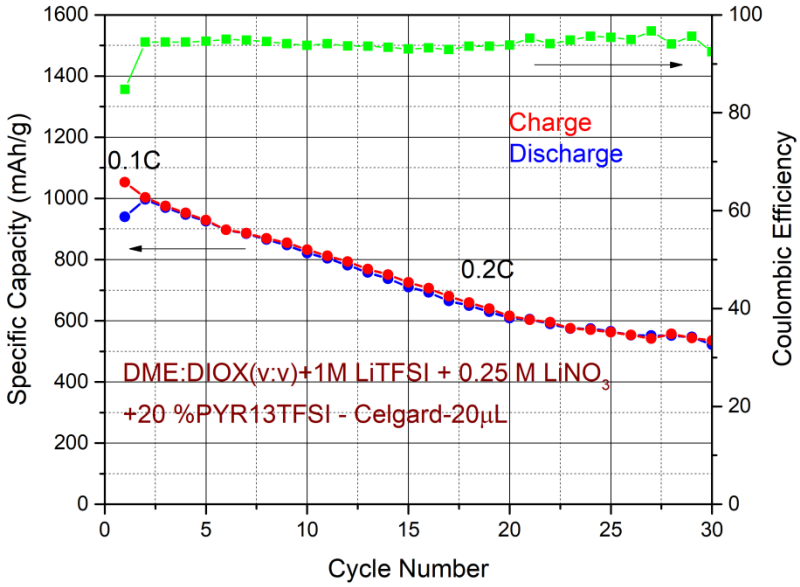

a)

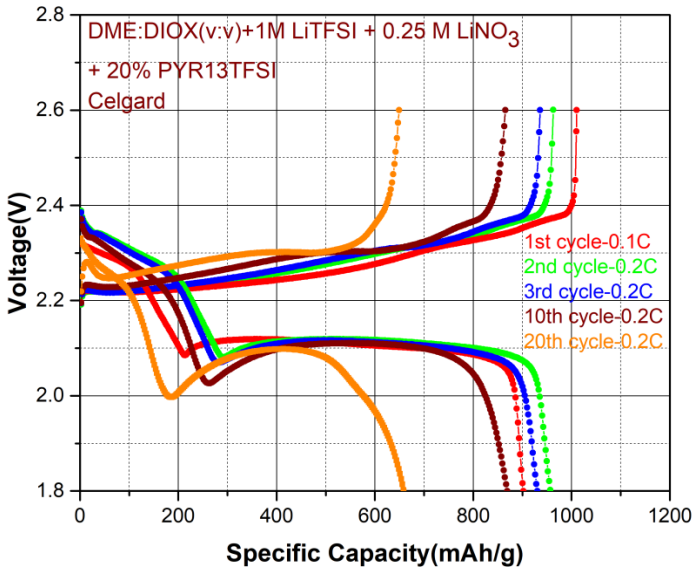

b)

Figure 6-20: a) Galvanostatic cycling and Coulombic efficiencies, b) Charge and discharge capacity of the cell with STD.IL.C

To compare the effect of separator (higher quantity of electrolyte), a cell with standard electrolyte and 20% of ionic liquid (PYR13TFSI) and Whatman separator(S.IL.W) was prepared. Galvanostatic cycling was performed and the cell was left in discharged state. The cell was disassembled in argon-field glove-box and the lithium foil was used for FESEM morphology and EDX analysis. Figure 6-21.ademonstrate the surface of the lithium disk in the cells with STD+IL20 and Whatman separator. InFigure 6-21.b, the spots of sulfur are evident. This indicates the tendency of ionic liquid to accumulate sulfur in the spots. The presence of accumulated points may explain clear color of extracted solvent from separator.The

separator was immersed in an equivolume mixture of DME:DIOX(1:1) to extract dissolved sulfur and polysulfide in the electrolyte (Figure 6-21.c).

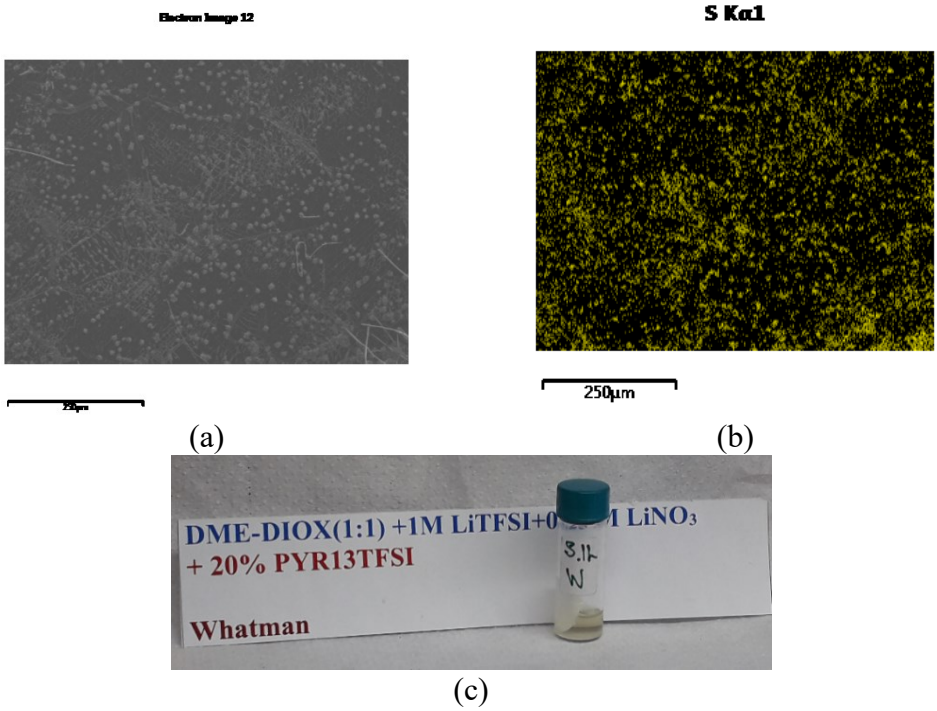

Figure 6-21: a) FESEM image of lithium surface, b)sulfur mapping on the surface of lithium, c) extracted polysulfides from separator of the cell with STD.IL.W

Figure 6-22.a presents the galvanostatic cycling of the cell with STD+IL20 and Whatman separator. After the first cycle at 0.1C, the cell provides initially a specific capacity around970 mAh/g which lost 12% of its capacity after 80 cycles. Figure 6-22.b shows the charge-discharge capacity at different cycles. It can be seen that the type of separator (quantity of electrolyte) can affect the stability of cycles. The cell with Whatman separator provides less initial capacity but the capacity lose after 80 cycles is much less than the cell with Celgard2500.

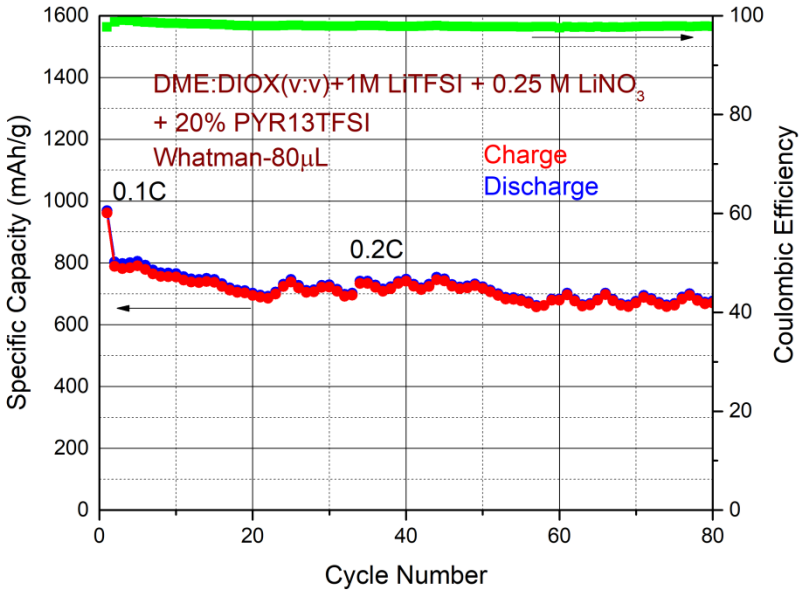

a)

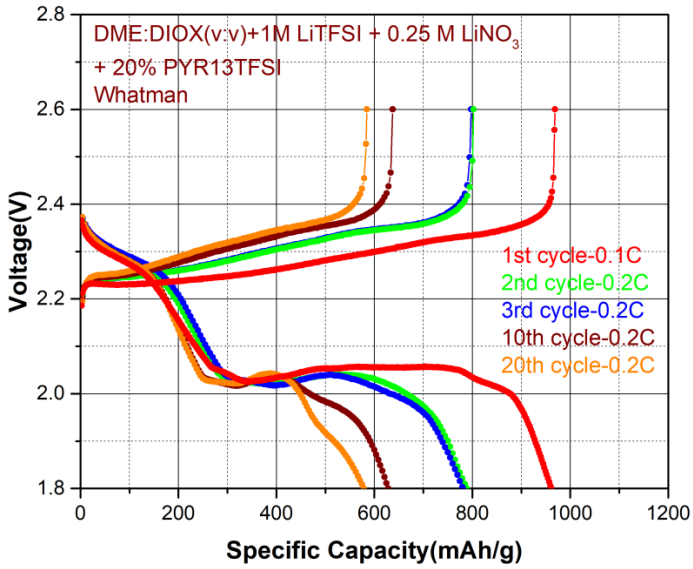

b)

Figure 6-22: a) Galvanostatic cycling and Coulombic efficiencies, b) Charge and discharge capacityof the cell with STD.IL.W

UV-Vis spectra of the hybrid electrolyte is presented in Figure 6-23. The intensity of peaks in the case of Celgard2500 is less than Whatman. The combined effect of standard electrolyte and ionic liquid can be seen in this spectra. Two peaks at 260 and 340nm are closer together and some signal at 610nm can be seen.[137] The overlapped peak at 420nm is related to S_4^{-2}.[131]

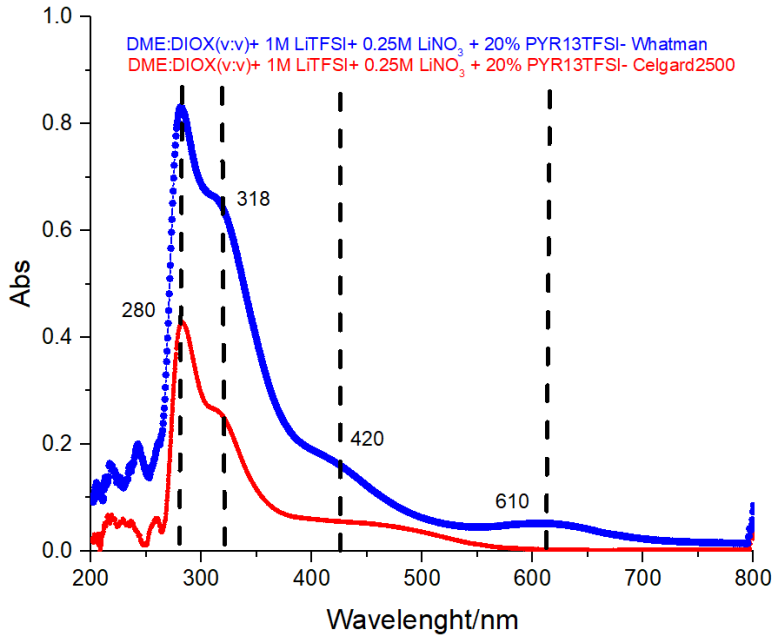

Figure 6-23: UV-Vis spectra of the hybrid electrolyte

6.3.6 Standard Electrolyte and Ionic Liquid Additive; Effect of Celgard2500 and Whatman

The results obtained in previous section, confirm that each separator differently affect the initial capacity and capacity stability after long cycling. To take advantages of the different characteristics of the separators, a cell with use of STD+IL20 electrolyte and the both Whatman and Celgard2500separators was prepared.

The galvanostatic cycling was performed and the cells were left at discharged state. Then the cells were disassembled and the lithium foils were used for FESEM morphology and EDX analysis.

Figure 6-24.a FESEM images shows the aggregation spots on the surface of the lithium. Figure 6-24Figure 6-24.b confirms the accumulation of the sulfur-based materials in these spots. It seems that the use of two separators can limit the distribution of the polysulfide products. Figure 6-24.c shows the clear extracted solution from Celgard2500 separator which was used in the cell.

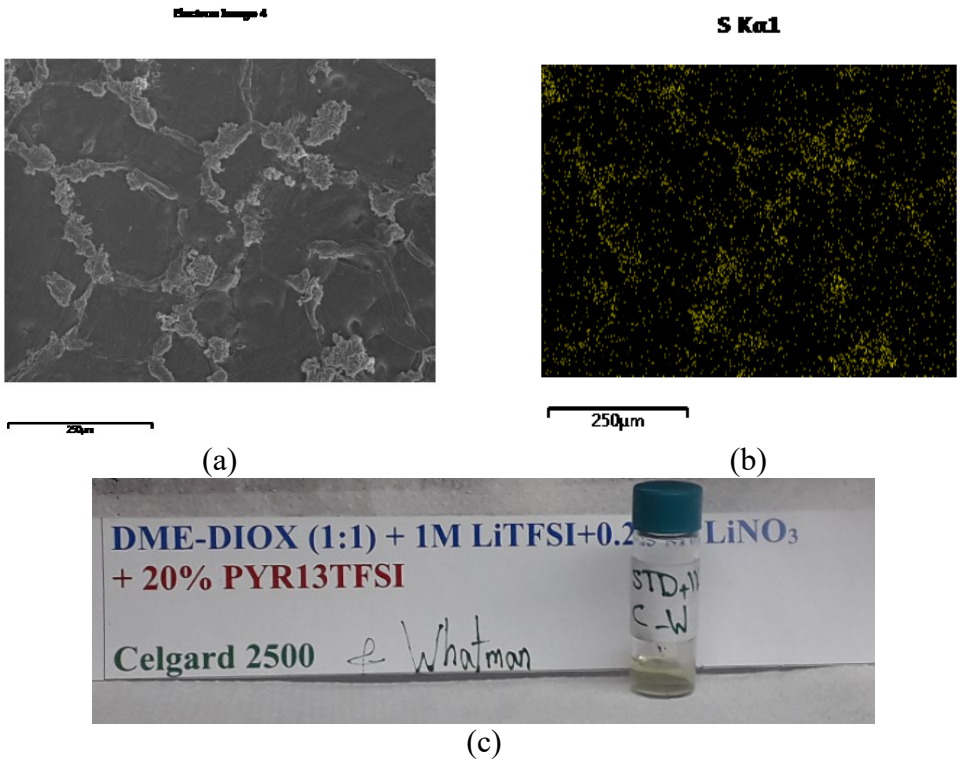

Figure 6-24: a) FESEM image of lithium surface, b)sulfur mapping on the surface of lithium, c) extracted polysulfides from separator of the cell with STD.IL.C.W

Figure 6-25.a shows the galvanostatic cycling of the cell with STD+IL20withthe both separators. The cell demonstrated a specific capacity around 1100mAh/g at 0.1C and for100 cycle at 0.2C it remained more than 800mAh/g. Figure 6-25.b depicts the charge-discharge capacity of the cell with hybrid electrolyte and double separators. The synergetic effect of the separators provides stable cycling with high coulumbic efficiency. No anomalous behavior in the voltage profile was observed. The higher capacity provided by the cell is related to the low value of the first discharge potential (2.35V) and the extension of the second discharge potential plateau (2.05V). The two separators appear to have a synergetic role one enhancing the capacity(Celgard2500) and the other one stabilizing the cycling(Whatman).

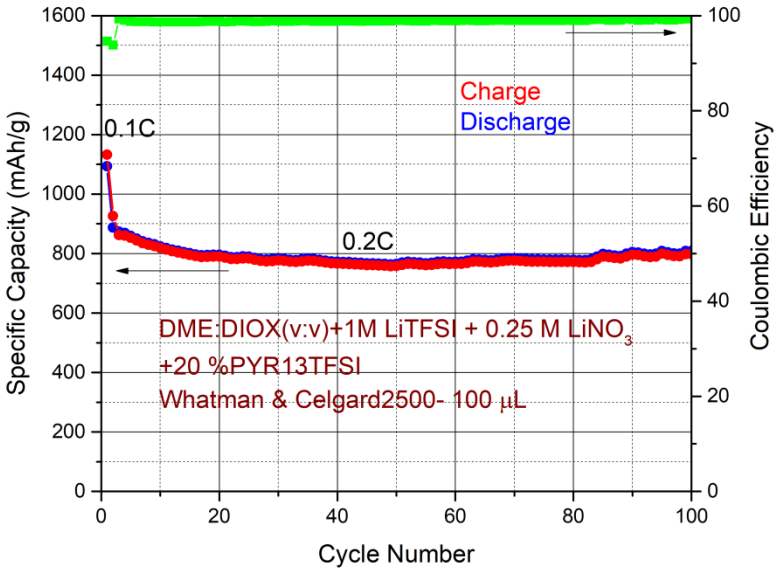

a)

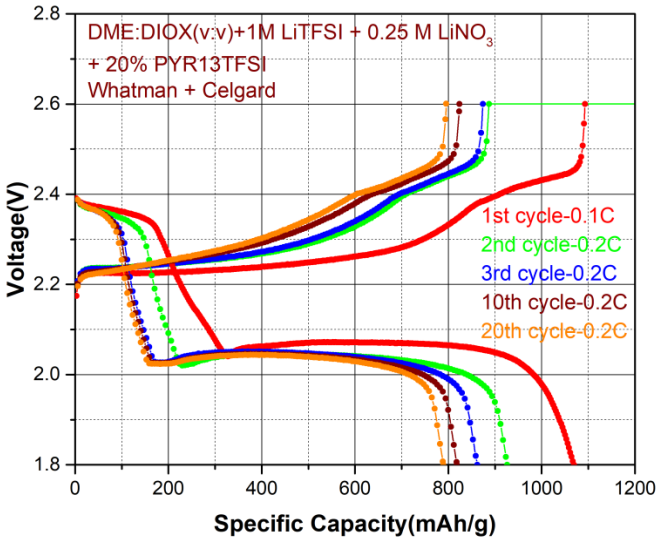

b)

Figure 6-25: a) Galvanostatic cycling and Coulombic efficiencies, b) Charge and discharge capacity of the cell with STD.IL.C.W

Chapter 7 Silicon-Sulfur Full Cell

As mentioned in chapter 2, the anode modification is one of the strategies to reduce the effect of shuttle phenomena in lithium-sulfur batteries. The silicon anode prepared in chapter 4 and the sulfur cathode in chapter 5 were assembled in a full Silicon-Sulfur cell. For the full Si-S cell preparation, the silicon must be lithiated before use as anode. To have a compatible lithium salt and electrolyte, the pre-lithiation and galvanostatic cycling were performed with lithium-silicon standard electrolyte.

The pre-lithiation of silicon anode was performed by assembling Li/Whatman/Si@CNS half-cell in EL-CELL using (DME:DIOX(v:v) + 1M LiTFSI + 0.25M $LiNO_3$) as electrolyte. The cell was cycled at a current density of 0.1C in the voltage range of 0.01-2 V, repeating the cycles to assure a sufficient quantity of lithium inserted in the Si@CNS electrode. Then, the cell was disassembled and the lithiated electrode was washed with DME/DIOX and dried in argon-filled glove-box. Full cell was assembled in CR2032 coin cell with the previously lithiated Si@CNS, the S@HC-CNS Sulfur cathode and Whatman separators using DME:DIOX (1:1) + 1M LiTFSI + 0.25 M $LiNO_3$ as electrolyte. The galvanostatic cycling was performed in the voltage range of 1.5-3 V at current density 0.1C for the first cycle and 0.2C for the next cycles. For this preliminary cell no electrode capacity balancing has been made.

Figure 7-1.a shows that the cell worked as it was expected giving a sufficient specific capacity for the first 5 cycles. The charge steps in all cycles show that Li^+ moving towards the anode in a quantity higher than that of the corresponding discharging. Such partial irreversibility draws to Li^+ ions consumption rapidly to the almost the complete depletion of Li in the Si anode.

Figure 7-1.b shows the voltage profiles of the first three cycles. The trend of the curves indicates the behavior as expected for sulfur system with the recharge step more extended than the discharge one. The potential values of the various stepsare lower than those of a conventional Li-S cell due to the presence of the silicon anode instead of the lithium metal. These findings indicate a promising system though still needs a long experimental work.

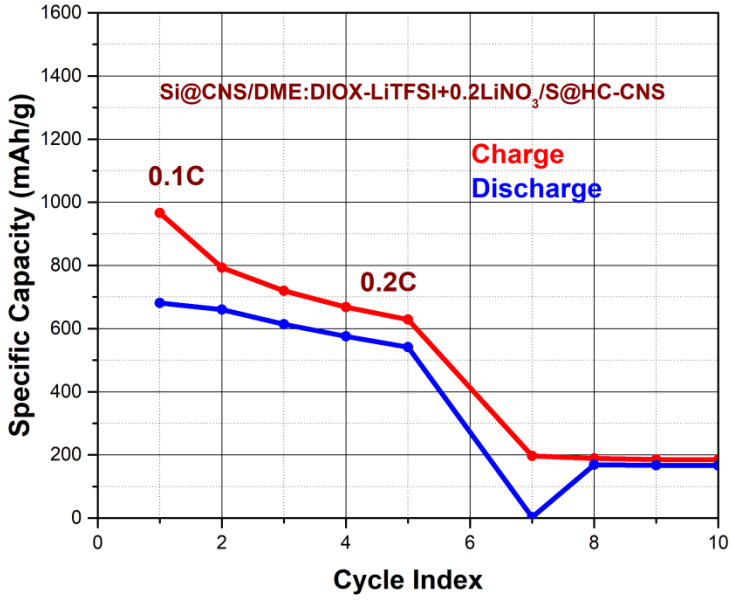

a)

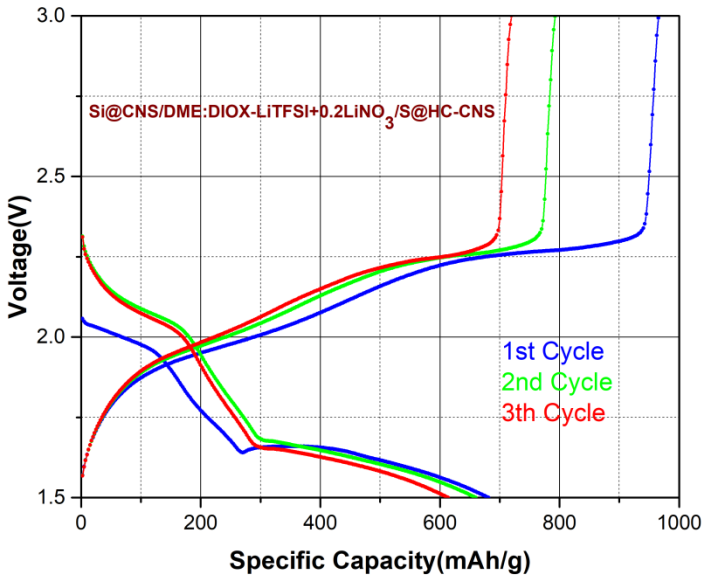

b)

Figure 7-1: a) Galvanostatic cycling b) Charge and discharge capacity of the full cell Si@CNS/ DME:DIOX (1:1) + 1M LiTFSI + 0.25 M LiNO3 /S@HC-CNS

Chapter 8 Conclusion and Prospects

In this work, an innovative application of cyclodextrin-based nanosponges (NS) as eco-friendly and low cost material for application in energy storage field is introduced. Cyclodextrins are cyclic oligosaccharides composed of glucopyranose units linked through α-1,4 glycosidic bonds which are produced from starch by enzymatic conversion. Nanosponges are polymerized cyclodextrin by different cross-linkers. Figure 8-1 depicts the extended field of the application of this innovative material inside the Li-ion and Post Li-ion systems

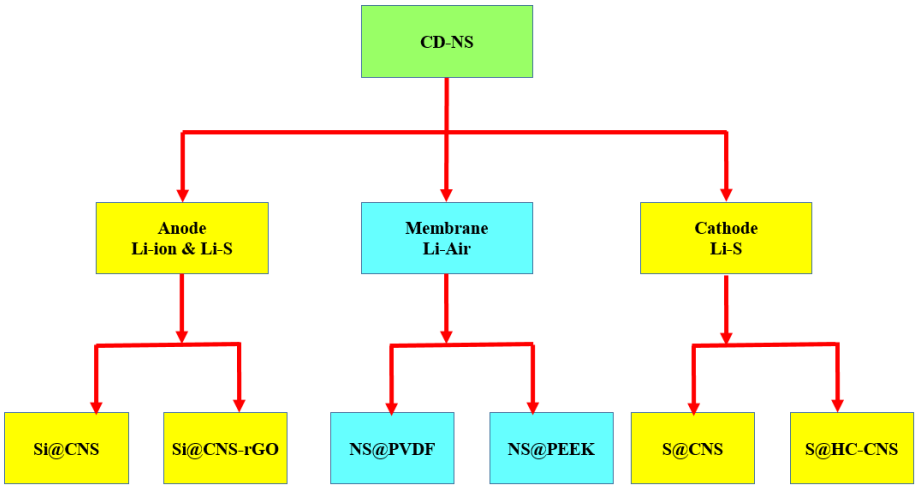

Figure 8-1: Application of nanosponges for energy storage

- In Lithium-Air batteries nanosponges were applied to overcome two problems. The conventional synthesis of NS shows very interesting results for application as Oxygen-selective membrane. The CITR-NS@PVdF membrane demonstrates high oxygen selectivity which increased more than six times respect to PVdF and very low water permeability that is reduced almost 98%. The same nanosponge in PEEK polymer matrix (NS@PWC) with oxygen blocking property was used as lithium-protection membrane.
- A lithium-alternative anode was prepared with embedding of silicon nanoparticles in NS. The pyrolysis of Si@NS provides different silicon mass-loading active materials. A passivated silicon with controlled 3% oxide layer creates an intimate contact with nanosponges which buffers the volume change of silicon during cycling. To increase the electric conductivity, the later was wrapped with the reduced graphene oxide. The final anode (Si3@CNS-rGO) provides a stable capacity 1500 mAh/g over 50 cycles. The modified electrode fabrication method and the use of Sodium Alginate binder resulted in preparation electrodes having excellent mechanical properties with a reproducible electrochemical performance.

The substitution of the standard electrolyte (EC:DMC (v:v) +1MLiPF6 + 1% VC) with modified electrolyte (EC:DMC (v:v) + LiTFSI + 1% FEC) increased 40% the specific capacity of the cell.

- In lithium-sulfur batteries, hierarchical carbon (HC-CNS) prepared by pyrolysis of PMDA-NS was applied as conductive matrix for lithium-sulfur cathode. In HC-CNS, mesopores function as electrolyte reservoir and micropores are supposed to be electrochemical reaction's sites. This carbon has possibility to host three times its mass elemental sulfur.
- Electrolyte for lithium-sulfur battery was another subject which is discussed in this thesis. Pyrrolidinium-based ionic liquids were synthesized through solvent-free method and used as additive in organic solvent electrolyte. The electrolyte with 20% ionic liquid demonstrates highest capacity while the 10% additive showed a better ionic conductivity. The low lithium polysulfide solubility of ionic liquids, enhanced the specific capacity and coulumbic efficiency of lithium-sulfur cells. The incompatibility of polymeric separator with ionic liquid was an issue that tackled by the use of fiberglass separator. The best result in terms of capacity and stability was obtained with the use of standard electrolyte and 20% ionic liquid (STD+20%IL) with the both of separators.
- A full sulfur cell with silicon-based anode and sulfur cathode synthetized by nanosponge-based material was prepared. The pre-lithiation of anode was performed in EL-cell and the configuration Si@CNS/DME:DIOX (1:1) + 1M LiTFSI + 0.25 M $LiNO_3$/S@HC-CNS was used for CR2032 coin cell assembly. The preliminary results showed that pre-lithiation of silicon has crucial effect on the performance of the cell. Moreover, the charge and discharge capacity of Silicon-Sulfur confirms the same behavior of silicon and lithium in sulfur systems.

References:

1. Worldbank. blogs.worldbank.org/developmenttalk/the-global-energy-challenge.
2. UN UN. Convention on Climate Change: Climate Agreement of Paris. 2015:1-27. doi:10.1017/s0020782900004253
3. Klessmann C, Held A, Rathmann M, Ragwitz M. Status and perspectives of renewable energy policy and deployment in the European Union—What is needed to reach the 2020 targets? *Energy Policy*. 2011;39(12):7637-7657. doi:10.1016/j.enpol.2011.08.038
4. DOE. https://www.energy.gov/oe/activities/technology-development/energy-storage.
5. Luo X, Wang J, Dooner M, Clarke J. Overview of current development in electrical energy storage technologies and the application potential in power system operation. *Appl Energy*. 2015;137:511-536. doi:10.1016/j.apenergy.2014.09.081
6. Chen H, Cong TN, Yang W, Tan C, Li Y, Ding Y. Progress in electrical energy storage system: A critical review. *Prog Nat Sci*. 2009;19(3):291-312. doi:10.1016/j.pnsc.2008.07.014
7. Patel K. Lithium-Sulfur Battery: Chemistry, Challenges, Cost, and Future. *J Undergrad Res Univ Illinois Chicago*. 2016;9(2). doi:10.5210/jur.v9i2.7553
8. World Economic Forum. https://www.weforum.org/agenda/2017/09/countries-are-announcing-plans-to-phase-out-petrol-and-diesel-cars-is-yours-on-the-list/.
9. EEA. https://www.eea.europa.eu/data-and-maps/indicators/transport-emissions-of-greenhouse-gases/transport-emissions-of-greenhouse-gases-11.
10. Transport emissions. https://ec.europa.eu/clima/policies/transport_en.
11. Mayer R. Elemental Sulfur and its Reactions. In: *Organic Chemistry of Sulfur*. Boston, MA: Springer US; 1977:33-69. doi:10.1007/978-1-4684-2049-4_2
12. Laura Crapanzano. Polymorphism of sulfur: Structural and Dynamical Aspects.
13. Borchardt L, Oschatz M, Kaskel S. Carbon Materials for Lithium Sulfur Batteries-Ten Critical Questions. *Chem - A Eur J*. 2016;22(22):7324-7351. doi:10.1002/chem.201600040
14. Zhang SS. Liquid electrolyte lithium/sulfur battery: Fundamental chemistry, problems, and solutions. *J Power Sources*. 2013;231:153-162. doi:10.1016/j.jpowsour.2012.12.102
15. Song J, Gordin ML, Xu T, et al. Strong lithium polysulfide chemisorption on electroactive sites of nitrogen-doped carbon composites for high-performance lithium-sulfur battery cathodes. *Angew Chemie - Int Ed*. 2015;54(14):4325-4329. doi:10.1002/anie.201411109
16. Yamin H. Lithium Sulfur Battery. *J Electrochem Soc*. 1988;135(5):1045. doi:10.1149/1.2095868
17. Dominko R, Demir-Cakan R, Morcrette M, Tarascon J-M. Analytical detection of soluble polysulphides in a modified Swagelok cell. *Electrochem commun*. 2011;13(2):117-120. doi:10.1016/j.elecom.2010.11.029
18. Ren Y, Shui H, Peng C, Liu H, Hu Y. Solubility of elemental sulfur in pure organic solvents and organic solvent–ionic liquid mixtures from 293.15 to

353.15K. *Fluid Phase Equilib*. 2011;312:31-36. doi:10.1016/j.fluid.2011.09.012
19. Yang H, Guo C, Naveed A, et al. Recent progress and perspective on lithium metal anode protection. *Energy Storage Mater*. 2018;14:199-221. doi:10.1016/j.ensm.2018.03.001
20. The electrolytic growth of dendrites from ionic solutions. *Proc R Soc London Ser A Math Phys Sci*. 1962;268(1335):485-505. doi:10.1098/rspa.1962.0154
21. Dornbusch DA, Hilton R, Lohman SD, Suppes GJ. Experimental Validation of the Elimination of Dendrite Short-Circuit Failure in Secondary Lithium-Metal Convection Cell Batteries. *J Electrochem Soc*. 2015;162(3):A262-A268. doi:10.1149/2.0021503jes
22. Deep Resource-https://deepresource.wordpress.com/2017/08/28/efficiency-breakthrough-lithium-ion-batteries/.
23. Zhang R, Li N-W, Cheng X-B, Yin Y-X, Zhang Q, Guo Y-G. Advanced Micro/Nanostructures for Lithium Metal Anodes. *Adv Sci*. 2017;4(3):1600445. doi:10.1002/advs.201600445
24. Kganyago KR, Ngoepe PE. Structural and electronic properties of lithium intercalated graphite. *Phys Rev B*. 2003;68(20):205111. doi:10.1103/PhysRevB.68.205111
25. Zhao H, Deng N, Yan J, et al. A review on anode for lithium-sulfur batteries: Progress and prospects. *Chem Eng J*. 2018;347(January):343-365. doi:10.1016/j.cej.2018.04.112
26. Zhang WJ. A review of the electrochemical performance of alloy anodes for lithium-ion batteries. *J Power Sources*. 2011;196(1):13-24. doi:10.1016/j.jpowsour.2010.07.020
27. Wachtler, Mario; Winter, Martin; Besenhard J. Anodic materials for rechargeable Li-batteries.
28. Ulus A, Rosenberg Y, Burstein L, Peled E. Tin Alloy-Graphite Composite Anode for Lithium-Ion Batteries. *J Electrochem Soc*. 2002;149(5):A635. doi:10.1149/1.1469029
29. Kubota Y, Escaño MCS, Nakanishi H, Kasai H. Crystal and electronic structure of Li15Si4. *J Appl Phys*. 2007;102(5):053704. doi:10.1063/1.2775999
30. *New Trends in Intercalation Compounds for Energy Storage and Conversion*.
31. Schuppler S, Friedman SL, Marcus MA, et al. Size, shape, and composition of luminescent species in oxidized Si nanocrystals and H-passivated porous Si. *Phys Rev B*. 1995;52(7):4910-4925. doi:10.1103/PhysRevB.52.4910
32. Beattie SD, Loveridge MJ, Lain MJ, et al. Understanding capacity fade in silicon based electrodes for lithium-ion batteries using three electrode cells and upper cut-off voltage studies. *J Power Sources*. 2016;302:426-430. doi:10.1016/j.jpowsour.2015.10.066
33. Obrovac MN, Krause LJ. Reversible Cycling of Crystalline Silicon Powder. *J Electrochem Soc*. 2007;154(2):A103. doi:10.1149/1.2402112
34. Huggins RA. Lithium alloy negative electrodes. *J Power Sources*. 1999;81-82:13-19. doi:10.1016/S0378-7753(99)00124-X
35. Ashuri M, He Q, Shaw LL. Silicon as a potential anode material for Li-ion batteries: Where size, geometry and structure matter. *Nanoscale*. 2016;8(1):74-103. doi:10.1039/c5nr05116a
36. Liu XH, Wang JW, Huang S, et al. In situ atomic-scale imaging of electrochemical lithiation in silicon. *Nat Nanotechnol*. 2012;7(11):749-756.

doi:10.1038/nnano.2012.170
37. McDowell MT, Lee SW, Nix WD, Cui Y. 25th anniversary article: Understanding the lithiation of silicon and other alloying anodes for lithium-ion batteries. *Adv Mater*. 2013;25(36):4966-4985. doi:10.1002/adma.201301795
38. Wang D, Gao M, Pan H, Wang J, Liu Y. High performance amorphous-Si@SiOx/C composite anode materials for Li-ion batteries derived from ball-milling and in situ carbonization. *J Power Sources*. 2014;256:190-199. doi:10.1016/j.jpowsour.2013.12.128
39. Tao H-C, Fan L-Z, Qu X. Facile synthesis of ordered porous Si@C nanorods as anode materials for Li-ion batteries. *Electrochim Acta*. 2012;71:194-200. doi:10.1016/j.electacta.2012.03.139
40. Zhang T, Fu L, Gao J, Yang L, Wu Y, Wu H. Core-shell Si/C nanocomposite as anode material for lithium ion batteries. *Pure Appl Chem*. 2006;78(10):1889-1896. doi:10.1351/pac200678101889
41. Chen D, Mei X, Ji G, et al. Reversible Lithium-Ion Storage in Silver-Treated Nanoscale Hollow Porous Silicon Particles. *Angew Chemie Int Ed*. 2012;51(10):2409-2413. doi:10.1002/anie.201107885
42. Zhou X, Tang J, Yang J, Xie J, Ma L. Silicon@carbon hollow core–shell heterostructures novel anode materials for lithium ion batteries. *Electrochim Acta*. 2013;87:663-668. doi:10.1016/j.electacta.2012.10.008
43. Ashuri M, He Q, Shaw LL. Silicon as a potential anode material for Li-ion batteries: where size, geometry and structure matter. *Nanoscale*. 2016;8(1):74-103. doi:10.1039/C5NR05116A
44. Chan CK, Peng H, Liu G, et al. High-performance lithium battery anodes using silicon nanowires. *Nat Nanotechnol*. 2008;3(1):31-35. doi:10.1038/nnano.2007.411
45. Liu N, Huo K, McDowell MT, Zhao J, Cui Y. Rice husks as a sustainable source of nanostructured silicon for high performance Li-ion battery anodes. *Sci Rep*. 2013;3(1):1919. doi:10.1038/srep01919
46. Wang JG, Xie K, Wei B. Advanced engineering of nanostructured carbons for lithium-sulfur batteries. *Nano Energy*. 2015;15:413-444. doi:10.1016/j.nanoen.2015.05.006
47. Zhang B, Qin X, Li GR, Gao XP. Enhancement of long stability of sulfur cathode by encapsulating sulfur into micropores of carbon spheres. *Energy Environ Sci*. 2010;3(10):1531. doi:10.1039/c002639e
48. Ji X, Lee KT, Nazar LF. A highly ordered nanostructured carbon–sulphur cathode for lithium–sulphur batteries. *Nat Mater*. 2009;8(6):500-506. doi:10.1038/nmat2460
49. Wei Seh Z, Li W, Cha JJ, et al. Sulphur–TiO2 yolk–shell nanoarchitecture with internal void space for long-cycle lithium–sulphur batteries. *Nat Commun*. 2013;4:1331. doi:10.1038/ncomms2327
50. Ding B, Shen L, Xu G, Nie P, Zhang X. Encapsulating sulfur into mesoporous TiO2host as a high performance cathode for lithium-sulfur battery. *Electrochim Acta*. 2013;107:78-84. doi:10.1016/j.electacta.2013.06.009
51. Zhang Z, Li Q, Zhang K, Chen W, Lai Y, Li J. Titanium-dioxide-grafted carbon paper with immobilized sulfur as a flexible free-standing cathode for superior lithium-sulfur batteries. *J Power Sources*. 2015;290:159-167. doi:10.1016/j.jpowsour.2015.05.010
52. Sun Y-Z, Huang J-Q, Zhao C-Z, Zhang Q. A review of solid electrolytes for

safe lithium-sulfur batteries. *Sci China Chem*. 2017;60(12):1508-1526. doi:10.1007/s11426-017-9164-2
53. Scheers J, Fantini S, Johansson P. A review of electrolytes for lithium-sulphur batteries. *J Power Sources*. 2014;255:204-218. doi:10.1016/j.jpowsour.2014.01.023
54. Judez X, Zhang H, Li C, et al. Review—Solid Electrolytes for Safe and High Energy Density Lithium-Sulfur Batteries: Promises and Challenges. *J Electrochem Soc*. 2018;165(1):A6008-A6016. doi:10.1149/2.0041801jes
55. Fulfer KD, Kuroda DG. Solvation Structure and Dynamics of the Lithium Ion in Organic Carbonate-Based Electrolytes: A Time-Dependent Infrared Spectroscopy Study. *J Phys Chem C*. 2016;120(42):24011-24022. doi:10.1021/acs.jpcc.6b08607
56. Bhatt MD, Cho M, Cho K. Conduction of Li+ cations in ethylene carbonate (EC) and propylene carbonate (PC): comparative studies using density functional theory. *J Solid State Electrochem*. 2012;16(2):435-441. doi:10.1007/s10008-011-1350-7
57. Park M, Zhang X, Chung M, Less GB, Sastry AM. A review of conduction phenomena in Li-ion batteries. *J Power Sources*. 2010;195(24):7904-7929. doi:10.1016/j.jpowsour.2010.06.060
58. Southall J. Ionic conductivity and viscosity correlations in liquid electrolytes for incorporation into PVDF gel electrolytes. *Solid State Ionics*. 1996;85(1-4):51-60. doi:10.1016/0167-2738(96)00040-9
59. *Phase Transformations in Metals and Alloys*.
60. Xu K, Angell CA. Sulfone-Based Electrolytes for Lithium-Ion Batteries. *J Electrochem Soc*. 2002;149(7):A920. doi:10.1149/1.1483866
61. Eshetu GG, Bertrand J-P, Lecocq A, et al. Fire behavior of carbonates-based electrolytes used in Li-ion rechargeable batteries with a focus on the role of the LiPF 6 and LiFSI salts. *J Power Sources*. 2014;269:804-811. doi:10.1016/j.jpowsour.2014.07.065
62. Skarmoutsos I, Ponnuchamy V, Vetere V, Mossa S. Li + Solvation in Pure, Binary, and Ternary Mixtures of Organic Carbonate Electrolytes. *J Phys Chem C*. 2015;119(9):4502-4515. doi:10.1021/jp511132c
63. Gao J, Lowe MA, Kiya Y, Abruña HD. Effects of Liquid Electrolytes on the Charge–Discharge Performance of Rechargeable Lithium/Sulfur Batteries: Electrochemical and in-Situ X-ray Absorption Spectroscopic Studies. *J Phys Chem C*. 2011;115(50):25132-25137. doi:10.1021/jp207714c
64. Chen L, Shaw LL. Recent advances in lithium-sulfur batteries. *J Power Sources*. 2014;267:770-783. doi:10.1016/j.jpowsour.2014.05.111
65. Gao J, Lowe MA, Kiya Y, Abruña HD. Effects of liquid electrolytes on the charge-discharge performance of rechargeable lithium/sulfur batteries: Electrochemical and in-situ X-ray absorption spectroscopic studies. *J Phys Chem C*. 2011;115(50):25132-25137. doi:10.1021/jp207714c
66. Hayamizu K, Aihara Y. Ion and solvent diffusion and ion conduction of PC-DEC and PC-DME binary solvent electrolytes of LiN(SO2CF3)2. *Electrochim Acta*. 2004;49(20):3397-3402. doi:10.1016/j.electacta.2004.03.007
67. Clark J, Farmer T, Hunt A, Sherwood J. Opportunities for Bio-Based Solvents Created as Petrochemical and Fuel Products Transition towards Renewable Resources. *Int J Mol Sci*. 2015;16(8):17101-17159. doi:10.3390/ijms160817101
68. Ghandi K. A Review of Ionic Liquids, Their Limits and Applications. *Green*

Sustain Chem. 2014;04(01):44-53. doi:10.4236/gsc.2014.41008
69. Reichardt C. Solvents and Solvent Effects: An Introduction. *Org Process Res Dev*. 2007;11(1):105-113. doi:10.1021/op0680082
70. Hayes R, Warr GG, Atkin R. Structure and Nanostructure in Ionic Liquids. *Chem Rev*. 2015;115(13):6357-6426. doi:10.1021/cr500411q
71. Parker, A. J. Q. Rev., Chem. Soc. 1962, 16 163−187. No Title.
72. Greaves TL, Drummond CJ. Protic Ionic Liquids: Properties and Applications. *Chem Rev*. 2008;108(1):206-237. doi:10.1021/cr068040u
73. Menne S, Vogl T, Balducci A. Lithium coordination in protic ionic liquids. *Phys Chem Chem Phys*. 2014;16(12):5485-5489. doi:10.1039/c3cp55183k
74. Visser, A. et al. In Ionic Liquids: Science and Applications.
75. Ohno H. *Electrochemical Aspects of Ionic Liquids*.; 2005. doi:10.1002/0471762512
76. Bonhôte P, Dias A-P, Papageorgiou N, Kalyanasundaram K, Grätzel M. Hydrophobic, Highly Conductive Ambient-Temperature Molten Salts †. *Inorg Chem*. 1996;35(5):1168-1178. doi:10.1021/ic951325x
77. Nádherná M, Reiter J, Moškon J, Dominko R. Lithium bis(fluorosulfonyl)imide-PYR14TFSI ionic liquid electrolyte compatible with graphite. *J Power Sources*. 2011;196(18):7700-7706. doi:10.1016/j.jpowsour.2011.04.033
78. Henderson WA, Passerini S. Phase Behavior of Ionic Liquid−LiX Mixtures: Pyrrolidinium Cations and TFSI - Anions. *Chem Mater*. 2004;16(15):2881-2885. doi:10.1021/cm049942j
79. Matsumoto H, Sakaebe H, Tatsumi K, Kikuta M, Ishiko E, Kono M. Fast cycling of Li/LiCoO2 cell with low-viscosity ionic liquids based on bis(fluorosulfonyl)imide [FSI]−. *J Power Sources*. 2006;160(2):1308-1313. doi:10.1016/j.jpowsour.2006.02.018
80. Yoo K, Deshpande A, Banerjee S, Dutta P. Electrochemical Model for Ionic Liquid Electrolytes in Lithium Batteries. *Electrochim Acta*. 2015;176:301-310. doi:10.1016/j.electacta.2015.07.003
81. Lesch V, Li Z, Bedrov D, Borodin O, Heuer A. The influence of cations on lithium ion coordination and transport in ionic liquid electrolytes: A MD simulation study. *Phys Chem Chem Phys*. 2016;18(1):382-392. doi:10.1039/c5cp05111h
82. Deshpande A, Kariyawasam L, Dutta P, Banerjee S. Enhancement of Lithium Ion Mobility in Ionic Liquid Electrolytes in Presence of Additives. *J Phys Chem C*. 2013;117(48):25343-25351. doi:10.1021/jp409498w
83. Puiu M, Babaligea I, Olmazu C, Răducan A, Oancea D. Peroxidase-mediated oxidation of l-dopa: A kinetic approach. *Biochem Eng J*. 2010;52(2-3):248-254. doi:10.1016/j.bej.2010.08.017
84. Zhou YZ, Alany RG, Chuang V, Wen J. Studies of the Rate Constant of l-DOPA Oxidation and Decarboxylation by HPLC. *Chromatographia*. 2012;75(11-12):597-606. doi:10.1007/s10337-012-2229-1
85. Caldera F. Synthesis of new hyper-cross-linked and hyper-branched polymers.
86. Amici J, Alidoost M, Francia C, et al. O 2 selective membranes based on a dextrin-nanosponge (NS) in a PVDF-HFP polymer matrix for Li–air cells. *Chem Commun*. 2016;52(94):13683-13686. doi:10.1039/C6CC06954A
87. Amici J, Alidoost M, Caldera F, et al. PEEK-WC/Nanosponge Membranes for Lithium-Anode Protection in Rechargeable Li−O 2 Batteries. *ChemElectroChem*. 2018;5(12):1599-1605. doi:10.1002/celc.201800241

88. Wang H, Dai Q, Li Q, et al. Preparation of porous carbon spheres from porous starch. *Solid State Ionics*. 2009;180(26-27):1429-1432. doi:10.1016/j.ssi.2009.08.006
89. Lee J, Kim J, Hyeon T. Recent Progress in the Synthesis of Porous Carbon Materials. *Adv Mater*. 2006;18(16):2073-2094. doi:10.1002/adma.200501576
90. Anceschi A, Magnacca G, Trotta F, Zanetti M. Preparation and characterization of microporous carbon spheres from high amylose pea maltodextrin. *RSC Adv*. 2017;7(57):36117-36123. doi:10.1039/C7RA05343F
91. Anceschi. Synthesis of new nanostructured biomaterials derived from starch.
92. Zubair U, Anceschi A, Caldera F, et al. Dual confinement of sulphur with rGO-wrapped microporous carbon from β-cyclodextrin nanosponges as a cathode material for Li–S batteries. *J Solid State Electrochem*. 2017;21(12):3411-3420. doi:10.1007/s10008-017-3664-6
93. Ashuri M, He Q, Shaw LL. Silicon as a potential anode material for Li-ion batteries: Where size, geometry and structure matter. *Nanoscale*. 2016;8(1):74-103. doi:10.1039/c5nr05116a
94. Lithiation ND, Liu XH, Zhong L, et al. Size-Dependent Fracture of Silicon. *ACS Nano*. 2012;(2):1522-1531. doi:10.1021/nn204476h
95. Chang H, Sun SQ. Silicon nanoparticles: Preparation, properties, and applications. *Chinese Phys B*. 2014;23(8). doi:10.1088/1674-1056/23/8/088102
96. Knipping J, Wiggers H, Rellinghaus B, Roth P, Konjhodzic D, Meier C. Synthesis of High Purity Silicon Nanoparticles in a Low Pressure Microwave Reactor. *J Nanosci Nanotechnol*. 2004;4(8):1039-1044. doi:10.1166/jnn.2004.149
97. Tilley RD, Yamamoto K. The Microemulsion Synthesis of Hydrophobic and Hydrophilic Silicon Nanocrystals. *Adv Mater*. 2006;18(15):2053-2056. doi:10.1002/adma.200600118
98. Tao HC, Yang XL, Zhang LL, Ni SB. Double-walled core-shell structured Si@SiO2@C nanocomposite as anode for lithium-ion batteries. *Ionics (Kiel)*. 2014;20(11):1547-1552. doi:10.1007/s11581-014-1138-8
99. Xu B, Wu H, Lin CX, Wang B, Zhang Z, Zhao XS. Stabilization of silicon nanoparticles in graphene aerogel framework for lithium ion storage. *RSC Adv*. 2015;5(39):30624-30630. doi:10.1039/c5ra00566c
100. Bai X, Yu Y, Kung HH, Wang B, Jiang J. Si@SiOx/graphene hydrogel composite anode for lithium-ion battery. *J Power Sources*. 2016;306:42-48. doi:10.1016/j.jpowsour.2015.11.102
101. Lin N, Zhou J, Zhu Y, Qian Y. Embedding silicon nanoparticles in graphene based 3D framework by cross-linking reaction for high performance lithium ion batteries. *J Mater Chem A*. 2014;2(46):19604-19608. doi:10.1039/c4ta05089d
102. Kim SK, Kim H, Chang H, et al. One-Step Formation of Silicon-Graphene Composites from Silicon Sludge Waste and Graphene Oxide via Aerosol Process for Lithium Ion Batteries. *Sci Rep*. 2016;6(May):1-8. doi:10.1038/srep33688
103. Chen D, Yi R, Chen S, Xu T, Gordin ML, Wang D. Facile synthesis of graphene-silicon nanocomposites with an advanced binder for high-performance lithium-ion battery anodes. *Solid State Ionics*. 2014;254:65-71. doi:10.1016/j.ssi.2013.11.020

104. Tang H, Zhang YJ, Xiong QQ, et al. Self-assembly silicon/porous reduced graphene oxide composite film as a binder-free and flexible anode for lithium-ion batteries. *Electrochim Acta*. 2015;156:86-93. doi:10.1016/j.electacta.2015.01.009
105. Chen Y, Zhang X, Tian Y, Zhao X. Synthesis and characterization of silicon nanoparticles inserted into graphene sheets as high performance anode material for lithium ion batteries. *J Nanomater*. 2014;2014. doi:10.1155/2014/734751
106. Maroni F, Raccichini R, Birrozzi A, et al. Graphene/silicon nanocomposite anode with enhanced electrochemical stability for lithium-ion battery applications. *J Power Sources*. 2014;269:873-882. doi:10.1016/j.jpowsour.2014.07.064
107. Chen S, Bao P, Huang X, Sun B, Wang G. Hierarchical 3D mesoporous silicon@graphene nanoarchitectures for lithium ion batteries with superior performance. *Nano Res*. 2014;7(1):85-94. doi:10.1007/s12274-013-0374-y
108. 2014-12-Tailoring Hollow Silicon−Carbon Nanocomposites As High.pdf.
109. Lener G, Otero M, Barraco DE, Leiva EPM. Energetics of silica lithiation and its applications to lithium ion batteries. *Electrochim Acta*. 2018;259:1053-1058. doi:10.1016/j.electacta.2017.10.126
110. Lener G, Garcia-Blanco AA, Furlong O, et al. A silica/carbon composite as anode for lithium-ion batteries with a large rate capability: Experiment and theoretical considerations. *Electrochim Acta*. 2018;279:289-300. doi:10.1016/j.electacta.2018.05.050
111. Xun S, Song X, Wang L, et al. The Effects of Native Oxide Surface Layer on the Electrochemical Performance of Si Nanoparticle-Based Electrodes. *J Electrochem Soc*. 2011;158(12):A1260. doi:10.1149/2.007112jes
112. Wolter, Mareike, Ph.D, Stefan Börner, Dipl.-Ing., and Uwe Partsch, Ph.D. "Electrode Manufacturing for Lithium-Ion Batteries on Pilot Scale." Fraunhofer IKTS Annual Report 2012/13 (2013): Wolter, Mareike, Ph.D, Stefan Börner, Dipl.-Ing., and Uwe Partsch PD "Electrode M for L-IB on PS. FIAR 2012/13 (2013): *No Title*.
113. Sheng Y. Investigation of Electrolyte Wetting in Lithium Ion Batteries : Effects of Electrode Pore Structures and Solution. *Thesis*. 2015;(December). http://umich.edu/~racelab/static/Webpublication/2015-JPS-XuningF.pdf.
114. Rey-Raap N, Piedboeuf M-LC, Arenillas A, Menéndez JA, Léonard AF, Job N. Aqueous and organic inks of carbon xerogels as models for studying the role of porosity in lithium-ion battery electrodes. *Mater Des*. 2016;109:282-288. doi:10.1016/j.matdes.2016.07.007
115. Choi N-S, Ha S-Y, Lee Y, et al. Recent Progress on Polymeric Binders for Silicon Anodes in Lithium-Ion Batteries. *J Electrochem Sci Technol*. 2015;6(2):35-49. doi:10.5229/JECST.2015.6.2.35
116. Kovalenko I, Zdyrko B, Magasinski A, et al. A Major Constituent of Brown Algae for Use in High-Capacity Li-Ion Batteries. *Science (80-)*. 2011;334(6052):75-79. doi:10.1126/science.1209150
117. Michan AL, Parimalam BS, Leskes M, et al. Fluoroethylene Carbonate and Vinylene Carbonate Reduction: Understanding Lithium-Ion Battery Electrolyte Additives and Solid Electrolyte Interphase Formation. *Chem Mater*. 2016;28(22):8149-8159. doi:10.1021/acs.chemmater.6b02282
118. Choi N-S, Yew KH, Lee KY, Sung M, Kim H, Kim S-S. Effect of fluoroethylene carbonate additive on interfacial properties of silicon thin-film electrode. *J Power Sources*. 2006;161(2):1254-1259.

doi:10.1016/j.jpowsour.2006.05.049
119. Schroder K, Alvarado J, Yersak TA, et al. The Effect of Fluoroethylene Carbonate as an Additive on the Solid Electrolyte Interphase on Silicon Lithium-Ion Electrodes. *Chem Mater*. 2015;27(16):5531-5542. doi:10.1021/acs.chemmater.5b01627
120. Song M-S, Han S-C, Kim H-S, et al. Effects of Nanosized Adsorbing Material on Electrochemical Properties of Sulfur Cathodes for Li/S Secondary Batteries. *J Electrochem Soc*. 2004;151(6):A791. doi:10.1149/1.1710895
121. Zhang F, Zhang X, Dong Y, Wang L. Facile and effective synthesis of reduced graphene oxide encapsulated sulfur via oil/water system for high performance lithium sulfur cells. *J Mater Chem*. 2012;22(23):11452. doi:10.1039/c2jm16543k
122. Zheng S, Chen Y, Xu Y, et al. In Situ Formed Lithium Sulfide/Microporous Carbon Cathodes for Lithium-Ion Batteries. *ACS Nano*. 2013;7(12):10995-11003. doi:10.1021/nn404601h
123. Yeon J-T, Jang J-Y, Han J-G, Cho J, Lee KT, Choi N-S. Raman Spectroscopic and X-ray Diffraction Studies of Sulfur Composite Electrodes during Discharge and Charge. *J Electrochem Soc*. 2012;159(8):A1308-A1314. doi:10.1149/2.080208jes
124. Cañas NA, Wolf S, Wagner N, Friedrich KA. In-situ X-ray diffraction studies of lithium-sulfur batteries. *J Power Sources*. 2013;226(November 2012):313-319. doi:10.1016/j.jpowsour.2012.10.092
125. Diao Y, Xie K, Xiong S, Hong X. Analysis of Polysulfide Dissolved in Electrolyte in Discharge-Charge Process of Li-S Battery. *J Electrochem Soc*. 2012;159(4):A421-A425. doi:10.1149/2.060204jes
126. Barchasz C, Molton F, Duboc C, Leprêtre J-C, Patoux S, Alloin F. Lithium/Sulfur Cell Discharge Mechanism: An Original Approach for Intermediate Species Identification. *Anal Chem*. 2012;84(9):3973-3980. doi:10.1021/ac2032244
127. Patel MUM, Dominko R. Application of in operando UV/Vis spectroscopy in lithium-sulfur batteries. *ChemSusChem*. 2014;7(8):2167-2175. doi:10.1002/cssc.201402215
128. Zhang SS. A new finding on the role of LiNO3 in lithium-sulfur battery. *J Power Sources*. 2016;322:99-105. doi:10.1016/j.jpowsour.2016.05.009
129. Kim HS, Jeong CS. Electrochemical properties of binary electrolytes for lithium-sulfur batteries. *Bull Korean Chem Soc*. 2011;32(10):3682-3686. doi:10.5012/bkcs.2011.32.10.3682
130. Suo L, Hu YS, Li H, Armand M, Chen L. A new class of Solvent-in-Salt electrolyte for high-energy rechargeable metallic lithium batteries. *Nat Commun*. 2013;4:1-9. doi:10.1038/ncomms2513
131. Xia Y, Fang R, Xiao Z, et al. Confining Sulfur in N-Doped Porous Carbon Microspheres Derived from Microalgaes for Advanced Lithium–Sulfur Batteries. *ACS Appl Mater Interfaces*. 2017;9(28):23782-23791. doi:10.1021/acsami.7b05798
132. Wu F, Zhu Q, Chen R, Chen N, Chen Y, Li L. A Safe Electrolyte with Counterbalance between the Ionic Liquid and Tris(ethylene glycol)dimethyl ether for High Performance Lithium-Sulfur Batteries. *Electrochim Acta*. 2015;184:356-363. doi:10.1016/j.electacta.2015.10.109
133. Wang L, Byon HR. N-Methyl-N-propylpiperidinium bis(trifluoromethanesulfonyl)imide-based organic electrolyte for high

performance lithium-sulfur batteries. *J Power Sources*. 2013;236:207-214. doi:10.1016/j.jpowsour.2013.02.068
134. Park J-W, Ueno K, Tachikawa N, Dokko K, Watanabe M. Ionic Liquid Electrolytes for Lithium-Sulfur Batteries. *J Phys Chem C*. 2013;117(40):20531-20541. doi:10.1021/jp408037e
135. Montanino M, Alessandrini F, Passerini S, Appetecchi GB. Water-based synthesis of hydrophobic ionic liquids for high-energy electrochemical devices. *Electrochim Acta*. 2013;96:124-133. doi:10.1016/j.electacta.2013.02.082
136. Appetecchi GB, Scaccia S, Tizzani C, Alessandrini F, Passerini S. Synthesis of Hydrophobic Ionic Liquids for Electrochemical Applications. *J Electrochem Soc*. 2006;153(9):A1685. doi:10.1149/1.2213420
137. He J, Chen Y, Manthiram A. MOF-derived Cobalt Sulfide Grown on 3D Graphene Foam as an Efficient Sulfur Host for Long-Life Lithium-Sulfur Batteries. *iScience*. 2018;4:36-43. doi:10.1016/j.isci.2018.05.005